Faculty of Mathematical, Physical and Natural Sciences
Department of Environmental Sciences
University of Milano-Bicocca

# DEVELOPMENT OF AUTOMATIC SPECTROMETRIC SYSTEMS FOR PROXIMAL SENSING OF PHOTOSYNTHETIC ACTIVITY OF VEGETATION

## PhD Dissertation

**candidate:**
Dr. Sergio Cogliati

**Supervisor:**
Dr. R. Colombo

**Advisor:**
Dr. A. Cescatti

**Coordinator:**
Prof. M. Vighi

January 2011

# Acknowledgements

This work would not have been possible without the contribution and invaluable help of many people. I am especially grateful to Drs. Micol Rossini for the collaboration on the development of the research project and for daily fruitful discussions at every stage of the work. I am also grateful to Dr. Michele Meroni his guidance instrumental in setting up this research project and introducing me to the field spectrometry techniques.

I would like to thank Dr. Roberto Colombo for his scientific support of the research activity and for the financial support of the research activity. I'm grateful to my advisor Dr. Alessandro Cescatti for valuable insights and comments. Very special thanks to the colleagues of the Remote Sensing of Dynamics Laboratory, Andrea Marchesi, Lorenzo Busetto, Francesco Fava, Mirco Migliavacca and Cinzia Panigada for their support and friendship.

I would also like to thank Dr. Alessandro Barducci and Francesco Castagnoli of the Italian National Research Council of Florence (CNR-IFAC) for the collaboration on the design and realization of the HyperSpectral Irradiometer (HSI). Special thanks also to Edoardo Cremonese, Marta Galvagno and Umberto Morra di Cella (all all ARPA-VdA, IT) for their fundamental and faultless help in the management of the measurement station at Torgnon (AO). I would also like to thank Beniamino Gilioli (CNR-IBIMET) and his colleagues for the collaboration on the $CO_2$ gas-flux measurement and analysis at the Sentinel-3 Experiment.

This research was funded by Interreg project PhenoAlp (European Regional Development Found) and field campaigns at San Rossore were funded by the European Space Agency in the framework of the Sentinel-3 Experiment. The participation to international meetings was partially funded by "Spectral Sampling Tools for Vegetation Biophysical Parameters and Flux Measurements in Europe" EU COST action (ES0903).

Finally, I am infinitely indebted to Veronica, to my family and friends for their enduring patience and support throughout this work.

# Table of contents

# Abstract

Terrestrial ecosystems absorb approximately 120 Gt of carbon annually through the photosynthetic process, also referred as *Gross Primary Production* (GPP). For this reason, assessment and modeling of photosynthetic functioning are critical issues in climate change research and crucial in predicting carbon dynamics.

The advent of *Eddy Covariance* (EC) technique provided(e.g., Baldocchi et al., 1996) in situ long-term and continuous measurements of carbon and water gas fluxes. An extensive network of such EC measurement stations has been established for a better comprehension of the main processes governing the carbon cycle. However, EC technique offers an intensive sampling of the temporal domain, but it lacks in spatial representativeness since it measures a relatively small area. Satellite *Remote Sensing* (RS) observations provide spatial and temporal variability of ecosystem parameters driving carbon fluxes which can be integrated with EC measurements to scale up carbon estimates to regional and global level.

Current Earth observing systems generally provide information of plant status derived from structural or biochemical properties such as *Leaf Area Index* (LAI) or *chlorophyll* content. These data can be used to model the potential photosynthetic rates of plant ecosystems and not the actual one. An alternative is offered by the monitoring of the *energy dissipation pathways*. In fact, the excess light absorbed by vegetation is released through heat dissipation (xanthophyll cycle) and/or re-emitted as *Fluorescence* (F). Recent RS techniques have encouraged the investigation of these *energy dissipation pathways* through the *Photochemical Reflectance Index* (PRI) (heat dissipation) and the analysis of the *Fraunhofer* lines (F re-emission). For a better comprehension of the link between photosynthesis and optical signals, a growing number of studies have recently focused on the collection of large datasets of repeated field spectral measurements in the sampling area of EC flux towers.

Object of this dissertation is the development of automatic spectrometric systems capable of collecting unattended, continuous, long-term spectral measurements of vegetation. Two different automatic spectrometric systems have been developed: the *HyperSpectral Irradiometer* (HSI) and the *Multiplexer Radiometer Irradiometer* (MRI). Both instruments are able to routinely and autonomously measure: sun incoming irradiance (downwelling Irradiance, $E^{TOT}$) and the irradiance/radiance upwelling from the investigated Earth surface (HSI measures $E^{S}$, MRI measures $L^{S}$). The systems are able to simultaneously collect "*fine*" and "*ultra-fine*" spectrums that allow the computation of different *Vegetation Indices* (VIs), including the PRI, and the estimation of the sun-induced chlorophyll *Fluorescence* at $O_2$-A band (F@760). HSI and MRI systems are intended to be operated in experimental sites equipped with *Eddy Covariance* flux towers to increase our understanding of the link between optical signals and $CO_2$ fluxes.

Instruments were installed at two different sites equipped with a micrometeorological EC flux tower. HSI was operated in an alpine pasture for two consecutive years (2009/2010), while MRI was installed in an alfalfa field in the context of the *Sen3Exp* field survey. Time series of spectral indices (VIs, PRI and F@760) and $CO_2$ fluxes data are reported and analyzed.

As a demonstration of the potential of these instruments to estimate the GPP, the use of derived *Vegetation Indices* and F@760 as inputs of *Light Use Efficiency* (LUE) models was tested in the last part of the research. Several versions of the basic LUE models were used in order to verify the most effective formulation for the description of GPP.

# *List of Tables*

# *List of Figures*

*VNIR and NIR spectrometers. The reflectance peak at 760 nm is visible in the NIR spectrometer data and it is originated by the fluorescence infilling of the $O_2$-A band.*

*Figure 3.6: Technical scheme of the Multiplexer Radiometer Irradiometer (MRI). The uplooking foreoptic (cosine receptor) collects the incident sunlight, sampling of the radiance from the Earth's surface is made by the down looking optical channel (bare fiber). Optical multiplexer, spectrometers and the personal computer are hosted in a protective box.*

*Figure 3.7: Typical setup of MRI installation in field: the tripod supports the ends of the optical channels. The red circle evidences the cosine corrector receptor, the green one indicates the end of the down-looking channels (bare fibers).*

*Figure 3.8: Example of a single spectral data acquisition session over a vegetated surface. Downwelling and upwelling radiances (upper panel) and resulting HCRF (lower panel) for Spec1 covering the full VNIR range and for Spec2, covering the restricted range 700-800 nm with higher resolution.*

*Figure 3.9: Diagram of the principal spectral features of field spectrometers. Points represent the spectral bands, FWHM (i.e. spectral resolution) and center wavelength of a response function.*

*Figure 3.10: Example of: A) Spectrum of CAL-2000 (Ocean Optics, USA) calibration light source measured by "ultra-fine" spectrometer. B) Normalized spectral response at the 750 nm argon line with 3 parameters Gaussian fit.*

*Figure 3.11: Distribution of selected absorption features over the incident irradiance spectrum (black curve). Solid vertical lines refer to solar Fraunhofer lines, dashed vertical lines refer to molecular oxygen absorption features, and gray areas are the spectral regions affected by water vapor absorption.*

*Figure 3.12: Spectral characterization of HSI during field operation in 2010. Results of SS detection using SpecCal algorithm for "fine" (SPEC1) and "ultra-fine" (SPEC2) resolution spectrums are reported in upper (A) and lower (B) panels, respectively. The small spectral coverage provided in the NIR range by SPEC2 allows using only one absorption feature: the $O_2$-A absorption band (760nm).*

*Figure 3.13: Field set-up used for FI between the reference and the MRI system. The tripod on the left supports the terminations of the optical channels of MRI, while the tripod on the right leads the optical fibers of the reference system. The down-looking optical fibers of MRI observe the Spectralon reference panel as well as the optical fibers of the reference system. The uplooking cosine foreoptics of MRI point the sky (zenith view).*

# *List of Acronyms*

| | |
|---|---|
| **APAR** | Absorbed Photosynthetically Active Radiation |
| **BHR** | BiHemispherical Reflectance Factor |
| **BRDF** | Bidirectional Reflectance Distribution Function |
| **Chl** | Chlorophyll |
| **EC** | Eddy Covariance |
| **F** | Chlorophyll Fluorescence |
| **FI** | Field Intercalibration |
| **FLD** | Fraunhofer Line Depth method |
| **FOV** | Field of View |
| **FWHM** | Full Width at Half Maximum |
| **F@760** | sun induced chlorophyll fluorescence at 760 nm |
| ***f*APAR** | fraction of APAR |
| **GPP** | Gross Primary Production |
| **HCRF** | Hemispherical Conical Reflectance Factor |
| **LAI** | Leaf Area Index |
| **LUE** | Light Use Efficiency |
| **NDVI** | Normalized Difference Vegetation Index |
| **NEP** | Net Ecosystem Production |
| **NPQ** | Non-Photochemical Quenching |
| **PAR** | Photosynthetically Active Radiation |
| **PRI** | Photochemical Reflectance Index |
| **RS** | Remote Sensing |
| **SFM** | Spectral Fitting Method |

| | |
|---|---|
| **SS** | Spectral Shift |
| **VIs** | Vegetation Indices |

# Chapter 1

# Introduction

## 1.1 Scientific Framework

Vegetation is the functional interface between the Earth's terrestrial biosphere and the atmosphere. Terrestrial plants fix carbon dioxide ($CO_2$) as organic compounds through photosynthesis or *Gross Primary Production* (GPP). This latter represents one of the key processes removing approximately 120 Gt of carbon annually from the atmosphere (Beer et al., 2010; Janzen, 2004). Photosynthesis is the conversion of light energy into chemical energy by living organisms and it represents the key process mediating 90% of carbon and water fluxes in the coupled biosphere–atmosphere system. About 50% of the carbon is released by plant respiration within a short time period. The remaining carbon in ecosystems is generally referred as *Net Ecosystem Production* (NEP). Photosynthetic $CO_2$ uptake rates and those released by respiration were balanced for the past several hundred thousand years keeping atmospheric $CO_2$ levels between 180 ppm and 280 ppm (Petit et al., 1999).

Disturbances and long-term changes of ecosystems release parts of this carbon within the time-frame of centuries. Currently there are great uncertainties about the human impact on the magnitude of these processes. Human activities are known to perturb in different ways these flows of carbon. Since the discovery of fossil carbon as a convenient form of energy, the residues of some hundred million years-worth of past photosynthetic carbon assimilation have been combusted to $CO_2$ and returned to the Earth's atmosphere 10–100 times faster than at any time in the past. Carbon that is released by anthropogenic activities has been monotonically increasing in the past decades. The net carbon that is fixed annually in natural ecosystems, however, is highly variable. Photosynthetic $CO_2$ fixation is the first key process removing carbon from the atmosphere and large year-to-year variations in carbon removed from the atmosphere highlight the significant role of the biogenic carbon cycle, where plant photosynthesis constitutes the first key process in determining GPP. Small changes in GPP will unavoidably have major impacts on the whole carbon cycle, with unpredictable impacts on short-, mid- and long-term carbon storage. GPP is also related to the global water cycle due to the strong coupling between photosynthetic rates and canopy transpiration. For each $CO_2$ molecule that is used in the photosynthesis, several hundred molecules of water are transpired (Jung et al., 2010).

There is a great need for a better understanding of the dynamics of carbon fluxes between the biosphere and the atmosphere, especially in response to perturbations. Photosynthesis is a complex process depending on various environmental factors which translate into variations in carbon and energy exchange between vegetation and atmosphere. Moreover the changes in land use and land management, e.g. the massive conversion of natural plant ecosystems in managed agricultural systems and altered land management practices have a strong impact on the Earth's biogeochemical cycles.

Photosynthetic $CO_2$ and water fluxes at canopy level can be reliably quantified using the *Eddy Covariance* (EC) technique. Over the last few decades, a worldwide network of micrometeorological flux stations (FLUXNET) has been established to provide understanding of drivers and processes controlling the carbon and water exchanges between biosphere and atmosphere (e.g. Baldocchi et al., 1996). Such network provides local scale information that can be up-scaled using *Remote Sensing* (RS) data for mapping the biophysical and biogeochemical processes from regional to global scale (e.g. Beer et al., 2010; Running et al., 2004).

*Remote Sensing* techniques can provide spatially-distributed measurements on a regular time basis in order to monitor the carbon cycle. Current strategies in optical *Remote Sensing* mainly rely on reflectance data offered by several Earth observing systems which provide estimates of structural or biochemical vegetation properties such as *Leaf Area Index* (LAI) or *Chlorophyll* (Chl) content (e.g. Baret et al., 2007). These data can be used to model the potential photosynthetic rates of plant ecosystems but actual vegetation photosynthesis (expressed as *Gross Primary Production*) cannot be observed directly. Photosynthesis has often been estimated using *Light-Use Efficiency* (LUE) models parameterized using RS data. The widely used *LUE* model (Monteith, 1972; 1977) stated that GPP is a function of the incident *Absorbed Photosynthetically Active Radiation* (APAR) and light-use efficiency (ε) which represents the conversion efficiency of absorbed energy to fixed carbon:

$$GPP = \varepsilon * fAPAR * PAR \qquad \textit{Equation 1.1}$$

where ε is the *Light-Use Efficiency* term, PAR is the incident *Photosynthetically Active Radiation* and *f*APAR is the *fraction* of PAR absorbed by vegetation. The *f*APAR can be estimated from remotely sensed *Vegetation Indices* (VIs) such as the *Normalized Difference Vegetation Index* (NDVI) (Rouse et al., 1974). Unfortunately, NDVI can be used to estimate the amount of light absorbed by a plant, but not the efficiency with which vegetation uses this to fix carbon. In fact NDVI measures the “*greenness*” of the vegetation and not photosynthesis itself. Because of this the efficiency term in the LUE model is often assumed to be the same for all vegetation types. There is now considerable evidence to suggest that the efficiency with which plants fix carbon can vary with species, vegetation functional type, and in response to changes in environmental conditions (e.g. variations in temperature and water vapor pressure deficit). In fact, the magnitude of ε is fundamentally determined by the quantum efficiency of photosynthesis. This is known to be reduced by stress factors, such as extreme temperatures, direct sunlight, or shortage of water and nutrients.

An alternative to this approach is offered by a new generation of *Remote Sensing* techniques able to monitor the energy dissipation pathways of vegetation. Typically, part of the energy absorbed by Chl pigments is not used by the light reactions of photosynthesis and is dissipated as fluorescence (re-emission of light at a longer wavelength than the absorbed one) and/or *Non-Photochemical Quenching* (NPQ) (Björkman, 1995). These two processes compete with photosynthesis for the use of the absorbed light.

Chlorophyll fluorescence can be considered a direct probe of the functional status of photosynthetic machinery because of its relationship with photosynthesis. This close relationship enabled plant physiologists to use field- or laboratory-based actively-induced fluorescence measurements as a diagnostic tool to assess the vitality of the photosynthetic apparatus. Under solar illumination chlorophyll re-emission adds continuously a weak signal to reflected solar radiation. Measurement of the sun-induced Chl fluorescence (F) by passive (i.e. without artificial excitation sources) RS systems at field scale is a challenging issue that has been proven to be feasible and may have the potential for the assessment of actual plant photosynthesis. The F signal can be detected passively in narrow dark lines of the solar and atmospheric spectrum in which irradiance is strongly reduced (*Fraunhofer* lines). In the near-infrared, one absorption band ($O_2$-A) positioned at 760 nm originates from molecular oxygen present in the Earth's atmosphere and has been extensively exploited for F estimation because it is spectrally wide (about 2 nm), deep (i.e. 80% of energy is absorbed) and close to the maximum of the chlorophyll fluorescence emission spectrum positioned at about 740 nm. In such absorption band, F can be detected by measuring to what extent the "wells" are filled by F compared to the continuum using different estimation techniques (Alonso et al., 2008; Meroni and Colombo, 2006; Plascyk, 1975; Plascyk and Gabriel, 1975). Some studies have recently shown that F can be used to estimate ε at leaf (Meroni et al., 2008a), canopy (Meroni et al., 2008b) and ecosystem level (Damm et al., 2010; Rossini et al., 2010). For a review of methods used to estimate F from RS observations see Meroni et al. (2009).

The other mechanism of energy dissipation, the NPQ, is linked to heat dissipation (Demmig-Adams, 2003). The rationale to estimate NPQ from the distance is posed by the observation of reflectance changes at 531 nm related to the de-epoxidation of xanthophyll pigments (Gamon et al., 1992) which is a photoprotective process involved in excess energy dissipation as heat (DemmigAdams and Adams, 1996). Gamon et al. (1992) proposed a vegetation index exploiting the green part of the spectrum, the Photochemical Reflectance Index (PRI), derived from the normalized difference between narrow band reflectances at 531 nm (i.e. the xanthophyll affected wavelength), and 570 nm (i.e. a reference wavelength) as an indirect measure of NPQ. Several studies have shown a good relationship between PRI, photosynthetic rates and ε when measuring at leaf (Gamon et al., 1997; Meroni et al., 2008a) and canopy scale (Garbulsky et al., 2008; Meroni et al., 2008b; Nichol et al., 2000; 2002; 2006).

The advent of hyperspectral sensors (i.e. high number of contiguous narrow bands) nowadays allows the remote detection of the variation of these energy dissipation processes by monitoring F and PRI. One way to better understand the relationships between the RS data (VIs, F and PRI) and photosynthesis is the installation of hyperspectral RS devices at EC flux towers to measure near-surface spectra in the *"footprint"* of flux towers.

## 1.2 Rationale

Integration of optical *Remote Sensing* observations with flux measurements across multiple scales is essential for understanding temporal and spatial patterns of surface–atmosphere fluxes of carbon and water vapor. EC flux towers provide local scale measurements (*footprint*) through the time (half-hourly measurement), while RS usually covers large areas with coarse temporal and/or spatial resolution. This sampling mismatch between flux and remote sensing measurements makes it difficult to directly relate the two types of measurement (Gamon et al., 2006b) and often requires the use of complex models to integrate fluxes with optical sampling.

For a better comprehension of the link between photosynthesis and optical signals, a growing number of studies has recently focused on the collection of large datasets of repeated field spectrometric observations in the sampling area of flux towers over diurnal cycles or longer time scales (e.g. with weekly measurements to get a seasonal trend) (Damm et al., 2010; Inoue et al., 2008; Rascher et al., 2009; Rossini et al., 2010). Long-lasting field spectrometric campaigns based on manual measurements are extremely resource demanding and do not ensure repeatability of the acquisition conditions as the instrument setup is initialized each day. To overcome such limitations few research groups initiated automatic tower-based spectral reflectance measurements (Daumard et al., 2010; Gamon et al., 2006a; Hilker et al., 2010; Leuning et al., 2006; Nakaji et al., 2008) using different devices. With such setups, non-imaging hyperspectral sensors (also referred as non-imaging spectrometers) are installed in the field on a flux station (or in its proximity), and are operated automatically for long periods (i.e. months to years).

Despite of the growing interest of the scientific community on the assessment of the carbon dynamics, only a small number of automatic tower based instruments are available nowadays (for a review see section 2.2.3), in part due to the high cost and complex long-term operation of hyperspectral spectrometers. Overall, most of these instruments are based on reflectance measurement at "*fine*" spectral resolution, with the intent to assess $CO_2$ exchange exploiting optical VIs and the *Photochemical Reflectance Index*. Only the system recently proposed by Daumard et al. (2010) provides continuous measurements at "*ultra-fine*" resolution in the spectral region interested by sun-induced chlorophyll *Fluorescence* emission.

In this context, further studies are needed to better understand the instrument characteristics most suited for ecosystem monitoring and carbon modeling, in terms of measurement approach (e.g. reflectance/radiance), devices and optical equipment employed (e.g. spectrometers, foreoptics etc.). Furthermore, new instruments able to measure sun-induced chlorophyll *Fluorescence* in the *Fraunhofer* lines are required, in order to provide F time series coupled with GPP measurements which can consolidate the role of F at stand level for carbon dynamic modeling.

The *SpecNet*[1] (Spectral Network) project (Gamon et al., 2006b) and the "*Spectral Sampling Tools for Vegetation Biophysical Parameters and Flux Measurements in Europe*" EU COST action (ES0903[2]) have been recently established to promote these activities. These international initiatives are designed to address the needs to apply scale-appropriate optical sampling in conjunction with EC flux measurements of carbon dioxide and water vapor.

---

[1] Website: http://specnet.info/

[2] Website: http://cost-es0903.fem-environment.eu/

## 1.3 Research objectives and structure of the dissertation

The aim of the research activity is the development of automatic spectrometric systems capable of collecting unattended, continuous, long-term spectral measurements of vegetation. These instruments are intended to be operated in experimental sites equipped with *Eddy Covariance* flux towers to increase our understanding of the link between optical signals and $CO_2$ fluxes. Dataset collected allows comparing continuously acquired spectral data with $CO_2$ fluxes at the same spatial and time scale. The requirements of these instruments are: i) to provide measurements of: sun incoming irradiance and irradiance/radiance upwelling from the investigated Earth surface; ii) to simultaneously collect "*fine*" and "*ultra-fine*" spectrums, which allow to derive *Vegetation Indices* (VIs), PRI, and sun-induced chlorophyll *Fluorescence* at $O_2$-A band (F@760).

The dissertation begins in chapter 2 with a brief review of the current status of RS techniques and automatic instruments available for vegetation monitoring.

The new automatic spectrometric systems realized: the *HyperSpectral Irradiometer* (HSI) and the *Multiplexer Radiometer Irradiometer* (MRI) are described in chapter 3. The development of such systems included the optical design and the definition of the *laboratory* and *in-situ* calibration procedures. The development of two different automatic systems addresses the need of study the best optical equipment and measurement configuration (e.g. upwelling radiance, $L^S$; upwelling irradiance, $E^S$) to quantify local scale vegetation properties and actual photosynthetic rate. Spectral and radiometric methodologies to calibrate the automatic systems before the installation and during the normal measurement operation in field were developed in order to provide calibrated "*fine*" and "*ultra-fine*" data.

The software segment of the developed automatic systems is described in Chapter 4. Control of HSI and MRI and unattended data acquisition are provided by the *Auto3S* software, developed from the original release of 3S software (Meroni and Colombo, 2009); processing of collected data is performed by OO_IDL computer code.

Chapter 5 deals with the field test of the automatic instruments. HSI was developed in the framework of the PhenoAlp Interreg project. In this context a permanent measurement station able to measure $CO_2$ gas-exchange using the EC technique was operated on an alpine pasture to analyze seasonal and interannual variability of carbon fluxes at local scale. A part of the study concerned the use of automatic spectrometric systems to improve the understanding of the link between gas fluxes and optical signals of vegetation. HSI was installed during two consecutive years (2009 and 2010) on the alpine pasture measurement site in order to evaluate the instrument capabilities to collect seasonal time series of hyperspectral data. The second automatic field spectrometric system developed, the Multiplexer Radiometer Irradiometer, was installed on an agriculture crop filed in the context of the “Sentinel 3 Experiment” (Sen3Exp) field survey, organized and promoted by the European Space Agency (ESA) as consolidation study for the Sentinel-3 mission.

As a demonstration of the potential of HSI and MRI to estimate the GPP, vegetation indices and F@760 derived from these systems were used as inputs of LUE models in the last part of the research (Chapter 6). Several versions of the basic LUE models, as proposed by Rossini et al. (2010), were used in order to verify the most effective formulation for the description of GPP.

# Bibliography

Alonso, L. et al., 2008. Improved Fraunhofer Line Discrimination Method for Vegetation Fluorescence Quantification. Ieee Geoscience and Remote Sensing Letters, 5(4): 620-624.

Baldocchi, D., Valentini, R., Running, S., Oechel, W. and Dahlman, R., 1996. Strategies for measuring and modelling carbon dioxide and water vapour fluxes over terrestrial ecosystems. Global Change Biology, 2(3): 159-168.

Baret, F. et al., 2007. LAI, fAPAR and fCover CYCLOPES global products derived from VEGETATION - Part 1: Principles of the algorithm. Remote Sensing of Environment, 110(3): 275-286.

Beer, C. et al., 2010. Terrestrial Gross Carbon Dioxide Uptake: Global Distribution and Covariation with Climate. Science, 329(5993): 834-838.

Björkman, O.D.-A., B., 1995. Regulation of photosynthetic light energy capture, conversion, and dissipation in leaves of higher plants. Ecophysiology of Photosynthesis: pp. 17-47.

Damm, A. et al., 2010. Remote sensing of sun induced fluorescence to improve modelling of diurnal courses of Gross Primary Production (GPP). Global Change Biology, 16(1): 171-186.

Daumard, F. et al., 2010. A Field Platform for Continuous Measurement of Canopy Fluorescence. Ieee Transactions on Geoscience and Remote Sensing, 48(9): 3358-3368.

Demmig-Adams, B., 2003. Linking the xanthophyll cycle with thermal energy dissipation. Photosynthesis Research, 76(1-3): 73-80.

DemmigAdams, B. and Adams, W.W., 1996. Xanthophyll cycle and light stress in nature: Uniform response to excess direct sunlight among higher plant species. Planta, 198(3): 460-470.

Gamon, J.A., Cheng, Y.F., Claudio, H., MacKinney, L. and Sims, D.A., 2006a. A mobile tram system for systematic sampling of ecosystem optical properties. Remote Sensing of Environment, 103(3): 246-254.

Gamon, J.A., Penuelas, J. and Field, C.B., 1992. A Narrow-Waveband Spectral Index That Tracks Diurnal Changes in Photosynthetic Efficiency. Remote Sensing of Environment, 41(1): 35-44.

Gamon, J.A., Rahman, A.F., Dungan, J.L., Schildhauer, M. and Huemmrich, K.F., 2006b. Spectral Network (SpecNet) - What is it and why do we need it? Remote Sensing of Environment, 103(3): 227-235.

Gamon, J.A., Serrano, L. and Surfus, J.S., 1997. The photochemical reflectance index: an optical indicator of photosynthetic radiation use efficiency across species, functional types, and nutrient levels. Oecologia, 112(4): 492-501.

Garbulsky, M.F., Penuelas, J., Papale, D. and Filella, I., 2008. Remote estimation of carbon dioxide uptake by a Mediterranean forest. Global Change Biology, 14(12): 2860-2867.

Hilker, T., Nesic, Z., Coops, N.C. and Lessard, D., 2010. A NEW, AUTOMATED, MULTIANGULAR RADIOMETER INSTRUMENT FOR TOWER-BASED OBSERVATIONS OF CANOPY REFLECTANCE (AMSPEC II). Instrumentation Science & Technology, 38(5): 319-340.

Inoue, Y., Penuelas, J., Miyata, A. and Mano, M., 2008. Normalized difference spectral indices for estimating photosynthetic efficiency and capacity at a canopy scale derived from hyperspectral and CO2 flux measurements in rice. Remote Sensing of Environment, 112(1): 156-172.

Janzen, H.H., 2004. Carbon cycling in earth systems - a soil science perspective. Agriculture Ecosystems & Environment, 104(3): 399-417.

Jung, M. et al., 2010. Recent decline in the global land evapotranspiration trend due to limited moisture supply. Nature, 467(7318): 951-954.

Leuning, R., Hughes, D., Daniel, P., Coops, N.C. and Newnham, G., 2006. A multi-angle spectrometer for automatic measurement of plant canopy reflectance spectra. Remote Sensing of Environment, 103(3): 236-245.

Meroni, M. and Colombo, R., 2006. Leaf level detection of solar induced chlorophyll fluorescence by means of a subnanometer resolution spectroradiometer. Remote Sensing of Environment, 103(4): 438-448.

Meroni, M. and Colombo, R., 2009. 3S: A novel program for field spectroscopy. Computers & Geosciences, 35: 1491-1496.

Meroni, M. et al., 2008a. Leaf level early assessment of ozone injuries by passive fluorescence and photochemical reflectance index. International Journal of Remote Sensing, 29(17-18): 5409-5422.

Meroni, M. et al., 2009. Remote sensing of solar-induced chlorophyll fluorescence: Review of methods and applications. Remote Sensing of Environment, 113(10): 2037-2051.

Meroni, M. et al., 2008b. Assessing steady-state fluorescence and PRI from hyperspectral proximal sensing as early indicators of plant stress: The case of ozone exposure. Sensors, 8(3): 1740-1754.

Monteith, J.L., 1972. Solar radiation and productivity in tropical ecosystems. Journal of Applied Ecology, 9: 747-766.

Monteith, J.L., 1977. Climate and efficiency of crop production in Britain. Philosophical Transactions of the Royal Society of London Series B-Biological Sciences, 281: 271-294.

Nakaji, T. et al., 2008. Utility of spectral vegetation indices for estimation of light conversion efficiency in coniferous forests in Japan. Agricultural and Forest Meteorology, 148(5): 776-787.

Nichol, C.J. et al., 2000. Remote sensing of photosynthetic-light-use efficiency of boreal forest. Agricultural and Forest Meteorology, 101(2-3): 131-142.

Nichol, C.J. et al., 2002. Remote sensing of photosynthetic-light-use efficiency of a Siberian boreal forest. Tellus Series B-Chemical and Physical Meteorology, 54(5): 677-687.

Nichol, C.J., Rascher, U., Matsubara, S. and Osmond, B., 2006. Assessing photosynthetic efficiency in an experimental mangrove canopy using remote sensing and chlorophyll fluorescence. Trees-Structure and Function, 20(1): 9-15.

Petit, J.R. et al., 1999. Climate and atmospheric history of the past 420,000 years from the Vostok ice core, Antarctica. Nature, 399(6735): 429-436.

Plascyk, J.A., 1975. Mk Ii Fraunhofer Line Discriminator (Fld-Ii) for Airborne and Orbital Remote-Sensing of Solar-Stimulated Luminescence. Optical Engineering, 14(4): 339-346.

Plascyk, J.A. and Gabriel, F.C., 1975. Fraunhofer Line Discriminator Mkii - Airborne Instrument for Precise and Standardized Ecological Luminescence Measurement. Ieee Transactions on Instrumentation and Measurement, 24(4): 306-313.

Rascher, U. et al., 2009. CEFLES2: the remote sensing component to quantify photosynthetic efficiency from the leaf to the region by measuring sun-induced fluorescence in the oxygen absorption bands. Biogeosciences Discussions, 6(1): 2217-2266.

Rossini, M. et al., 2010. High resolution field spectroscopy measurements for estimating gross ecosystem production in a rice field. Agricultural and Forest Meteorology, 150(9): 1283-1296.

Rouse, J.W., Haas, R.H., Schell, J.A., Deering, D.W. and Harlan, J.C., 1974. Monitoring the Vernal Advancements and Retro Gradation of Natural Vegetation, Greenbelt, MD, USA.

Running, S.W. et al., 2004. A continuous satellite-derived measure of global terrestrial primary production. Bioscience, 54(6): 547-560.

# Chapter 2

# Techniques for estimating vegetation photosynthesis

Photosynthetic $CO_2$ fixation of terrestrial ecosystems is one of the key processes removing 120 Gt $yr^{-1}$ of carbon from the atmosphere, as recently reported in the IPCC Fourth Assessment Report (Denman, 2007). For this reason assessment and modeling of photosynthetic functioning of terrestrial ecosystems are critical issues in climate change research and crucial in predicting carbon dynamics.

Attempts at estimating terrestrial carbon fluxes at global scale have concentrated on the development of process-based ecosystem exchange models (e.g. the Boreal Ecosystem Productivity Simulator (BEPS, Liu et al., 1997)) and the Terrestrial Ecosystem Model (TEM, e.g. Raich et al., 1991). While such models show great promise, their applicability at regional and global scales is challenging due to their complexity and requirements for data that are often scarce or unavailable at appropriate spatial and temporal scales. Several measurement techniques are available for local monitoring of carbon balance, for example the advent of *Eddy Covariance* (EC) technique (e.g., Baldocchi et al., 1996) provided in situ long-term and continuous measurements of carbon and water gas fluxes. An extensive network of EC measurement stations (FLUXNET network) has been established for a better comprehension of the main processes governing the carbon cycle of terrestrial ecosystems. However, EC technique offers an intensive sampling of the temporal domain, but it lacks in spatial representativeness since it measures a relatively small area and the regional (or continental) up-scaling of the measurements is problematic (Chen et al., 2003). As a complement to the EC technique, satellite-based

*Remote Sensing* (RS) observations provide spatial and temporal variability of ecosystem parameters driving carbon fluxes which can be integrated with EC measurements to scale up carbon estimates to regional and global level. A brief overview of *Eddy Covariance* and *Remote Sensing* techniques actually used to monitor vegetation photosynthetic status is given in this chapter.

## 2.1 Eddy Covariance techniques

The *Eddy Covariance* (EC) technique is one of the most commonly applied methods for measuring primary production. EC evaluates the exchange rate of $CO_2$ across the interface between the atmosphere and plants canopies by measuring the covariance between fluctuations in vertical wind velocity and $CO_2$ mixing ratio. In particular the technique determinates the net difference (NEP) of $CO_2$ across the canopy-atmosphere interface using a statistical analysis of the instantaneous vertical mass flux density ($F= \omega\rho_c$, $\mu mol\ m^{-2}s^{-1}$). The product is a relationship that expresses the mean flux density of $CO_2$ averaged over time as the covariance between fluctuation in vertical velocity ($\omega$) and the $CO_2$ mixing ratio ($c = \rho_c / \rho_a$ where $\rho_a$ is air density $\rho_c$ is the $CO_2$ density):

$$F = \overline{\rho_a}\,\overline{\omega' c'}$$ *Equation 2.1*

The overbars denote time averaging and primes represent fluctuation from the mean (eg. $c' = c - \bar{c}$). Usually averaged time interval is 30 minutes. While this measurement technique is capable of providing accurate and continuous estimates of ecosystem level NEP (Baldocchi et al., 2001), the area or footprint that can be sampled with EC measurements (also known as the flux footprint) is usually restricted to a few hectares, depending on the height of the flux measurement, terrain, stand height and density (Kljun et al., 2004). The EC method assumptions require flat terrains, extended and uniform fetch of vegetation upwind, steady state atmospheric condition and that the sensors and the data logging systems are able to sense and record the fastest and smallest eddies (Baldocchi, 2003). Violation of these assumptions can cause systematic errors in the interpretation of EC measurements (Baldocchi et al., 1988; Foken and

Wichura, 1996), which magnify when estimates of NEP are integrated overtime (Moncrieff et al., 1997). Unfortunately, very few natural stands of vegetation meet these strict standards. Further, many of the more interesting science questions are associated with ecosystems that are on non-ideal terrain, situated in and among complex landscapes and when they are experiencing varying atmospheric conditions. In these non-ideal conditions the *Eddy Covariance* method is vulnerable to large and systematic bias error (Finnigan et al., 2003; Goulden et al., 1996). Partitioning techniques allow deriving *Gross Primary Production* from NEP measurements at EC flux station.

In order to characterize NEP for different ecosystems, networks of instruments and sites to measure eddy fluxes of $CO_2$, water and energy over a wide typology of ecosystems, climate zone and biome have been formed with the ultimate goal of facilitating the modeling of primary production globally. In 1997 a global network of collaborating regional networks FLUXNET[1] was consolidated to coordinate regional and global analysis of observations from micrometeorological tower sites. Today $CO_2$, water vapor fluxes and many ancillary meteorological, soil, and plant variables, are being measured at 500 sites spread world-wide Figure 2.1.

With this network, information on plant physiology, ecosystem metabolism, biological and biochemical processes, effects of disturbances, complex terrain, biodiversity, stand age, land use, land management (eg. irrigation, fertilization, thinning, grazing, prescribed burning etc.) and extreme event on carbon and water fluxes have been obtained.

---

[1] Website: http://www.fluxnet.ornl.gov/fluxnet/index.cfm

*Figure 2.1: FLUXNET micrometeorological tower sites spread world-wide*

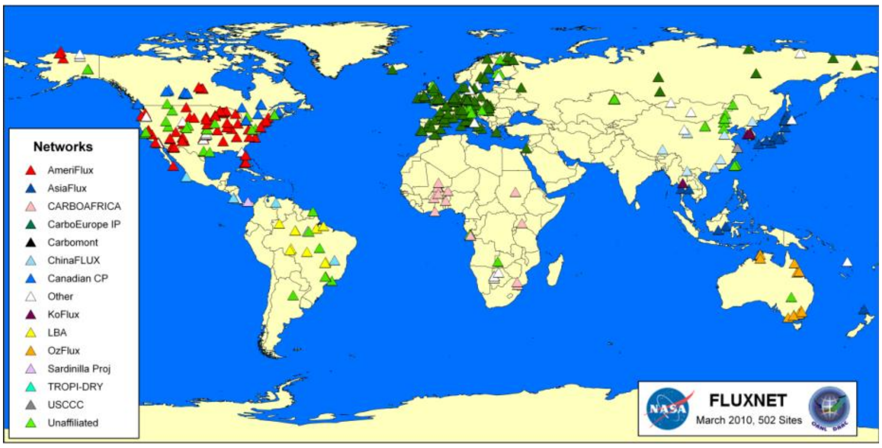

## 2.2 Remote Sensing techniques

*Remote Sensing* techniques employed in Earth science rely on the use of satellite-based observations that provide spatially continuous observations at global scale repeated in the time. RS has been widely proved to be a key tool for determining and classifying vegetation types, leaf pigment concentrations (Zarco-Tejada et al., 2002), abundance of other bio-chemical components (Curran, 1989) and estimation of physical properties of canopies (eg. leaf area index, leaf angle distribution etc.). Several researches have also shown the capabilities of satellite-based remote sensing data to provide information useful for carbon cycle modeling. For example carbon cycle models require parameterization of the land surface, which, in a spatially continuous mode and on a regularly basis, is only possible using remote sensing.

Most models, aimed at the estimation of photosynthetic rate or *Gross Primary Production* from RS data, are based on the concept of *Light-Use Efficiency* (Monteith, 1972; 1977) as explained in *Equation 1.1*. From a RS perspective, LUE models are attractive because their entire set of input parameters can in principle be derived from RS measurements (for a review see Hilker et al., 2008). The determination of *f*APAR from RS data has matured over a number of years supported by the close relationship between absorbed solar energy and *Vegetation Indices* exploiting the visible and near-infrared regions (Asrar et al., 1984; Tucker and Sellers, 1986) - such as the well-known *Normalized Difference Vegetation Index* (NDVI) (Rouse et al., 1974). However NDVI can be used to estimate the amount of light absorbed by a plant, but not the efficiency with which vegetation uses this to fix carbon. In fact NDVI measures the "*greenness*" of the vegetation and not photosynthesis itself.

Because of this the efficiency term in the LUE model is often assumed to be the same for all vegetation types. There is now considerable evidence to suggest that the efficiency with which plants fix carbon can vary with species, vegetation functional type, and in response to changes in environmental conditions (e.g. variations in temperature and water vapour pressure deficit). In fact, the magnitude of ε is fundamentally determined by the quantum efficiency of photosynthesis. This is known to be reduced by stress factors, such as extreme temperatures, direct sunlight, or shortage of water and nutrients.

When vegetation is exposed to a stressor green leaves, in the short-term (hours or days), remain green but reduce photosynthesis. Only at longer time scales, when prolonged stress causes premature senescence or abscission would stress therefore show as a change in NDVI. Undoubtedly, NDVI is especially useful for picking up seasonal and interannual variations in the overall 'condition of the canopy', especially in relation to drought (Lui et al., 1994; Sims et al., 2006), and relating these variations to the capacity of the canopy to photosynthesize.

New generation of *Remote Sensing* techniques offers the possibility to monitor the so-called *energy dissipation pathways* of vegetation (Meroni et al., 2008). Typically, part of the energy absorbed by chlorophyll (Chl) pigments is not used by the light reactions of photosynthesis, but it is dissipated as fluorescence (F) (re-emission of light at a longer wavelength than the absorbed one) and/or *non-photochemical quenching* (NPQ) related to the xanthophyll cycle (Björkman, 1995). This latter physiological mechanism of plants can be detected using the narrow-band *Photochemical Reflectance Index* (PRI) as reported in the study of Gamon et al. (1992). Therefore, these *energy dissipation pathways* are in competition with photochemical energy conversion for the use of absorbed light, thus F and

PRI are expected to provide an indirect assessment of photochemical efficiency.

Encouraged by the advent of *"fine"* resolution spectral measurement devices that allow measurement of canopy reflectance using narrow wavebands in the visible and near infrared region, estimation of ε (*Equation 1.1*) using RS techniques increased in the past decade. These technological advancements had improved the capabilities of monitoring the *energy dissipation pathways* of vegetation represented by heat dissipation (*xanthophyll cycle*) and the re-emission of *sun induced chlorophyll Fluorescence* (F). *Fluorescence* estimation requires a spectroradiometer with a "*ultra-fine*" resolution (about 0.1 nm) since the Fraunhofer lines exploitable for F measurement are typically 0.5 to 2 nm wide, while PRI can be investigated by traditional "fine" resolution sensors (2 to 10 nm). An overview of the processes that regulate the interaction of the light with vegetation and the remote sensing methods used to retrieve information for carbon assessment are reported in the following sections.

## 2.2.1 The reflected light

Optical Earth Observation Systems are typically able to measure the radiance reflected from the Earth surface in the solar domain (0.3-3 µm). In order to determinate properties of terrestrial vegetation from the remotely sensed signal, it is necessary to understand how vegetation interacts with the incoming radiation to generate the reflected signal. The nature of the reflection, in terms of its intensity, its spectral properties, and its spatial or angular properties, provides information about the surface being studied.

The interaction of light with plant canopies depends both on the radiative properties of the individual elements of the vegetation (leaves, stems, soils, water, etc.) and on the canopy architecture in relation to the angular distribution of the incident radiation and the orientation of the sensor.

Leaf optical properties (i.e. reflectance and transmission spectrums) are a function of both the concentration of light absorbing compounds (chlorophylls, carotenoids, water, cellulose, lignin, starch, proteins, etc.), and the internal scattering of light that is not absorbed or absorbed less efficiently. Leaves absorb a large proportion of incident radiation in the visible wavelengths (400-700 nm, with a dip/maximum in the green), while the greater part of radiation is scattered in the near infrared (NIR) region. In the visible wavelengths leaf spectral properties are governed by its chemical composition and in particular by the photosynthetic pigments (chlorophyll, carotenoids and flavonoids) content and composition. The most important pigment is the chlorophyll that accounts for almost all the absorption in the red and in the blue region. Absorption spectrums of the most significant pigments are reported in Figure 2.2.

*Figure 2.2: Absorption spectrums of the most significant pigments widely present in leaves. (http://www.uic.edu)*

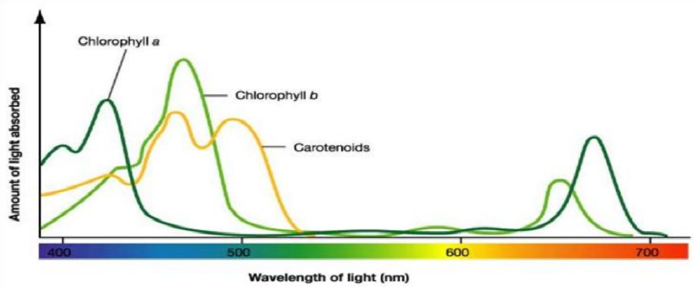

In contrast, in the near infrared region (700-1100 nm) biochemical absorptions are limited to the compounds typically found in dry leaves, primarily cellulose, lignin and other structural carbohydrates. Leaf reflectance in this region is determined by multiple scattering of photons within the leaf, related to the internal structure, fraction of air spaces, and air-water interfaces that refract light within leaves.

Finally, water absorption features dominate the middle (or shortwave) - infrared (1100-2500 nm). The primary and secondary absorptions of water in leaf reflectance are greatest in spectral bands centered at 1450, 1940, and 2500 nm, with important secondary absorptions at 980 nm, and 1240 nm (Carter, 1991).

Radiation reflected from and transmitted through vegetation elements can be specular or diffuse, depending on the characteristics of the elements itself and the direction of the incident radiation flux. An example of typical leaf reflectance and transmittance signatures measured in laboratory is reported in Figure 2.3.

*Figure 2.3: (a) Reflectance and transmittance of a Vitis vinifera L. leaf. Absorptance of the leaf is given by the difference between the two curves. (b) Typical reflectance signature of either dicotyledonous leaves (lettuce, potato, poplar, and grape vine) and conifer needles (Pinus contorta, Pseudotsuga menziesii, and Picea sitchensis) (data from the LOPEX93 experiment (Hosgood et al., 2005[2])).*

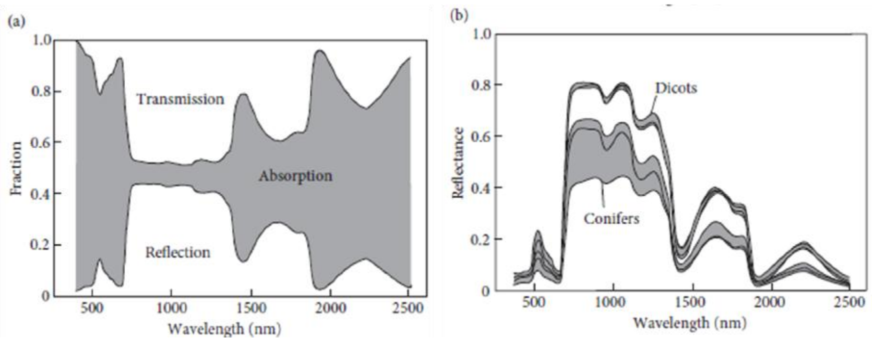

The characteristic absorption/scattering and hence reflectance features shown by different constituents of leaves provide a powerful means for obtaining information on leaf physical and chemical properties. The interaction of radiation with leaves depends also on the angle of incidence of radiation with respect to the leaf and further complication is that the arrangement of leaves to form a canopy modifies the canopy reflection.

Another features observable in the visible range is related to the detection of xanthophyll cycle, which represents an important photoprotection mechanism that allows plants to thermally dissipate (NPQ) the absorbed light energy that exceeds the photosynthetic demand. Although the exact mechanisms of NPQ are not completely understood, recent experimental works support the hypothesis that zeaxanthin formation, via the xanthophyll cycle pigments, is responsible for the majority of dissipation of the excess excitation energy (Demmig-Adams, 2003; Horton et al., 1996; Horton et al., 2005). Under excess light, violaxanthin is converted rapidly via the intermediate antheraxanthin to zeaxanthin (Figure 2.4, a), and this reaction is reversed under low light levels (i.e. epoxidation). The interconversion of the xanthophyll cycle pigments can be detected in leaves through a change (Bilger et al., 1989) in the absorbance at 505-515 nm or in the reflectance at 531 nm (Gamon et al., 1990)(Figure 2.4, b).

---

[2] Website: http://ies.jrc.ec.europa.eu/index.php?page=data-portals

*Figure 2.4: a) The xanthophyll cycle: When strong illumination occurs the violaxanthin is converted to antheraxanthin and zeaxanthin. This biochemical mechanism allows thermal dissipation of energy absorbed by leaf. b) Effect of Xantophyll cycle on leaf reflectance.*

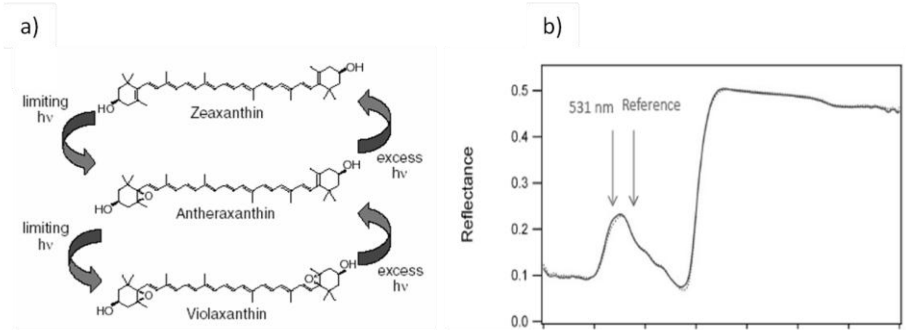

*Canopy Reflectance* (CR) results from the addition of the absorption and scattering processes that occur at the incident solar flux through the canopy. CR depends on the spectral properties of leaves, their amount and spatial distribution, direction of the incoming light flux (direct/diffuse), the orientation of the observer, spectral properties of background (soil).

Some of the many possible trajectories of radiation scattering and penetration in a plant canopy are illustrated in Figure 2.5. The incident sunlight may either be directly reflected back to the sky from a leaf (A), with a small fraction transmitted through the leaf, or else it may be involved in secondary (B), or even tertiary (C) reflections before finally being reflected back to the sky. Similarly, some of the reflections may involve the soil (D).

*Figure 2.5: (a) Illustration of some of the possible interactions of radiation with a plant canopy with randomly oriented leaves, showing the multiple scattering events. The incident sunlight may either be directly reflected back to the sky from a leaf (A), with a small fraction transmitted through the leaf, or else it may be involved in a secondary (B), or even tertiary (C) reflection before finally being reflected back to the sky. Similarly some of the reflections may involve the soil (D). (source: H. G Jones and R. A Vaughan, "Remote Sensing of Vegetation Principles, Techniques, and Applications", Oxford University Press).*

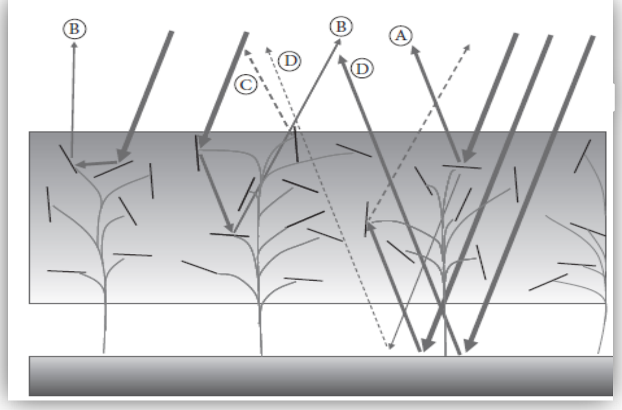

The most important structural parameters defining the architecture of a canopy are: i) *Leaf Area Index* (LAI, $m^2 \, m^{-2}$), the ratio of leaf area (one-sided) to the ground area and ii) *Leaf Angle Distribution* (LAD). These architectural parameters, LAI and LAD, affect canopy reflectance. In particular, an increase of LAI results in a general increase of absorption in the visible region of the *spectrum*, and an increase in scattering in the infrared region. LAD shows effects on the *Bidirectional Reflectance Distribution Function* (BRDF) of the canopy, because it affects the canopy directional reflectance as a function of illumination and viewing angles. Moreover LAD changes the gap probability through the canopy as a function of solar zenith and view angles, which determines the amount of radiation that will be intercepted by vegetation elements.

It follows that the characteristic combinations of these features in individual species gives obvious scope for distinguishing them on the basis of reflected radiation. At the same time, plant growth and development, as well as specific stresses, will change the structural and chemical characteristics of the plants, which can thus be inferred from the recorded spectral signature.

In order to extract quantitative information about canopy architectural and leaf biochemical parameters from remotely sensed data, different methodologies have been developed/tested. Several spectral indices, named *Vegetation Indexes*, VIs, have been developed to analyze remote sensing data. VIs are combinations of discrete spectral bands that maximize the sensitivity of the index to the investigated/requested canopy characteristic while minimizing the sensitivity to the unknown and unwanted canopy characteristics. Most of the *Vegetation Indices* are based on differential reflectance of energy by the vegetation in the red and near infrared regions. Such indices have been extensively used for land cover classification, climate and land-use-change detection, drought monitoring, to name just a few applications.

VIs have been used to estimate or predict various land surface biophysical variables. The *greenness* VIs measures the general quantity and vigor of green vegetation. They are combinations of reflectance measurements that are sensitive to the combined effects of leaf chlorophyll concentration, canopy leaf area, foliage clumping, and canopy architecture. These VIs are designed to provide a measure of the overall amount and quality of photosynthetic material in vegetation, which is essential for understanding the state of vegetation for any purpose. These VIs are an integrative measurement of these factors and are well correlated with the *f*APAR.

The most common used vegetation indices are ratios of single-band or linear-combined reflectances. Most of the ratio-based vegetation indices use the red and the near infrared spectral bands. The first ratio-based vegetation index was the *Simple Ratio,* SR (Jordan, 1969):

$$SR = \frac{r_{NIR}}{r_{RED}} \qquad \textit{Equation 2.2}$$

where $r_{NIR}$ and $r_{RED}$ are reflectance values of Red and Near Infrared light received at the sensors.

The most well-known and frequently used VI is the *Normalized Difference Vegetation Index*, NDVI (Rouse et al., 1974):

$$NDVI = \frac{r_{NIR} - r_{RED}}{r_{NIR} + r_{RED}} = \frac{SR-1}{SR+1} \qquad \textit{Equation 2.3}$$

The SR and NDVI are built on the observation that chlorophyll in green leaves strongly absorbs light in the Red, with maximum absorption at about

690 nm, while the cell walls strongly scatter (reflect and transmit) light in the NIR region (about 850 nm).

Based on differential spectral properties of vegetation in red and NIR regions, more complex VIs (EVI, SAVI, MTCI etc.) have been formulated. For example, the *Enhanced Vegetation Index*, EVI (Huete et al., 2002) is calculated as:

$$EVI = G \frac{r_{NIR} - r_{RED}}{r_{NIR} + C_1\, r_{RED} - C_2\, r_{BLUE} + \mathrm{L}} \qquad \textit{Equation 2.4}$$

where L is the canopy background (soil) adjustment factor and $C_1$, $C_2$ are the coefficients of the aerosol resistance term, which uses the blue band to correct for aerosol influences in the red band. The coefficients adopted in the EVI algorithm are, L=1, C1=6, C2=7.5, and G (gain factor)=2.5. The EVI does not ”saturate" as rapidly as NDVI in dense vegetation and it has been shown to be highly correlated with photosynthesis and plant transpiration in a number of studies.

The *Soil-Adjusted Vegetation Index*, SAVI (Huete, 1988) is a *Vegetation Index* that accounts for, and minimizes, the soil optical effect on the canopy reflectances. The SAVI equation introduces a coefficient (L) that should vary with vegetation density to eliminate the effects from background soils (Equation 2.5).

$$SAVI = \frac{(r_{NIR} - r_{RED})\,(1+L)}{r_{NIR} + r_{RED} + L} \qquad \textit{Equation 2.5}$$

Finally, with the advent of hyperspectral sensors (i.e. sensors providing a set of high spectral resolution contiguous bands) a number of narrow-band VIs has been proposed to estimate plant pigment content. Among these the *Meris Terrestrial Chlorophyll vegetation Index*, MTCI (Dash and Curran, 2004), has recently shown some potential in GPP monitoring (Rossini et al. 2010, Wu et al. 2009, Harris et al. 2010). This index is specifically designed for canopy chlorophyll content estimation and it is calculated as:

$$MTCI = \frac{r_{753} - r_{708}}{r_{708} - r_{631}} \qquad \textit{Equation 2.6}$$

Several studies have reported significant correlations between GPP and greenness or chlorophyll-related indices because chlorophyll is related to the presence of photosynthetic biomass, which is essential for primary productivity and thus conceptually related to GPP. However, the limitation behind this kind of VIs is that variations in GPP due to short-term (hours to days) environmental stresses, such as high temperature and irradiance, cannot be estimated by these indices alone, until these stresses affect canopy greenness (i.e. canopy Chl content). Thus they can be empirical estimators of photosynthesis or primary productivity for certain ecosystems because they are related to potential carbon gain in the absence of constraints on photosynthesis. However, considerable uncertainty still remains about how much of this capacity is realized in practice because the photosynthetic rate may varies significantly between plants, environmental conditions, and ecosystems due to varying environmental constraints (Garbulsky et al., 2010).

Different studies conducted during the 1990s show the capability to accurately assess the photosynthetic efficiency based on concurrent xanthophyll pigment changes (Filella et al., 1996; Gamon et al., 1990; Gamon et al., 1992; Gamon et al., 1997; Gamon and Surfus, 1999; Penuelas et al., 1995; Penuelas et al., 1997). This approach is based on the activation of the xanthophyll cycle which is linked to heat dissipation (Demmig-Adams, 2003) of excess energy absorbed by vegetation. Since the reflectance at 531 nm is functionally related to the de-epoxidation state of the xanthophyll cycle (Gamon et al., 1990; Gamon et al., 1992; Peñuelas et al., 1995), the *Photochemical Reflectance Index*, PRI, typically calculated as:

$$PRI = \frac{r_{531} - r_{570}}{r_{531} + r_{570}} \qquad \textit{Equation 2.7}$$

where *r* is the reflectance at the specified wavelength (nm), was developed to remotely assess photosynthetic efficiency using narrow-band reflectance (Gamon et al., 1992; Peñuelas et al., 1995).

## 2.2.2 The emitted light (fluorescence)

Until now, most of the information about vegetation condition collected using *Remote Sensing* techniques has come from the analysis of the reflected light in the solar domain. Additional information about vegetation GPP in the visible and near infrared wavelength range can be gained with the *sun-induced chlorophyll Fluorescence* (F). When vegetation absorbs more light energy than can be utilized productively by photosynthesis, part of this excess energy can be re-emitted as fluorescence (re-emission of light at a longer wavelength than for excitation).Together with the other dissipative pathway (NPQ), F competes with photosynthesis for the use of the absorbed light.

The F emission spectrum of a leaf exhibits two peaks in the red and near infrared regions, with maxima around 690 nm and 740 nm (Buschmann, 2007; Lichtenthaler, 1987)(Figure 2.6 A). The ratio of the red to the far-red chlorophyll fluorescence maximum primarily depends on the leaf chlorophyll content and to a lower degree also on the photosynthetic activity.

Under solar illumination plants fluorescence (F) adds a weak signal to reflected solar radiation. If both fluorescence emission and surface reflectance are assumed to follow Lambert's law, the radiance upwelling from vegetation (L) at ground level is therefore composed of two coupled contributions, one reflected (r $E^{TOT}/\pi$) and the other emitted (F):

$$L(\lambda) = \frac{r(\lambda)E^{TOT}(\lambda)}{\pi} + F(\lambda) \qquad \textit{Equation 2.8}$$

where λ is wavelength, r is reflectance (free of the emission component), and $E^{TOT}$ is total irradiance (direct/diffuse) incident on the target. Even though F contributes to the signal detected by a remote sensor (Figure 2.6, B), its magnitude is small (1–5% of the reflected radiation in the near infrared) thus making the decoupling of the two contributions difficult.

*Figure 2.6: A): F spectrum in the region between 650 and 800 nm, the two emission peaks are centered at 690 nm and 740 nm respectively. B): The actual reflectance (black curve) was computed as the ratio of the reflected and incident fluxes; the apparent reflectance (red curve) was computed as the ratio of the total upwelling flux (reflection plus F) and the incident flux. The difference between the two quantities is highlighted in the grey boxes, showing the responses surrounding the F emission maxima (vertical dotted lines).*

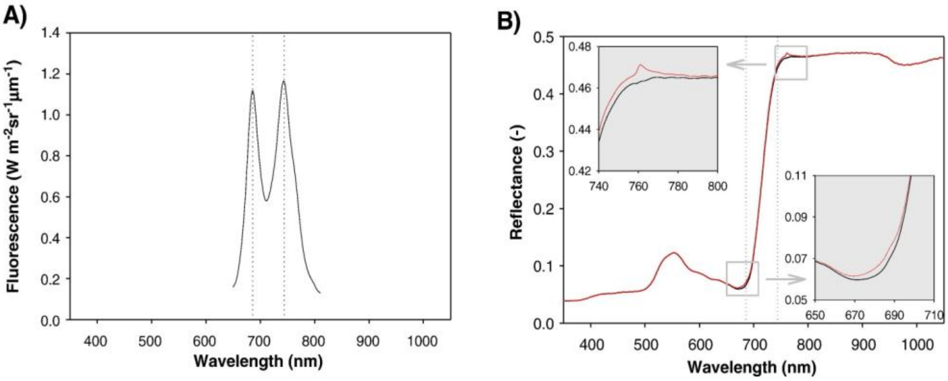

Zarco-Tejada et al. (2000) first recognized the effect of F on r and demonstrated that it is possible to detect the F signal using r measurements. In fact, the reflectance factor usually computed by the RS community as the ratio between upwelling and incident fluxes is indeed polluted by the F contribution:

$$r^* = \frac{\pi L}{E^{TOT}} = r + \frac{\pi F}{E^{TOT}}$$

*Equation 2.9*

This quantity, referred here as apparent reflectance, r*, differs from the pure reflectance (r) as indicated by the right hand side of Equation 2.9 and as shown in Figure 2.6.

The F signal can be detected passively in narrow dark lines of the solar and atmospheric spectrum in which irradiance is strongly reduced (the so-called *Fraunhofer lines*). In the visible and near-infrared, the solar spectrum at ground level exhibits three main "*Fraunhofer*" features which have been exploited for F estimation: Hα due to hydrogen (H) absorption in the solar atmosphere (centered at 656.4 nm) and two telluric oxygen ($O_2$) absorption bands in the Earth atmosphere, $O_2$-B (687.0 nm) and $O_2$-A (760.4 nm).

The incident at-surface irradiance at different spectral resolutions (0.005, 0.1 and 1.0 nm Full Width at Half Maximum, FWHM) and at the spectral regions around these three absorption features is shown in Fig. 2.7.

Irradiance data were simulated by means of the Matrix Operator Model (MOMO) (Fell and Fischer, 2001). Among other inputs, the sun zenith angle was set to 30°, with a mid-latitude summer atmosphere, the surface at sea level, and the aerosol optical thickness at 550 nm equal to 0.2. Resampling to the different spectral resolutions was performed assuming Gaussian-like spectral response functions with the given FWHM.

*Figure 2.7: Incident irradiance ($E^{TOT}$) at ground level at the three absorption lines normally used for F retrieval and at three different spectral resolutions (0.005, 0.1 and 1.0 nm for the green, red and blue curves, respectively). Data were simulated by the MOMO atmospheric radiative transfer code. The three lines are situated at 656.4 nm (Hα), 687.0 nm ($O_2$-B) and 760.4 nm ($O_2$-A).*

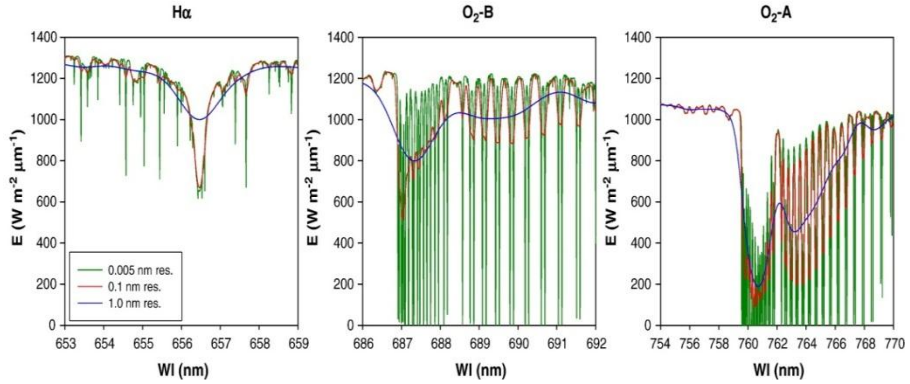

The $O_2$ absorption bands were used more extensively than the H feature because, when observed with typical resolutions from a tenth of a nanometer to a few nanometers they appear wider and deeper. Moreover, they are spectrally closer to the peaks of the F emission spectrum positioned at about 690 and 740 nm thus making the contribution of F to the overall upwelling signal more significant. The main drawbacks associated with the use of the $O_2$ absorption features for F retrieval are that the shape and width of the features are subject to spatial and temporal variations because they depend on the atmospheric state, the illumination and observation geometry, and because the emitted F is re-absorbed along the upward atmospheric path which diminishes the signal to be measured by an airborne or spaceborne instrument.

The rationale for the passive estimation of F is therefore to exploit these dark bands by measuring to what extent the “wells” are filled by F relative to the reflectance continuum (Elachi, 1987). The $O_2$-A band was exploited in this work because it is larger (in terms of bandwidth) and deeper (in terms of attenuation with respect to continuum) than the $O_2$-B band. At the $O_2$-A band incident radiation at ground level is attenuated by up to more than 90% when measured with a resolution of about 0.1 nm. With such a resolution, details of the internal structure and narrow features of the $O_2$-A band can be observed in the incident solar radiance spectrum collected with a high spectral resolution spectrometer Figure 2.8.

*Figure 2.8: Apparent reflectance factor (r*, black curve) at the $O_2$-A band calculated from incident and upwelling radiances (red and green curves, respectively). Measurements were collected early in the morning with an HR4000 spectrometer (OceanOptics, USA) characterized by a FWHM of 0.1 nm*

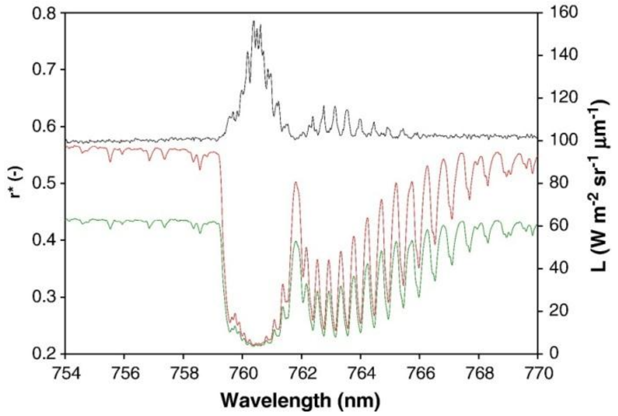

Figure 2.8 also demonstrates that the reflectance computed as the ratio of the upwelling and downwelling radiances according to Equation 2.9 is indeed an apparent reflectance polluted by the F contribution from the infilling of the $O_2$-A band producing the peak at 760 nm. Several methods have been developed to quantify F. In the next paragraphs the most widely used methods: i) *Fraunhofer Line Discriminator* (FLD); ii) *Spectral Fitting Method* (SFM) are briefly described.

### *The FLD method*

The FLD relies on two flux measurements, one inside and one outside a *Fraunhofer line*. The magnitude of F is deduced by comparing the signal measured inside the dark line ($\lambda_{in}$, e.g. 760 for $O_2$-A) with the signal measured in a nearby wavelength ($\lambda_{out}$, e.g. 758 nm) that contains the entire solar background irradiance. In practice, the FLD method requires measurement of incident solar irradiance (E, Figure 2.9) and target radiance

(L, Figure 2.9) in $\lambda_{in}$ and $\lambda_{out}$ (the bottom and shoulder of the well) to solve the following system of equations:

$$L(\lambda_{in}) = \frac{r(\lambda_{in})\,E^{TOT}(\lambda_{in})}{\pi} + F(\lambda_{in}) \qquad \textit{Equation 2.10a}$$

$$L(\lambda_{out}) = \frac{r(\lambda_{out})\,E^{TOT}(\lambda_{out})}{\pi} + F(\lambda_{out}) \qquad \textit{Equation 2.10b}$$

*Figure 2.9: The standard FLD method. A): Incident solar irradiance spectrum at the $O_2$-A band. B): Upwelling fluxes: the total radiance observed over the vegetated target (blue curve) is made up of the sum of F (red area) and pure reflection (green curve). The blue curves in A) and B) are the only measurable quantities.*

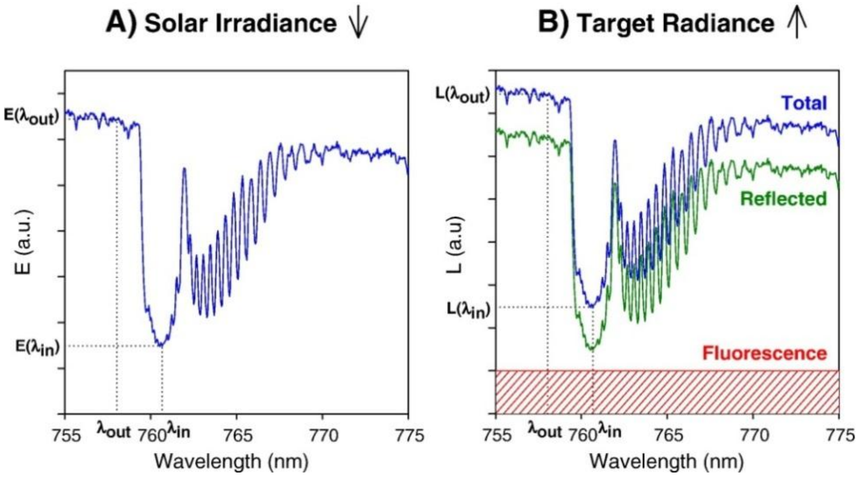

Solar-induced Chl fluorescence is then computed on the assumption that r and F remain constant at the two close wavelengths involved in the measurement:

$$\rho = \frac{L(\lambda_{out}) - L(\lambda_{in})}{E^{TOT}(\lambda_{out}) - E^{TOT}(\lambda_{in})} \qquad \textit{Equation 2.11}$$

$$F = \frac{E^{TOT}(\lambda_{out})\, L(\lambda_{in}) - L(\lambda_{out})\, E^{TOT}(\lambda_{in})}{E^{TOT}(\lambda_{out}) - E^{TOT}(\lambda_{in})} \qquad \textit{Equation 2.12}$$

These equations form the basis of the FLD method exploited by the majority of studies. This method is simple and requires radiance measurements in only two spectral channels. The main drawback of the method is that, the values of r and F are far from being constant in the spectral rang considered.

***The SFM method***

*The Fraunhofer Line Discriminator* (FLD) principle has long been considered as the reference method to quantify solar-induced chlorophyll fluorescence (F) from passive remote sensing measurements. Recently, alternative retrieval algorithms based on the spectral fitting of hyperspectral radiance observations, *Spectral Fitting Method* (SFM), have been proposed by (Meroni et al., 2010). SFM are based on the assumption that the spectral variations of r and F in the selected spectral interval can be described by a polynomial or other appropriate mathematical functions. The measured upwelling radiance, L(λ), is therefore expressed as:

$$\begin{aligned} L(\lambda) = {} & \frac{r_{MOD}(\lambda) E^{TOT}(\lambda)}{\pi} + F_{MOD}(\lambda) + \varepsilon(\lambda) \\ & = L_{MOD}(\lambda) + F_{MOD}(\lambda) + \varepsilon(\lambda) \end{aligned}$$

$$\lambda \in [\lambda_1 - \lambda_2] \qquad \textit{Equation 2.13}$$

where $r_{MOD}(\lambda)$ and $F_{MOD}(\lambda)$ are the mathematical functions used to describe the two key variables, $L_{MOD}(\lambda)$ is the modeled radiance and ε(λ) is the difference between observed and modeled radiance, which represents the modeling error at each wavelength. (Meroni and Colombo, 2006) used a SFM in which linear functions were used to describe r(λ) and F(λ) of *Equation 2.12* in a restricted spectral range around the $O_2$–A absorption band. With a large number of contiguous spectral observations provided by very high spectral resolution spectrometers (e.g., FWHM=0.1 nm), an overdetermined bilinear system was formed with *Equation 2.12* and the four unknowns (i.e., gain and offset of the linear r(λ) and F(λ) functions) were estimated. In summary, the FLD assumptions of constant r and F are replaced by SFM assumptions of linear/quadratic variation of the two variables.

An example of results of the decoupling achieved with SFMs is illustrated in Figure 2.10. Figure 2.10 (left panel) shows the observed incident and upwelling radiance over a vegetated target, and the apparent r (r*), ratio between the two fluxes) around the $O_2$-A band. Reflectance is indicated here as apparent because it is indeed polluted by the F contribution as shown by the in-filling of the absorption well, which causes the peak in correspondence to the well bottom at about 760.6 nm.

*Figure 2.10: Left: incident and upwelling radiance measured on a vegetated target (E/π and L, respectively), and the resulting apparent r. Right: modeled F and r, $F_{MOD}$ and $r_{MOD}$, resulting from the application of the bilinear SFM. Measurements were collected over a winter wheat canopy with a HR4000 spectrometer (OceanOptics, USA) characterized by a spectral resolution of 0.13 nm and a sampling interval of 0.02 nm.*

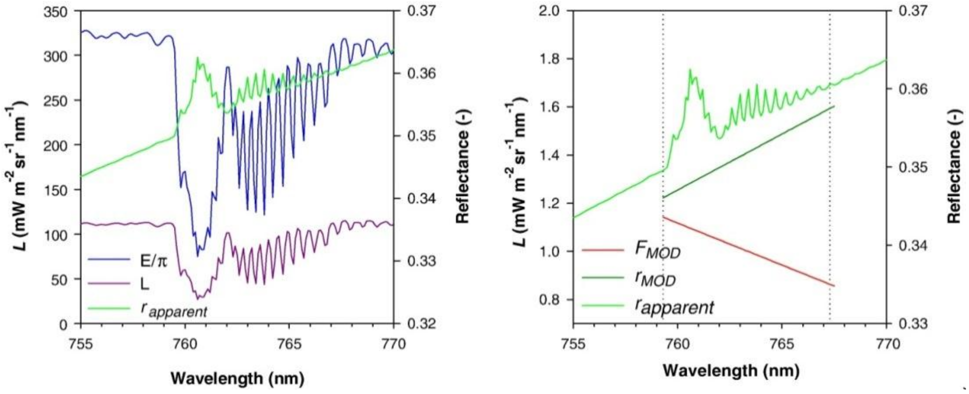

Figure 2.10 (right panel) shows the modeled $r_{MOD}$ and $F_{MOD}$ functions obtained after optimizing the bilinear SFM model over the spectral interval [759.3 nm, 767.5 nm], encompassing the major absorption well and its frequency features. Figure 2.10 also shows that the modeled r (free of F) differs from the apparent one in both magnitude and shape since the slope of $r_{MOD}$ is larger than that of r-apparent.

### 2.2.3 RS instrumentation currently available

Recent studies have related the satellite PRI signal to flux tower estimates of ε. Middleton et al. (2004) and Rahman et al. (2004) used single orbit acquisitions from MODIS to estimate PRI for an Aspen stand in boreal Canada and a secondary deciduous forest in the United States. Drolet et al. (2005) followed this up with a thorough study utilizing MODIS scenes over an aspen site in Canada. In their study they highlighted the variability in the PRI and ε during the MODIS overpasses and strong statistical correlations between PRI and ε calculated from a micrometeorological flux tower.

Instead, currently, it is not yet available a space sensor useful for detecting the *sun-induced chlorophyll Fluorescence*. Recently, on 27 November 2010, the satellite mission FLEX (*Fluorescence Experiment*) by the *European Space Agency* (ESA) has been selected for further development to 'Phase-A/B1'. This phase includes feasibility study and further consolidation of the various components that make up a satellite mission. The FLEX mission aims to provide global maps of vegetation fluorescence, which can be converted into an indicator of photosynthetic activity. These data would improve our understanding of how much carbon is stored in plants and their role in the carbon and water cycle. Despite of a number of Earth Observation systems characterized by different spectral, spatial and temporal resolution, this approach nowadays suffers some limitations concerning:

- the coarse spatial resolution typically provided by current satellite sensor;
- temporal resolution;
- spectral bands (width and wavelength) available.

For a better comprehension of the link between photosynthesis and optical signals, a growing number of studies has recently focused on the collection of large datasets of repeated field spectroscopy observations in the sampling area of EC flux towers (i.e., the footprint) over diurnal cycles or longer time scales (e.g. with weekly measurements to get a seasonal trend) (Damm et al., 2010; Inoue et al., 2008; Rascher et al., 2009; Rossini et al., 2010). Such EC measurement stations provide local scale information that can be up-scaled using remote sensing (RS) data for mapping the biophysical and biogeochemical processes from regional to global scale (e.g. Running et al., 2004). The acquisition of spectral measurements paired with simultaneous carbon flux data is a valuable approach to address the scale mismatch between satellite remote sensing and flux measurements for a better understanding of the relation between photosynthesis and optical signals.

For such reason few research groups initiated automatic tower-based spectral measurements using different devices. With such setups, spectral instruments are installed in the field on a flux station (or in its proximity) and are operated automatically for long periods (i.e. months to years). A short overview about the instrumentation able of autonomous, continuous and long-term spectral measurements currently available is reported below. Different approaches have been investigated: i) filtered photodiode-based sensors that collect few wide-wavebands; ii) non-imaging spectrometer sensors capable of collecting hundreds of continuous narrow-bands.

The first approach is based on the consideration that it may only be necessary to measure a limited number of wavebands to model canopy GPP. The sensor configuration typically employed provides measurement of spectral bands used to calculate NDVI and PRI (Garrity et al., 2010; Wohlfahrt et al., 2010). The installation of these sensors at EC flux towers is simple, relatively low-cost and requires low maintenance. Two different sensor units are required to measure downwelling and upwelling light fluxes. Usually the upward pointing probe is equipped with a cosine-receptor (diffuser), while the Field of View (FOV) of the downward pointing probe can be conical-like (10-25° are widely used), or equipped with a cosine-receptor. In order to accurately assess the reflectance factor of the investigated wavebands, a thorough cross-calibration of upward and downward sensors is required.

The non-imaging spectrometer sensors instead are capable of collecting continuous narrow bands in the visible and near-infrared spectral range. These instruments provide both sky irradiance and canopy radiance measurements to allow continuous calculation of canopy reflectance spectrums. A list of such instruments is reported in Table 2.1.

*Table 2.1: List and main features of instrumentations currently available for automatic tower-based spectral measurements. Instrument spectral range and spectral resolution of spectrums collected by different detectors (spectrometers) employed, the computed reflectance factor (it depends by instrument FOV), the possibility of multiangular observations, radiometric indices calculated and radiometric calibration approach are reported.*

| **Reference** | **Name** | **Range (nm)** | **Resolution (FWHM)** | **Detector** | **Reflectance (FOV)** | **Indices** | **Radiometric Calibration** |
|---|---|---|---|---|---|---|---|
| (Leuning et al., 2006) | MAS | 300-1150 | *fine (<10 nm)* | Unispec | HCRF (10°) | VIs, PRI | Cross-calibration |
| (Gamon et al., 2006) | Tram system | 310-1130 | *Fine (<10 nm)* | UniSpec | HCRF (20°) | VIs, PRI | Cross-calibration |
| (Hilker et al., 2010) | AMSPEC | | *Fine (<10 nm)* | UniSpec | HCRF (20°) | VIs, PRI | Cross-calibration |
| (Nakaji et al., 2008) | | 350-1050 | *fine (10 nm)* | MS-700 | BHR (~180°) | VIs, PRI | Cross-calibration |
| (Daumard et al., 2010) | TriFLEX | 300-900 | *fine (~2 nm)* | OceanOptics (HR2000+) | HCRF (25°) | VIs, PRI, | absolute |
| | | 630-815 | *ultra-fine (0.5 nm)* | | | F@687, F@760 | |

Leuning et al. (2006) proposed a novel optical periscope that is combined with a spectrometer to measure the spectral reflectance of a forest canopy at four azimuth angles at hourly intervals every day of the year. The instrument, known as the *Multi-Angle Spectrometer* (MAS), consists of two major components: an optical periscope mounted on top of the mast and a Unispec-SC spectrometer (PP Systems, Haverhill, MA, USA) and associated electronics mounted 2 m below the periscope and connected to it via electrical and fiber-optic cables. Figure 2.11 shows the periscope that samples incoming radiation and radiation reflected from the forest canopy in the selected azimuth directions.

*Figure 2.11: Mechanical design of the optical periscope of Multi-Angle Spectrometer (MAS) (source: Leuning et al., 2006).*

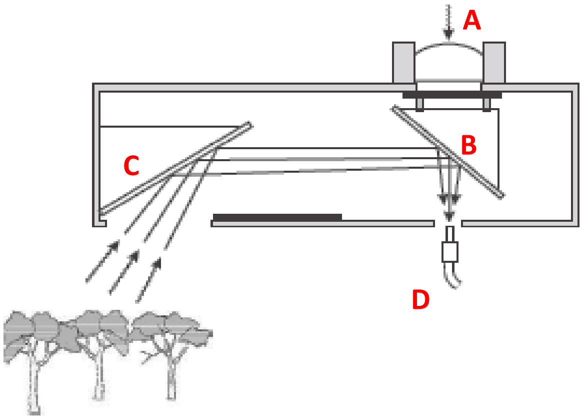

On top of the periscope a cosine-corrected hemispherical diffuser (A) samples incoming irradiance. A moveable mirror (B) in the periscope is positioned so that the sky port is blocked and light from the main mirror (C) is reflected onto the optical fiber of the spectrometer. Instrument FOV is of 10° and measurements are collected with a zenith angle of 58°. When MAS is mounted at 70 m height, with a forest canopy of 40 m, the sampled area is about 19 m in the radial direction and 8 m in the azimuth direction. This instrument can be defined as “single-beam” (Milton et al., 2009) because the same detector measures both the incoming irradiance ($E^{TOT}$) and radiance upwelling ($L^{s}$) from the sampling area. A limitation of single-beam devices is that identical illumination conditions at the time of $E^{TOT}$ and $L^{S}$ measurements are assumed to compute the reflectance factor.

On the contrary "dual-beam" instruments use two different detectors to simultaneously measure $E^{TOT}$ and $L^{S}$. This kind of devices overcome the assumption of identical illumination conditions at the time of $E^{TOT}$ and $L^{S}$ measurements and thus can acquire more reliable measurements than their single-beam counterparts with varying illumination condition. However the two detectors have to be very well spectrally and radiometrically matched (Milton et al., 2009) in order to obtain reliable measurements.

An example of dual-beam instruments is the tram system developed by Gamon et al. (2006). It consists of a dual-detector spectrometer (Unispec-DC, PP Systems, Haverhill, MA, USA) mounted on a robotic cart for mobile sampling of ecosystem spectral reflectance. A schematic view of the tram system, showing the cart mounted on an elevated rail, is depicted in Figure 2.12.

*Figure 2.12: Tram system developed by Gamon et al. (2006) consists of a Unispec dual-detector spectrometer mounted on a robotic cart for mobile sampling of ecosystem spectral reflectance. a) image of the system installed in field; b) schematic view of instrument measurements.*

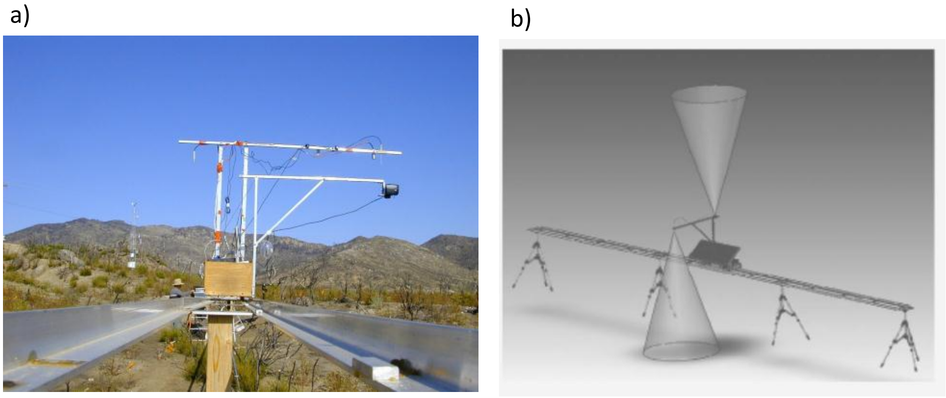
a)
b)

Using the upward- and downward-pointing foreoptics, a dual-detector spectrometer enables simultaneous sampling of upwelling and downwelling radiation (illustrated by cones), providing "on-the-fly" calculation of spectral reflectance. The upward looking probe is fitted with a cosine head ("reference" channel), while in typical usage the downward-looking channel is fitted with field of view restrictor that limits the FOV to approximately 20° (e.g. from a distance of 3 m, this samples a region on the ground of approximately 1 m diameter). The tram rail is approximately 100 m long and it is typically placed near the footprint of EC towers in order to spatially characterize heterogeneity of sampled area.

Other device employing the "dual-beam" approach is the *Automated Multiangular Spectroradiometer* system AMSPEC II (Hilker et al., 2010)(Figure 2.13). The instrument is featured by a motor-driven probe that allows observations in a 290° view area around the tower (the 70° that cannot be observed are due to obstruction by the tower).

*Figure 2.13: The AMSPEC II system developed by Hilker et al. (2010). A) image of the instrument installed on EC flux tower; B) schematic view of AMSPEC II installation and footprint.*

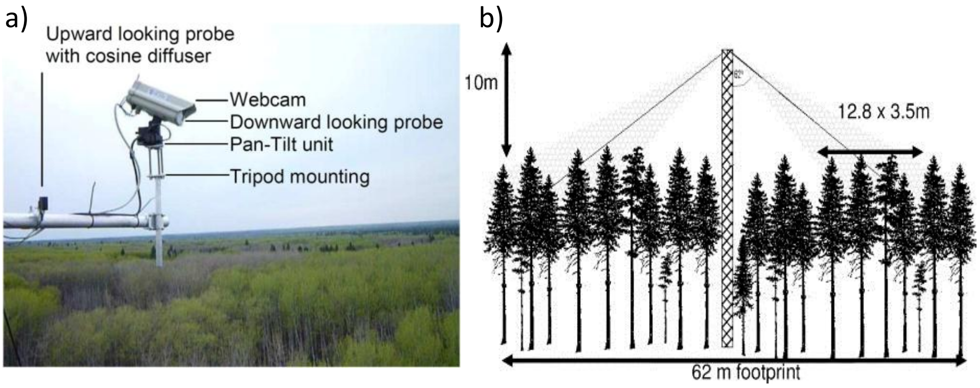

To allow sampling under varying sky conditions the spectrometer used is a Unispec-DC (PP Systems, Amesbury, MA, USA), so canopy reflectance is obtained from simultaneous measurements of solar irradiance and radiance, sampled every 5 s from sunrise to sunset. The upward looking probe is equipped with a cosine receptor (PP-Systems) to correct sky irradiance measurements for varying solar altitudes. The downward looking probe measures canopy radiance at varying zenith and azimuth angles to account for reflectance bidirectional behavior of investigated canopy. Multiangular measurements, such as those provided by MAS and AMSPEC systems, can be used to describe the anisotropy of the vegetation surface and to characterize VIs and PRI as a function of the sun–observer geometry. Furthermore this approach may be very useful to better understand the relationship between canopy architecture (eg. bidirectional effects, canopy shading) and ε.

Nakaji et al.(2008) obtained unattended, continuous reflectance measurements of different forests (Japanese latch, Japanese cypress, Hybrid larch and dwarf bamboo) using hemispherical spectroradiometers mounted on the monitoring flux towers. Two spectroradiometers (MS-700, Eko instruments, Japan) were held vertically on the upper and lower sides of a horizontal boom which jutted out from the tower top. Spectral reflectance of the canopy was derived from the upward flux divided by the downward flux density. The downward- and upward-pointing FOV are hemispherical allowing the computation of the *BiHemispherical Reflectance Factor* (BHR) (Schaepman-Strub et al., 2006), on the contrary MAS, tram-system and AMSPEC characterized by a conical downlooking FOV allow the determination of the *Hemispherical Conical Reflectance Factor* (HCRF) (Schaepman-Strub et al., 2006). All these automatic systems are characterized by a "*fine"* spectral resolution, corresponding to a "fine" spectral resolution (i.e. 1-3 nm and however < 10 nm), suitable for the computation of vegetation indices, including PRI.

The only instrument that meets the spectral requirements for measuring the *sun-induced chlorophyll Fluorescence* was developed by Daumard et al. (2010). This instrument, named TriFLEX (Figure 2.14), is designed for continuous measurement of fluorescence in the oxygen A and B absorption bands. TriFLEX uses two spectrometers (HR2000+, Ocean Optics, Dudenin, FL) to measure simultaneously irradiance and vegetation radiance spectra in 630–815 nm spectral range with "*ultra-fine*" resolution (FWHM ~ 0.1 nm). A third spectrometer (HR2000+, Ocean Optics) measures "*fine*" resolution vegetation radiance on the spectral range 300–900 nm. The data produced are the radiances of the target, the fluorescence flux at 687 and 760 nm, and several vegetation indexes, including PRI and NDVI. With TriFLEX instrument, the measurements of the $O_2$ band depth are made in parallel for both reference and vegetation. Cross-calibration is performed every 20 min to match the two spectrometer responses.

*Figure 2.14: TriFLEX instrument. Sp1 is a "fine" resolution spectrometer (300–900 nm, FWHM ~2 nm). Sp2 and Sp3 are two identical "ultra-fine" resolution spectrometers (630–815 nm, FWHM ~0.5nm). Sp2 acquires the radiance from the vegetation and Sp3 acquires the irradiance by continuously measuring the radiance from a reference board (see Sp3 FOV on the top left panel). The reference board can be rotated from default position to the calibration position (see top left panel) for cross-calibration purposes.*

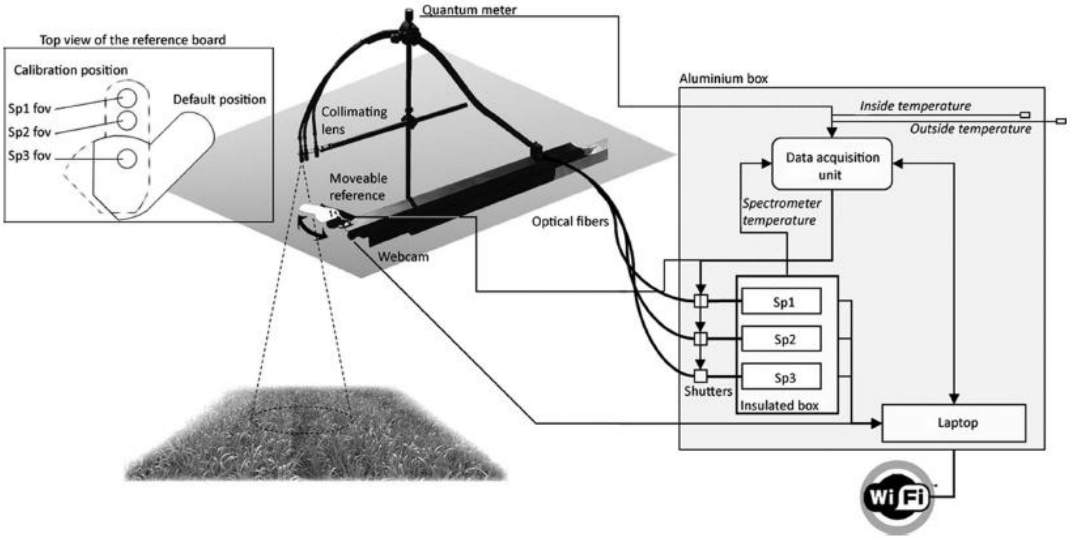

# Bibliography

Asrar, G., Fuchs, M., Kanemasu, E.T. and Hatfield, J.L., 1984. Estimating absorbed photosynthetic radiation and Leaf Area Index from spectral reflectance in wheat. Agronomy Journal, 76: 300–306.

Baldocchi, D., Falge, E. and Wilson, K., 2001. A spectral analysis of biosphere-atmosphere trace gas flux densities and meteorological variables across hour to multi-year time scales. Agricultural and Forest Meteorology, 107(1): 1-27.

Baldocchi, D., Hicks, B.B. and Meyers, T.P., 1988. Measuring biosphere–atmosphere exchanges of biologically related gases with micrometeorological methods. Ecology, 69: 1331-1340.

Baldocchi, D., Valentini, R., Running, S., Oechel, W. and Dahlman, R., 1996. Strategies for measuring and modelling carbon dioxide and water vapour fluxes over terrestrial ecosystems. Global Change Biology, 2(3): 159-168.

Baldocchi, D.D., 2003. Assessing the eddy covariance technique for evaluating carbon dioxide exchange rates of ecosystems: past, present and future. Global Change Biology, 9(4): 479-492.

Bilger, W., Bjorkman, O. and Thayer, S.S., 1989. Light-induced spectral absorbance changes in relation to photosynthesis and the epoxidation state of xanthophyll cycle components in cotton leaves. Plant Physiology 91: 542-551.

Björkman, O.D.-A., B., 1995. Regulation of photosynthetic light energy capture, conversion, and dissipation in leaves of higher plants. Ecophysiology of Photosynthesis: pp. 17-47.

Buschmann, C., 2007. Variability and application of the chlorophyll fluorescence emission ratio red/far-red of leaves. Photosynthesis Research, 92(2): 261-271.

Chen, J.M., Liu, J., Leblanc, S.G., Lacaze, R. and Roujean, J.L., 2003. Multi-angular optical remote sensing for assessing vegetation structure and carbon absorption. Remote Sensing of Environment, 84(4): 516-525.

Curran, P.J., 1989. Remote-Sensing of Foliar Chemistry. Remote Sensing of Environment, 30(3): 271-278.

Damm, A. et al., 2010. Remote sensing of sun induced fluorescence to improve modelling of diurnal courses of Gross Primary Production (GPP). Global Change Biology, 16(1): 171-186.

Dash, J. and Curran, P.J., 2004. The MERIS terrestrial chlorophyll index. International Journal of Remote Sensing, 25(23): 5403-5413.

Daumard, F. et al., 2010. A Field Platform for Continuous Measurement of Canopy Fluorescence. Ieee Transactions on Geoscience and Remote Sensing, 48(9): 3358-3368.

Demmig-Adams, B., 2003. Linking the xanthophyll cycle with thermal energy dissipation. Photosynthesis Research, 76(1-3): 73-80.

Denman, K.e.a., 2007. Couplings Between Changes in the Climate System and Biogeochemistry, IPCC, Climate Change 2007: The Physical Science Basis, Contribution of Working Group I to the Fourth Assessment Report of the Intergovernmental Panel on Climate Change [Solomon, S., D. Qin, M. Manning, Z. Chen, M. Marquis, K. Averyt, M. Tignor and H. Miller (eds.)]. Cambridge University Press.

Drolet, G.G. et al., 2005. A MODIS-derived photochemical reflectance index to detect inter-annual variations in the photosynthetic light-use efficiency of a boreal deciduous forest. Remote Sensing of Environment, 98(2-3): 212-224.

Elachi, C. (Editor), 1987. Introduction to the Physics and Techniques of Remote Sensing. Chichester, New York, Brisbane, Toronto, Singapore: John Wile.

Fell, F. and Fischer, J., 2001. Numerical simulation of the light field in the atmosphere-ocean system using the matrix-operator method. Journal of Quantitative Spectroscopy & Radiative Transfer, 69(3): 351-388.

Filella, I., Amaro, T., Araus, J.L. and Penuelas, J., 1996. Relationship between photosynthetic radiation-use efficiency of Barley canopies and the photochemical reflectance index (PRI). Physiologia Plantarum, 96(2): 211-216.

Finnigan, J.J., Clement, R., Malhi, Y., Leuning, R. and Cleugh, H.A., 2003. A re-evaluation of long-term flux measurement techniques - Part I: Averaging and coordinate rotation. Boundary-Layer Meteorology, 107(1): 1-48.

Foken, T. and Wichura, B., 1996. Tools for quality assessment of surface-based flux measurements. Agricultural and Forest Meteorology, 78(1-2): 83-105.

Gamon, J.A., Cheng, Y.F., Claudio, H., MacKinney, L. and Sims, D.A., 2006. A mobile tram system for systematic sampling of ecosystem optical properties. Remote Sensing of Environment, 103(3): 246-254.

Gamon, J.A. et al., 1990. Remote-Sensing of the Xanthophyll Cycle and Chlorophyll Fluorescence in Sunflower Leaves and Canopies. Oecologia, 85(1): 1-7.

Gamon, J.A., Penuelas, J. and Field, C.B., 1992. A Narrow-Waveband Spectral Index That Tracks Diurnal Changes in Photosynthetic Efficiency. Remote Sensing of Environment, 41(1): 35-44.

Gamon, J.A., Serrano, L. and Surfus, J.S., 1997. The photochemical reflectance index: an optical indicator of photosynthetic radiation use efficiency across species, functional types, and nutrient levels. Oecologia, 112(4): 492-501.

Gamon, J.A. and Surfus, J.S., 1999. Assessing leaf pigment content and activity with a reflectometer. New Phytologist, 143(1): 105-117.

Garbulsky, M.F. et al., 2010. Patterns and controls of the variability of radiation use efficiency and primary productivity across terrestrial ecosystems. Global Ecology and Biogeography, 19(2): 253-267.

Garrity, S.R., Vierling, L.A. and Bickford, K., 2010. A simple filtered photodiode instrument for continuous measurement of narrowband NDVI and PRI over vegetated canopies. Agricultural and Forest Meteorology, 150(3): 489-496.

Goulden, M.L., Munger, J.W., Fan, S.M., Daube, B.C. and Wofsy, S.C., 1996. Measurements of carbon sequestration by long-term eddy covariance: Methods and a critical evaluation of accuracy. Global Change Biology, 2(3): 169-182.

Hilker, T., Coops, N.C., Wulder, M.A., Black, T.A. and Guy, R.D., 2008. The use of remote sensing in light use efficiency based models of gross primary production: A review of current status and future requirements. Science of the Total Environment, 404(2-3): 411-423.

Hilker, T., Nesic, Z., Coops, N.C. and Lessard, D., 2010. A NEW, AUTOMATED, MULTIANGULAR RADIOMETER INSTRUMENT FOR TOWER-BASED OBSERVATIONS OF CANOPY REFLECTANCE (AMSPEC II). Instrumentation Science & Technology, 38(5): 319-340.

Horton, P., Ruban, A.V. and Walters, R.G., 1996. Regulation of light harvesting in green plants. Annual Review of Plant Physiology and Plant Molecular Biology, 47: 655-684.

Horton, P., Wentworth, M. and Ruban, A., 2005. Control of the light harvesting function of chloroplast membranes: The LHCII-aggregation model for non-photochemical quenching. Febs Letters, 579(20): 4201-4206.

Huete, A. et al., 2002. Overview of the radiometric and biophysical performance of the MODIS vegetation indices. Remote Sensing of Environment, 83(1-2): 195-213.

Huete, A.R., 1988. A soil-adjusted vegetation index (SAVI). Remote Sensing of Environment, 25(3): 295-309.

Inoue, Y., Penuelas, J., Miyata, A. and Mano, M., 2008. Normalized difference spectral indices for estimating photosynthetic efficiency and capacity at a canopy scale derived from hyperspectral and CO2 flux measurements in rice. Remote Sensing of Environment, 112(1): 156-172.

Jordan, C.F., 1969. Derivation of leaf area index from quality of light on the forest floo. Ecology, 50: 663-666.

Kljun, N., Calanca, P., Rotachhi, M.W. and Schmid, H.P., 2004. A simple parameterisation for flux footprint predictions. Boundary-Layer Meteorology, 112(3): 503-523.

Leuning, R., Hughes, D., Daniel, P., Coops, N.C. and Newnham, G., 2006. A multi-angle spectrometer for automatic measurement of plant canopy reflectance spectra. Remote Sensing of Environment, 103(3): 236-245.

Lichtenthaler, H.K., 1987. Chlorophylls and carotenoids: pigments of photosynthetic biomembranes. In: S.P. Colowick and N.O. Kaplan (Editors), Methods in Enzymology. Academic Press, San Diego, pp. 350-382.

Liu, J., Chen, J.M., Cihlar, J. and Park, W.M., 1997. A process-based boreal ecosystem productivity simulator using remote sensing inputs. Remote Sensing of Environment, 62(2): 158-175.

Meroni, M. et al., 2010. Performance of Spectral Fitting Methods for vegetation fluorescence quantification. Remote Sensing of Environment, 114(2): 363-374.

Meroni, M. and Colombo, R., 2006. Leaf level detection of solar induced chlorophyll fluorescence by means of a subnanometer resolution spectroradiometer. Remote Sensing of Environment, 103(4): 438-448.

Meroni, M. et al., 2008. Assessing steady-state fluorescence and PRI from hyperspectral proximal sensing as early indicators of plant stress: The case of ozone exposure. Sensors, 8(3): 1740-1754.

Middleton EM, D.G., Huemmrich KF et al., 2004. Direct satellite inference of ecosystem light use efficiency for carbon exchange using MODIS on Terra and Aqua., Geoscience and Remote Sensing Symposium, IGARSS'04. IEEE International.

Milton, E.J., Schaepman, M.E., Anderson, K., Kneubuhler, M. and Fox, N., 2009. Progress in field spectroscopy. Remote Sensing of Environment, 113: S92-S109.

Moncrieff, J., Valentini, R., Greco, S., Seufert, G. and Ciccioli, P., 1997. Trace gas exchange over terrestrial ecosystems: Methods and perspectives in micrometeorology. Journal of Experimental Botany, 48(310): 1133-1142.

Monteith, J.L., 1972. Solar radiation and productivity in tropical ecosystems. Journal of Applied Ecology, 9: 747-766.

Monteith, J.L., 1977. Climate and efficiency of crop production in Britain. Philosophical Transactions of the Royal Society of London Series B-Biological Sciences, 281: 271-294.

Nakaji, T. et al., 2008. Utility of spectral vegetation indices for estimation of light conversion efficiency in coniferous forests in Japan. Agricultural and Forest Meteorology, 148(5): 776-787.

Penuelas, J., Filella, I. and Gamon, J.A., 1995. Assessment of Photosynthetic Radiation-Use Efficiency with Spectral Reflectance. New Phytologist, 131(3): 291-296.

Penuelas, J., Filella, I., Gamon, J.A. and Field, C., 1997. Assessing photosynthetic radiation-use efficiency of emergent aquatic vegetation from spectral reflectance. Aquatic Botany, 58(3-4): 307-315.

Rahman, A.F., Cordova, V.D., Gamon, J.A., Schmid, H.P. and Sims, D.A., 2004. Potential of MODIS ocean bands for estimating CO/sub 2/ flux from terrestrial vegetation: a novel approach. Geophysical Research Letters, 31(10): 4 pp.

Raich, J.W. et al., 1991. POTENTIAL NET PRIMARY PRODUCTIVITY IN SOUTH-AMERICA - APPLICATION OF A GLOBAL-MODEL. Ecological Applications, 1(4): 399-429.

Rascher, U. et al., 2009. CEFLES2: the remote sensing component to quantify photosynthetic efficiency from the leaf to the region by measuring sun-induced fluorescence in the oxygen absorption bands. Biogeosciences Discussions, 6(1): 2217-2266.

Rossini, M. et al., 2010. High resolution field spectroscopy measurements for estimating gross ecosystem production in a rice field. Agricultural and Forest Meteorology, 150(9): 1283-1296.

Rouse, J.W., Haas, R.H., Schell, J.A., Deering, D.W. and Harlan, J.C., 1974. Monitoring the Vernal Advancements and Retro Gradation of Natural Vegetation, Greenbelt, MD, USA.

Running, S.W. et al., 2004. A continuous satellite-derived measure of global terrestrial primary production. Bioscience, 54(6): 547-560.

Schaepman-Strub, G., Schaepman, M.E., Painter, T.H., Dangel, S. and Martonchik, J.V., 2006. Reflectance quantities in optical remote sensing-definitions and case studies. Remote Sensing of Environment, 103(1): 27-42.

Tucker, C.J. and Sellers, P.J., 1986. Satellite remote sensing of primary production. International Journal of Remote Sensing, 7: 1395–1416.

Wohlfahrt, G., Pilloni, S., Hörtnagl, L. and Hammerle, A., 2010. Estimating carbon dioxide fluxes from temperate mountain grasslands using broad-band vegetation indices. Biogeosciences, 7(2): 683-694.

Zarco-Tejada, P.J., Miller, J.R., Mohammed, G.H. and Noland, T.L., 2000. Chlorophyll fluorescence effects on vegetation apparent reflectance: I. Leaf-level measurements and model simulation. Remote Sensing of Environment, 74(3): 582-595.

Zarco-Tejada, P.J., Miller, J.R., Mohammed, G.H., Noland, T.L. and Sampson, P.H., 2002. Vegetation stress detection through chlorophyll a+b estimation and fluorescence effects on hyperspectral imagery. Journal of Environmental Quality, 31(5): 1433-1441.

# Chapter 3

# Development of Automatic Field Spectrometric Systems

Field spectrometry refers to the use of non-imaging spectrometers near the ground surface and it is usually aimed at evaluating spectral reflectance of the investigated target (Milton et al., 2009). For this purpose, consecutive measurements of total incident sunlight ($E^{TOT}$), and radiance ($L^S$) or irradiance ($E^S$) upwelling from the target are collected by an operator. The incident light is usually evaluated by measuring the radiance upwelling from a white calibrated panel which represents the ideal Lambertian surface. Upwelling fluxes from the investigated surface are usually collected holding the sensor vertically over the surface (*nadir view*) but spectral libraries collected observing the target from different viewing angles are also available (Painter et al., 2003).

FLUXNET network has been established to provide understanding of drivers and processes controlling the carbon and water exchanges between biosphere and atmosphere (Baldocchi, 2008). Such network provides local scale information that are up-scaled using remote sensing (RS) data for mapping the biophysical and biogeochemical processes from regional to global scale (e.g., Running et al., (2004), Sims et al., (2008)). For a better comprehension of the link between photosynthesis and optical signals, a growing number of studies has recently focused on the collection of large datasets of repeated field spectroscopy observations in the sampling area of flux towers (i.e., the footprint) over diurnal cycles or longer time scales (e.g. seasons, years) (Damm et al., 2010; Inoue et al., 2008; Rascher et al., 2009; Rossini et al., 2010). Long-lasting field spectroscopy campaigns based on manual measurements are extremely resource demanding and do not ensure repeatability of the acquisition conditions as the instrument setup is initialized each day. To overcome such limitations few research groups initiated automatic tower-based spectral reflectance measurements (Daumard et al., 2010; Hilker et al., 2007; Hilker et al., 2008a; Leuning et al., 2006; Meroni, 2010; Nakaji et al., 2007; Nakaji et al., 2008) using different devices. With such setups, non-imaging spectrometers are installed in the field on a flux station (or in its proximity), and are operated automatically for long periods (i.e. months to years). This is a valuable approach for a better understanding of the relation between photosynthesis and optical signals because it provides spectral measurements paired with simultaneous carbon flux data. The *SpecNet* (*Spectral Network*) project (Gamon et al., 2006) and the "*Spectral Sampling Tools for Vegetation Biophysical Parameters and Flux Measurements in Europe*" EU COST action (ES0903) have been recently established to promote these activities. In most of the studies, optical *Vegetation Indices* (VIs) are extracted from the measured reflectance spectrums in visible to near infrared region (VNIR, 400-1400 nm) in order to track the development of vegetation. Recent researches have instead focused on the remote estimation of the *Light Use Efficiency* (LUE)(Grace et al., 2007; Hilker et al., 2008b), from "*fine*" (1 nm of *Full Width at Half Maximum*, FWHM) and "*ultra-fine*" (FWHM 0.1 nm) spectral resolution data. LUE represents the conversion efficiency of energy to fixed carbon and it is employed to derive actual photosynthetic rates from potential ones.

The narrow-band spectral index *Photochemical Reflectance Index* (PRI) (Gamon et al., 1992) and the *sun-induced chlorophyll Fluorescence* (F), (Plascyk, 1975; Plascyk and Gabriel, 1975) have been showing some potential for the estimation of LUE. Estimating F with hyperspectral observations is a recent application (for a review see Meroni et al., 2009) that requires a spectral resolution as fine as 0.1 nm FWHM to investigate narrow absorption lines present in the incident irradiance spectrum. Such resolution can be achieved by commercial spectrometers at the expenses of the extension of the spectral interval being investigated. In fact, a typical CMOS (Complementary Metal Oxide Semiconductor), CCD (Charge Coupled Devices) or photodiode array spectrometer can cover the entire VNIR range with a 1-3 nm resolution that is adequate for the computation of all VIs including the PRI. Conversely, when the required resolution is 0.1 nm or lesser (as required for F estimation Meroni and Colombo, 2006; Meroni et al., 2008), the digitized spectral range is restricted to a hundred nanometers. This technical constrain imposes the simultaneous use of two spectrometers with different spectral resolution and range if the computation of VIs and F is required.

This chapter presents the development of two fully automated spectral systems capable of collecting unattended, continuous, long-term spectral measurements. Optical instruments routinely collect "*fine*" and "*ultra-fine*" spectrums of incident irradiance ($E^{TOT}$) and upwelling irradiance($E^{S}$)-radiance($L^{S}$) by using *High Resolution Spectrometers HR4000* (OceanOptics, US).

The *HyperSpectral Irradiometer* (HSI) is a custom designed system employing a rotating arm to observe alternately the sky and the target surface. The *Multiplexer Radiometer Irradiometer* (MRI) instead is entirely composed of commercial optical-electronic components and it uses an optical multiplexer (MPM-2000, OceanOptics, US) that switches the input of the detectors between a channel measuring the incident irradiance (through a fiber connected to an up-looking cosine-response optic) and a channel measuring the radiance upwelling from the surface through a down-looking bare fiber.

The development of such systems includes the optical design, the development of the data acquisition and processing software as well as the definition of the calibration procedures.

# 3.1 The HyperSpectral Irradiometer – HSI

The *HyperSpectral Irradiometer* (HSI) is a fully automated spectral system capable of collecting unattended, continuous, long-term spectral measurements of Earth surface under solar light illumination. It's a custom designed instrument developed in collaboration with the Italian National Research Council (IFAC-CNR, Florence). HSI employs a rotating arm to observe alternately the sky and the target surface. A cosine-response optic consisting of planar holographic diffuser is used to measure the solar incident irradiance ($E^{TOT}$) and the irradiance upwelling from the surface ($E^{S}$), allowing the computation of the BHR (Bi-Hemispherical Reflectance factor) (Shapman-Strub et al, 2006).

The system is able to simultaneously collect "fine" and "ultra-fine" spectrums, in particular the instrument employs two spectrometers sharing the same optical signal, one covering the VNIR range 400-1000 nm (SPEC1) with a FWHM of 1 nm, and the other providing higher spectral resolution (0.1 nm FWHM) within a narrower spectral interval (700-800 nm) in the NIR (SPEC2). The VNIR data collected by the first spectrometer allow the computation of the reflectance spectrum and the associated *Vegetation Indices* (VIs), while higher spectral resolution NIR data from the second instrument permit the estimation of *Sun-Induced Fluorescence* in the oxygen absorption band $O_2$-A located around 760 nm (F@760).

*Table 3.1: Technical features of the Ocean Optics High Resolution Spectrometers HR4000 embedded into HSI. Full Width at Half Maximum (FWHM) and Sampling Interval represent the spectral resolution of the spectrometers. The first spectrometer works in the VNIR spectral range, the high resolution spectrometer instead works in a smaller range (700 nm - 800 nm).*

| *Spec.* | *FWHM* | *Sampling Interval* | *Spectral Range* | *Application* |
|---|---|---|---|---|
| **1** | 1 | 0.25 | 400-1000 | Irrad. measurements, ρ computation |
| **2** | 0.1 | 0.02 | 700-800 | Fluorescence at $O_2$-A (F@760) |

Figure 3.1 shows the 3D rendering of HSI optoelectronic system. A cosine-response foreoptic (Figure 3.1, a) consisting of a planar holographic diffuser, protected by an external BK7 window, is used to collect the

incident light. The cosine response entrance was selected because it represents an optimal compromise for measuring standard irradiance values when operating in zenith view, and matching the wide eddy flux footprint when operating in nadiral viewing geometry. The system is able to observe both the downwelling spectral irradiance and the ground emerging irradiance from a height of a few meters.

The choice of polycarbonate holographic diffuser helped us to maintain a high optical throughput of the light collecting element. The diffuser foreoptic feeds the two spectrometers through a ray path bounded by two black aluminum cylinders connected by a 45° folding mirror, as shown in Figure 3.1, b.

*Figure 3.1: 3D rendering of HSI optical design. (a) Entrance cosine-response foreoptic; (b) 45° inclined folding mirror; (c) aspheric achromatic multiplets; (d) mechanical shutter; (e) beam splitter plate; (f) VNIR spectrometer; (g) NIR spectrometer; (h) step motors.*

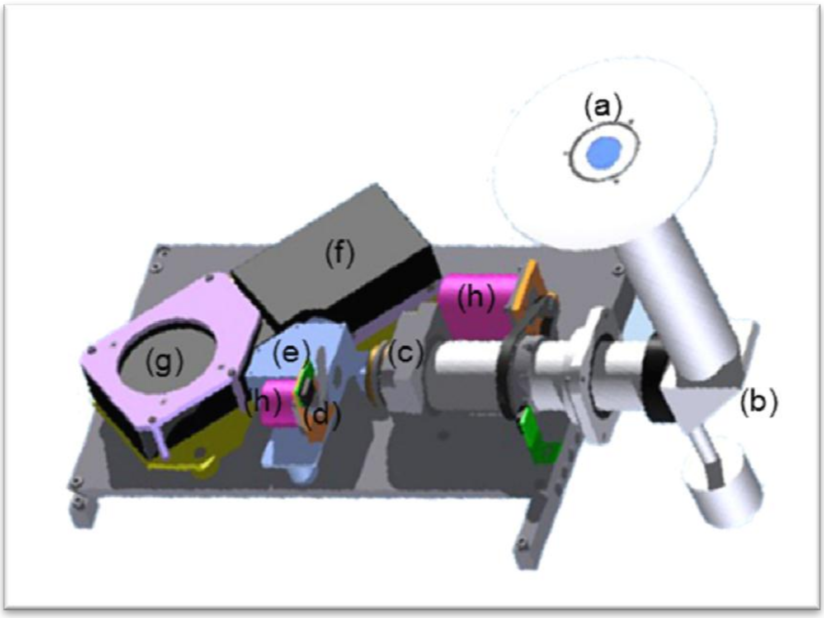

After the folding mirror (Figure 3.1, b), the light is focused by a pair of aspheric achromats (element (c) in Figure 3.1) near the input port of the spectrometers, where two additional doublets, one for each spectrometer, increase the signal level by reducing the effective focal length of the instrument. A BK7 dichroic Beam Splitter (BS) plate (Figure 3.1, e), placed before the two final doublets, performs amplitude division of the incoming beam with an output intensity ratio of 30R/70T (30% reflected, 70% transmitted). The greater portion of the input photon flux is transmitted to the NIR spectrometer (the element (g) in Figure 3.1) that, due to its higher resolving power and to the lower level of available irradiance, requires longer integration times than the VNIR spectrometer (Figure 3.1, element (f)). This last spectrometer, which exploits a broader spectral interval, is fed by the BS reflected ray-path, hence avoiding the spectrally variable lateral displacement of the beam affecting the transmitted ray-path. This phenomenon, connected to the spectral dispersion of the BS material, is almost negligible over the narrow spectral range (less than 100 nm) observed by the NIR spectrometer, also because of the reduced slope of the BK7 refraction index around 750 nm. An electro-actuated mechanical shutter shown in Figure 3.1 as the element (d) can stop the light traveling the instrument, allowing the user to gauge the dark signal of the spectrometers. Optical and electronic components are hosted in a waterproof and thermally insulated box (50x40x19 cm, 25 kg weight) (Figure 3.2).

A dedicated cooling system was developed to control thermal conditions of the instrument to avoid radiometric and spectral troubles to the optical components. An air-conditioner (EVE0300220, Stulz SpA) provides 164 $m^3$/h of fresh air that is pushed into the instrument along a dedicated pipeline, at the same time hot and wet air is pumped out by a second pipeline connected to the input of the air-conditioner. The resulting duty-cycle has different advantages: i) to minimize the condensation of water over optical components (eg. mirrors, diffusers etc…); ii) to minimize the thermal drift of the optical components; iii) to avoid the entrance of dust and a progressive deterioration of the optical performances. Slim and low power consumption thermoelectric resistances are placed close to the optical equipment subjected to condensation of water vapor. HSI is expected to work in field for long time periods under varying environmental conditions (temperature, air humidity, rain etc…).

*Figure 3.2: (A) picture of the HSI box, the overlay is the mechanical design of the instrument; (B) picture of the HSI installed in field.*

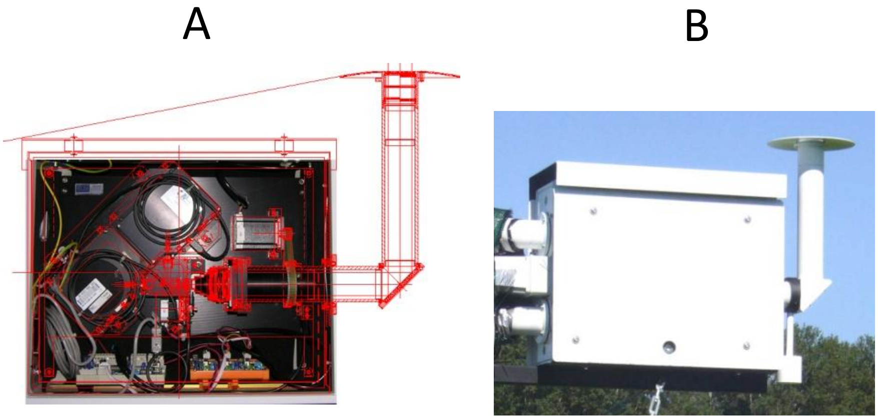

Spectrometers, stepped motors and the other electronic equipment are controlled by an Industrial Personal Computer (VS-Flexrunner 863A/CV). The communication with the two spectrometers is based on the Universal Serial Bus v2.0 protocol. Electronic control boards of HSI are instead managed using a RS232 communication protocol. Spectral data measured by the instrument are stored on the PC.

During operations, HSI employs the rotating arm to observe alternately the sky and the target surface (Figure 3.3 (a) and (b), respectively). The arm rotation, as well as the mechanical shutter for dark current measurement, is actuated by stepper motors (Figure 3.1, h) controlled by a computer through an electronic board (PCE computer systems, Italy).

The measurement of incident solar irradiance ($E^{TOT}$) and upwelling irradiance emerging from the surface ($E^{S}$), allows the computation of the *Bi-Hemispherical Reflectance factor* (BHR, also known as albedo), the ratio of the radiant flux reflected from a unit surface area into the whole hemisphere to the incident radiant flux of hemispherical angular extent (equation 3.1).

$$BHR = \frac{1}{\pi}\int_0^{2\pi}\int_0^{\pi/2} r\left(\theta_i,\varphi_i,2\pi\right)\cdot\cos\theta_i\cdot\sin\theta_i\;d\theta_i\;d\varphi_i$$

*Equation 3.1*

*Figure 3.3: HSI in position zenith (a) and nadir (b) view, measuring the incident and upwelling irradiance, respectively.*

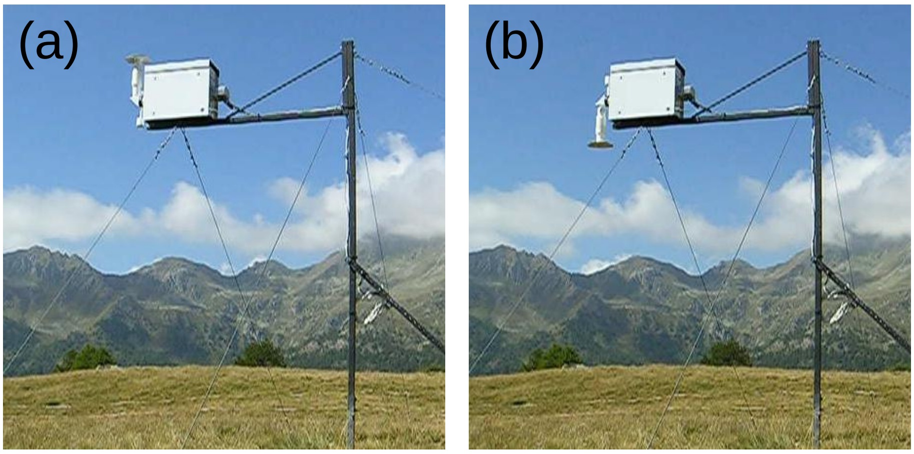

The measured irradiance *E* can be expressed integrating the impinging radiance *L* over all the propagation directions *(ϑ, φ)*, as shown in the following equation:

$$E(\lambda)=\int_0^{2\pi}\int_0^{\pi/2} L(\lambda,\theta,\varphi)\cdot\cos\theta_i\cdot\sin\theta_i\, d\theta_i\, d\varphi_i \qquad \textit{Equation 3.2}$$

Where $\lambda$ is the wavelength and [0, $2\pi$] and [0, $\pi/2$] define the integration intervals with respect to azimuth ($\phi$) and zenith ($\theta$) angles, respectively. Using equation 3.2 and assuming that the observed surface is homogeneous and Lambertian (i.e., *L* is independent of ($\theta$,$\phi$)), it is possible to model the contribution to the total measured irradiance of the signal coming from a cone defined by a given zenith angle $\theta$ and all azimuthal directions (Figure 3.4). Figure 3.4 shows that 97% of the total signal comes from a cone limited by a zenith angle of 80° and also that the maximum contribution to the measured signal comes from zenith angles around 45°.

Note that when the HSI is measuring $E^S$ (i.e., it's in nadir view position), the zenith angle $\theta$ defines a circular area on the ground with a radius h*tan$\theta$, where h is the height above ground of the instrument.

*Figure 3.4: Dashed line: fraction of the signal coming from the cone defined by the angular interval [0,* $\theta$*]. Full dots: fractional contribution of the signal arriving from zenithal angular sectors (*$\theta \pm 5°$*). The upper x-axis reports the radius of the area contributing to the signal as a function of* $\theta$ *and for an instrument height of 3.5 m.*

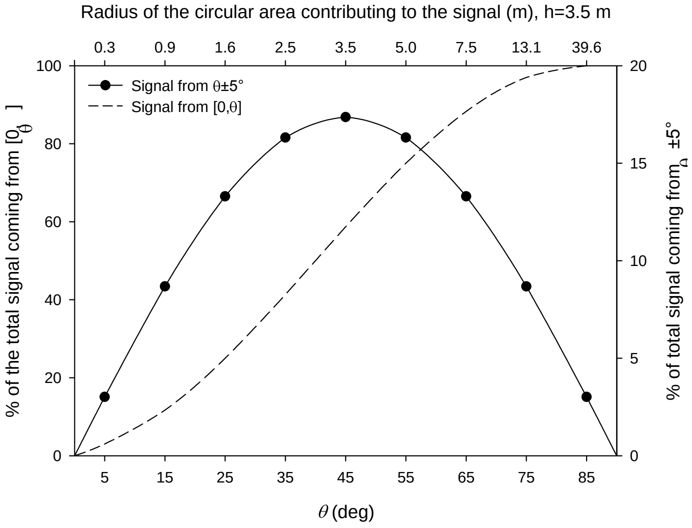

HSI is usually installed in field using the small metal tower showed in Figure 3.3, the structure allows to keep the instrument at an heght of 3.5 m above the investigated surface in nadir position. Using this configuration for a typical instrument installation, the 97% footprint of HSI is represented by a circular ground area with a radius of about 20 m as shown in Figure 3.4.

A dedicated power supply system has been developed: it consists of 9 photovoltaic panels, 6 storage batteries and a tension reducer in order to feed all the devices.

As an example typical spectral data collected by HSI during a single acquisition session over a vegetated surface are depicted in Figure 3.5. Spectrums of the sun light irradiance ($E^{TOT}$) and the upwelling irradiance are depicted ($E^{S}$). "*Fine*" (dark-lines) spectrums collected by the SPEC1 covers the VNIR range, "*ultra-fine*" spectrums measured by the SPEC2 covers the 700-800 nm range (light-lines). Blue lines are the total solar incident irradiance ($E^{TOT}$), red lines are the irradiance upwelling from the target surface ($E^{S}$) and green lines are the computed BHR.

*Figure 3.5: Example of a single spectral data acquisition over a vegetated surface. Downwelling and upwelling irradiances ($E^{TOT}$ and $E^{S}$) and the resulting BHRs for the VNIR and NIR spectrometers. The reflectance peak at 760 nm is visible in the NIR spectrometer data and it is originated by the fluorescence infilling of the $O_2$-A band.*

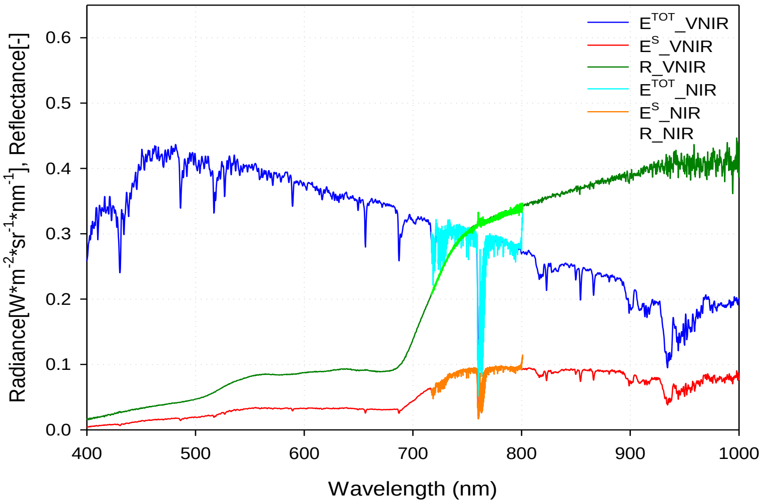

The optical setup of HSI was modified in 2010 removing the2$^{nd}$ holographic diffuser of the cosine receptor. This results in a greater optical throughput of the instrument, allowing to reduce the time needed to collect a session of spectral measurements. We are aware that the removal of a diffuser causes a worsening of the cosine response of the foreoptic, however we think that the improvements derived by the reduction of the acquisition time compensate the worsening of the cosine response.

# 3.2 The Multiplexer Radiometer Irradiometer – MRI

The *Multiplexer Radiometer Irradiometer* (MRI) is a fully automated spectral system developed assembling commercial optoelectronic components. This instrument is capable of collecting unattended, continuous, long-term passive spectral measurements of Earth surface in the optical domain. MRI simultaneously collects "*fine*" (FWHM of 1 nm) and "*ultra-fine*" (0.1 nm FWHM) spectrums employing two spectrometers: the former covering the VNIR range 400-1000 nm (SPEC1) with a 1 nm spectral resolution, and the latter providing an higher spectral resolution within a narrower spectral interval (700-800 nm) in the NIR (SPEC2). The VNIR data collected by the first spectrometer allow the computation of the reflectance spectrum and the associated vegetation indices (VIs), while higher spectral resolution NIR data from the second device permit the estimation of *sun-induced chlorophyll Fluorescence* in the oxygen absorption band $O_2$-A located around 760 nm (F@760).

The core of the MRI is a commercial *optical multiplexer* (MPM-2000, Ocean Optics, US) that switches the input of the spectrometers between different optical channels (optical fibers), allowing to alternatively measure sun irradiance (downwelling) and radiance coming from the Earth surface (upwelling). The uplooking channel is equipped with a cosine corrector oriented towards the Zenith and it's used to measure total downwelling sun irradiance ($E^{TOT}$). The entrance foreoptic is a CC-3 (Ocean Optics, Dunedin, USA), characterized by an opaline glass diffusing to collect radiation (light) at 180°. The optical channel oriented toward nadir has a Field of View (FOV) of 25° that allows the measurement of the radiance coming from the surface. Optical fibers used for both measurement channels are 5 m long Ocean Optics VNIR 600 µm diameter optical fibers. Spectrometer dark current is measured by switching the input of the multiplexer to a blind channel. Optical fibers are connected to the optical multiplexer which transfers the light to the spectrometers thought two 50 cm long VNIR 600 µm optical fibers. The spectrometers employed are Ocean Optics (HR4000 High Resolution Spectrometer, Ocean Optics, Inc.). Detailed technical features are reported in Table 3.2. The technical scheme of the instrument optical layout is shown in Figure 3.6.

*Table 3.2: Technical features of the Ocean Optics High Resolution Spectrometers HR4000 embedded in MRI. Full Width at Half Maximum (FWHM) and the Sampling Interval represent the spectral resolution of the instrument. The first spectrometer works in the VNIR spectral range, the high resolution spectrometer instead works in a small range (700 nm - 800 nm).*

| *Spec.* | *FWHM* | *Sampling Interval* | *Spectral Range* | *Application* |
|---|---|---|---|---|
| **1** | 1 | 0.25 | 400-1000 | Irrad. measurements, ρ computation |
| **2** | 0.1 | 0.02 | 700-800 | Fluorescence at $O_2$-A (F@760) |

Typical integration time values for mid latitude summer illumination conditions at midday are 200 msec for the SPEC1 and 1 sec for the SPEC2.

*Figure 3.6: Technical scheme of the Multiplexer Radiometer Irradiometer (MRI). The uplooking foreoptic (cosine receptor) collects the incident sunlight, sampling of the radiance from the Earth's surface is made by the down looking optical channel (bare fiber). Optical multiplexer, spectrometers and the personal computer are hosted in a protective box.*

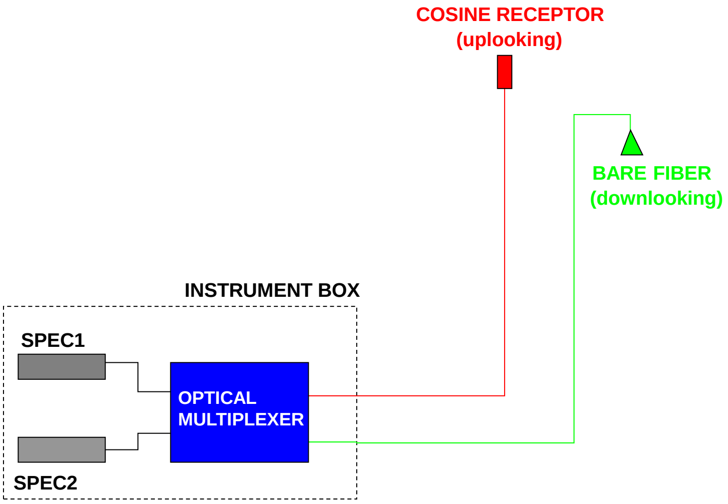

The optical multiplexer operations and the acquisitions of spectral measurements are controlled by a netbook personal computer (EeePc, ASUS, Inc) connected to these elements. The multiplexer is controlled via a RS232 cable while the spectrometers are interfaced through a USB 2.0 connection.

The main optical components (multiplexer, spectrometers), netbook and power supply are hosted in a protective box that enables input/output of all optical channels and electrical supply cable, but at the same time is resistant to weather. Air temperature inside the box is controlled by a cooling system that allows to regulate the temperature of the optical and electronic components. The field installation of MRI typically requires a tripod for sampling low height canopy (Figure 3.7) or a tower-based setup over tall vegetation like forest trees.

*Figure 3.7: Typical setup of MRI installation in field: the tripod supports the ends of the optical channels. The red circle evidences the cosine corrector receptor, the green one indicates the end of the down-looking channels (bare fibers).*

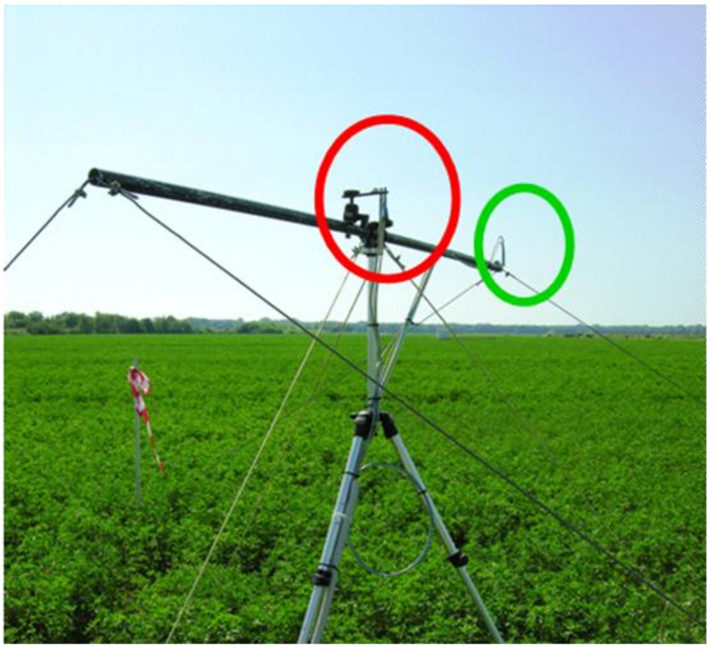

Using the optical layout described, MRI allows the measurement of the *Hemispherical-Conical Reflectance Factor* (HCRF) (Shapman-Strub et al., 2006):

$$HCRF = R(\theta_i, \varphi_i, 2\pi, \theta_r, \varphi_r, \omega_r \ =$$

$$= \frac{\int_{\omega_r}\int_{2\pi} f(\theta_i,\varphi_i,\theta_r,\varphi_r)\, L_i(\theta_i,\varphi_i) d\Omega_i d\Omega_r}{(d\Omega_r/\pi)\int_{2\pi} L_i(\theta_i,\varphi_i) d\Omega_i} \qquad \textit{Equation 3.3}$$

were $\vartheta_i$ is the solar zenith angle, $\varphi_i$ the solar azimuth angle, $\vartheta_r$ is the zenith angle of the reflection direction, $\varphi_r$ the azimuth angle of the reflection direction, ω the solid angle and Ω the projected solid angle.

As an example, typical spectral data collected by MRI during a single acquisition session over a vegetated surface are depicted in Figure 3.8. In the upper panel the spectrums of the incident and upwelling radiances ($E^{TOT}/\pi$ and $L^S$) are depicted. “*Fine*” spectrums (dark-lines) collected by the SPEC1 cover the VNIR range, “*ultra-fine*” spectrums (light-lines) measured by the SPEC2 covers the 700-800 nm range. Blue lines are the total solar incident radiance ($E^{TOT}/\pi$), red lines are the radiance upwelling from the target surface ($L^S$) and green lines are the resulting HCRF.

*Figure 3.8: Example of a single spectral data acquisition session over a vegetated surface. Downwelling and upwelling radiances (upper panel) and resulting HCRF (lower panel) for Spec1 covering the full VNIR range and for Spec2, covering the restricted range 700-800 nm with higher resolution.*

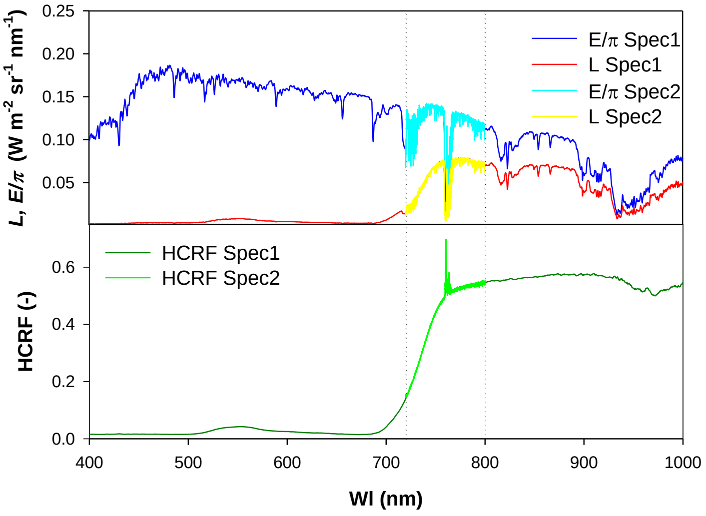

# 3.3 Comparison between HSI and MRI instruments

Summary remarks concerning the technical differences of the HSI and MRI systems are discussed in this section. Relevant characteristics that distinguish the two instruments are listed in Table 3.3.

As mentioned in the last sections both the systems observe the sky with a cosine-receptor foreoptic (measuring downwelling irradiance, $E^{TOT}$), but they detect the light flux emerging from the investigated surface using different foreoptics. HSI employs a rotating arm that allows to observe alternately the sky and the target with the same foreoptic (single optical channel). MRI is designed with two different optical channels which are alternatively selected by the optical Multiplexer. The uplooking channel is equipped with a cosine corrector oriented towards the Zenith and it’s used to measure total downwelling sun irradiance ($E^{TOT}$), while the optical channel oriented toward nadir has a FOV of 25° that allows the measurement of the radiance coming from the surface ($L^{S}$). Consequently instruments measure different reflectance quantities, the BHR and the HCRF are estimated respectively by HSI and MRI. BHR is suitable because enables to sampling a wider area, but BRDF effects of vegetation are more pronounced.

*Table 3.3: Summary table of technical characteristics that distinguish HSI and MRI systems.*

| Characteristic | HSI | MRI |
|---|---|---|
| **Uplooking FOV** | hemispherical | hemispherical |
| **Downlooking FOV** | hemispherical | conical (25°) |
| **Reflectance** | BHR | HCRF |
| **Moving parts** | yes (instrument FOV) | no |
| **Optical channel** | single | double |
| **Field installation and maintenance** | more difficult | easy |

On the other hand, despite the area sampled by MRI is smaller, the signal recorded ($L^S$) results less affected by BRDF effects. Furthermore upscaling studies to airborne or satellite remote sensing platform appear to be facilitated using $L^S$.

Optical design of HSI is preferred because the downwelling and upwelling light fluxes are measured with the same optical channel so the resulting reflectance values are less dependent on instrument calibration, while accurate calibration of both (up/down looking) channels of MRI is needed to quantify the reflectance factor. Moreover the calibration of a double channel instrument requires additional efforts, because calibration procedures must be applied to each measurement optical path.

Following the field experience conducted, the installation/maintenance of MRI is resulted easier and more flexible to be adapted at different canopies. This is mainly related to the fact that the box containing the optical and electronic components (heavy part) can be place at ground, whereas only the instrument entrance foreoptics (light part) are placed above the canopy exploiting the 5 m long optical fibers.

# 3.4 System Calibration

The accurate spectral and radiometric characterization and calibration of high-resolution spectrometers is required for correctly computing, interpreting, and comparing radiance and reflectance spectrums acquired at different times or by different instruments. For example, in the field of vegetation monitoring many recent applications rely on the analysis of very narrow absorption features related to the characteristics of both plants and the atmosphere. This makes precise characterization of the instrument response fundamental for the development and validation of data-processing algorithms (Guanter et al., 2009).

The use of narrow-band spectral vegetation indices has, in fact, proliferated in vegetation studies to detect leaf biochemical composition or physiological status (Gamon et al., 1992; Meroni et al., 2009). Today, the intercomparison of spectral data collected on the ground with different spectrometers is also needed in the framework of the established *SpecNet* (Spectral Network) project (Gamon et al. 2006) and of recent activities related to European Cooperation in Science and Technology” (EU COST) Action ES0903. Complete characterization is also important for the processing of spectral data with radiative transfer (RT) physically based models and in particular for the inversion of reflectance models simulating RT in the vegetation (e.g. Jacquemoud et al., 2009).

The *calibration* term is often used as an abbreviation of the complex problem of *characterizing* and *calibrating* the performance of an instrument. The *characterization* process is the assessment of the instrument’s behaviour with respect to the arriving photons while *calibration* process takes such behaviour into account and establishes traceability of the characterized instrument to a predefined standard. Accurate *characterization* and *calibration* of spectrometers is required for correctly computing, interpreting, and comparing radiance and reflectance spectrums acquired at different times or by different instruments.

*Calibration* of optical devices is an instrument-specific task that includes spectral and radiometric calibration. Spectral calibration consists in the determination of the spectral performances of instrument, important parameters are: the *Full-Width-at-Half-Maximum* (FWHM) (i.e. spectral resolution), *Center Wavelength* value of each spectral band. The radiometric calibration consists instead in the conversion of the digital counts (raw signal) measured by a spectrometer in physical units (e.g. $W\ m^{-2} sr^{-1}\ nm^{-1}$ ) for each wavelength.

Optical sensor calibration is usually performed in laboratory and ideally at regular time, in order to account sensor aging and degradation. A regular calibration is particularly relevant in this research aimed at the recording of continuous and long-term hyperspectral measurements. In fact, systems operated at the flux-towers are continuously exposed to varying environmental factors (e.g. temperature, rain, humidity etc.) which affect instrument performances. The developed automatic field spectrometric systems are, actually, one-off products with very specific calibration requirements, for this reason a dedicated calibration process is required in order to consider the different optical layouts.

The calibration process developed for the *calibration* of HSI and MRI entails two phases: a detailed "*laboratory calibration*" carried out yearly before installing the instrument in the field and an "*in-situ calibration*" performed regularly during field measurement.

## 3.4.1 Laboratory Calibration

Laboratory calibration of a sensor is a complex task that involves the use of highly specific instruments and the access to traceable radiometric standards. Standard calibration procedures available for commercial spectrometers must be adapted to the specific features of each system. For example, the hemispherical field of view of both instruments (i.e. HSI and MRI) requires the use of special equipment to carry out the radiometric calibration such as large Integrating Spheres traceable to International Standard. This equipment is expensive and available only in research centres of international importance such as Goddard Space Flight Center (GSFC[1]), Calibration Home Base (CHB[2]) at the DLR (Oberpfaffenhofen,

---

[1] Website: http://spectral.gsfc.nasa.gov

[2] Website: http://www.dlr.de/caf/en/desktopdefault.aspx/tabid-5378/9173_read-16387/

Germany) and the United Kingdom Network (NCAVEO[3]). Unfortunately, for this reason, a laboratory absolute radiometric calibration of the developed automatic systems has not yet been performed. However, radiometric calibration of automatic systems is accomplished by cross-calibration measurements collected in field, simultaneously, using a well-calibrated (i.e. laboratory calibrated) reference system. Details of the methodology adopted for radiometric calibration are reported in chapter 3.4.2.2.

Spectral calibration was instead achieved in laboratory applying an improved version of the standard methodology provided by the spectrometer manufacturer (OceanOptics, US). The aim of the procedure is the estimation of the *Full Width at Half Maximum* (FWHM) and the *Center Wavelength* value of each spectrometer spectral band (Figure 3.9).

*Figure 3.9: Diagram of the principal spectral features of field spectrometers. Points represent the spectral bands, FWHM (i.e. spectral resolution) and center wavelength of a response function.*

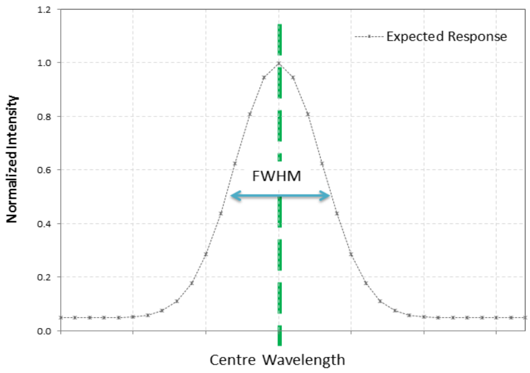

Spectral calibration relies on the use of particular light sources, typically mercury (Hg), argon (Ar) lamps, able to produce very narrow emission lines across the VNIR spectral range. In the present research an argon-mercury light calibration source (CAL-2000 Mercury Argon Lamp, Ocean Optics, US) providing several nearly monochromatic spectral lines in the range 250-920 nm was used. Emission lines produced by the calibration light source are considered infinitesimally narrow (in terms of bandwidth) with respect to the FWHM of both the spectrometers. Measurements of emission line provided from the calibration are collected with both "*fine*" and "*ultra-fine*"

---

[3] Website: http://www.ncaveo.ac.uk

resolution spectrometers embedded in HSI and MRI. As an example, a spectrum recorded with the "*ultra-fine*" spectrometer is reported in Figure 3.10 A. A gaussian function is fitted to each emission line available in the spectral region covered by the spectrometer to determinate the FWHM and center wavelength (Figure 3.10 B).

*Figure 3.10: Example of: A) Spectrum of CAL-2000 (Ocean Optics, USA) calibration light source measured by "ultra-fine" spectrometer. B) Normalized spectral response at the 750 nm argon line with 3 parameters Gaussian fit.*

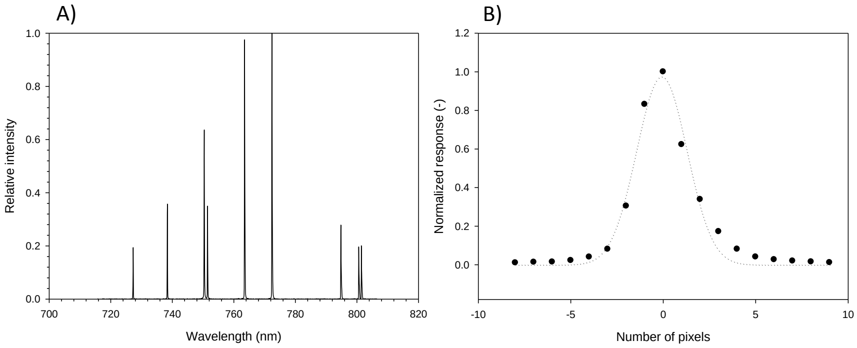

Once determined the parameters of the gaussian function, FWHM is calculated with Equation 3.4.

$$FWHM = 2\sqrt{2\ln 2}\ \sigma \qquad \textit{Equation 3.4}$$

where σ is the standard deviation of the Gaussian function. An example of the results obtained with the "*ultra-fine*" spectrometer is reported in Table 3.4.

*Table 3.4: Example of the results obtained by spectral calibration of the "ultra-fine" resolution spectrometer. Lines are the nominal (i.e. tabulated) wavelengths of the emission lines (CAL-2000, OceanOptics, US) considered; pixel # is the pixel number of the peak maximum; FWHM represents the spectral resolution.*

| Line (nm) | Pixel # | FWHM (nm) |
|---|---|---|
| **727.2936** | 366.3 | 0.220908 |
| **738.3981** | 754.2 | 0.166577 |
| **750.3869** | 1194.4 | 0.137017 |
| **763.5106** | 1705.0 | 0.117745 |
| **794.8176** | 3087.9 | 0.166660 |

FWHM is slightly different across the spectral range, minimum values are typically observed at the centre of the spectral range covered by the instrument. However the average value is considered.

Center wavelength array is determined comparing the center value measured by the spectrometer (expressed as pixel #) with the nominal wavelength value (i.e. tabulated) for each emission line. Comparison is done by non-linear regression technique. A third-degree polynomial is used in order to estimate the spectral calibration coefficients (I and $C_k$). The intercept (I) is the first wavelength of the spectrometer (the lower spectral range of the spectrometer). Equation 3.5 relates the pixel # and the true wavelength values ($\lambda_i$). It is evaluated to calculate the calibrated wavelength values for each spectral pixel (i) of the spectrometer.

$$\lambda_i = I + \sum_{k=1}^{3} C_k p_i^k$$

*Equation 3.5*

## 3.4.2 In situ Calibration

Characterization and calibration are usually performed in the laboratory by means of time and resource consuming calibration procedures and, therefore, they are not always performed with the necessary frequency during the instrument’s life. Unfortunately the accuracy of laboratory calibration deteriorates or becomes obsolete during instrument operations, due to the modification of the physical characteristics of the instrument caused by the natural deterioration of the optoelectronic components. Instrument response may drift slightly because of the aging of the optical and electronic components, misalignment due to mechanical shock/vibration, and effects caused by environmental conditions (Guanter et al., 2006).

Accurate characterization/calibration of spectrometric systems in the time is required in order to continuously deliver high quality spectral data and associated uncertainties. In situ calibration methodologies of HSI and MRI are developed in order to reach these purposes.

# 3.4.2.1 Spectral calibration

Spectral calibration may drift slightly and instrument FWHM may also change due to the aging of the optical and electronic components, misalignment due to mechanical shock, and variations in environmental conditions. Wavelength drift originates the so-called *Spectral Shift* (SS), defined for a given channel as the difference of the nominal center wavelength and the actual one.

Several approaches have been proposed to detect SS (Gao et al., 2004; Green et al., 2003; Guanter et al., 2007; Guanter et al., 2006) and to characterize the FWHM (Green et al., 2003; Guanter et al., 2009) from the data measured during sensor operation, avoiding ad hoc laboratory calibration. All these methods are based on the comparison between measured and modeled at-sensor solar radiance spectra. The spectral characteristics of the instrument are estimated by comparing specific atmospheric absorption features present in both the measured and the simulated spectra. The exploited features are usually related to atmospheric absorption features because these studies are intended for calibration of spectrometers with typical resolutions ranging from 2 to 10 nm. This limits the choice of absorption features to rather broad ones, such as those related to water vapor or molecular oxygen, which are highly influenced by the optical properties of the atmosphere.

A spectrum matching method named "*SpecCal*" was developed (Meroni et al., 2010) to determine both the SS and FWHM of "*fine"* and "*ultra-fine"* spectral resolution spectrometers by means of ground measurements of incident solar irradiance regularly performed during man-assisted or automated field spectrometric operations to calculate the reflectance of the investigated surface. Besides the use of atmospheric absorption features, the fine resolution of the spectrometers considered allows the exploitation of several narrow solar *Fraunhofer* lines, which are dark lines in the spectrum caused by absorption of various chemical elements in the upper layer of the Sun's atmosphere. Given the extraterrestrial origin of such lines, they are less variable than the terrestrial atmospheric absorption features and, thus, make the accuracy of the method less dependent on the accurate parameterization of the atmospheric model simulation.

Evaluation of the spectral parameters of a spectrometer is achieved by comparing the measured spectrum of incident irradiance, $E^{TOT}_{meas}(\lambda)$, with that modeled using the MODTRAN4 radiative transfer code (reference irradiance) (Berk et al., 1998), $E^{TOT}_{mod}(\lambda)$, in selected spectral windows characterized by the presence of one or more strong absorption features, where the measurements are most sensitive to instrument calibration. The spectral windows selected for calibration are well distributed over the VNIR range (Figure 3.11), allowing a window-wise evaluation of both SS and FWHM at several wavelengths along the spectrum.

*Figure 3.11: Distribution of selected absorption features over the incident irradiance spectrum (black curve). Solid vertical lines refer to solar Fraunhofer lines, dashed vertical lines refer to molecular oxygen absorption features, and gray areas are the spectral regions affected by water vapor absorption.*

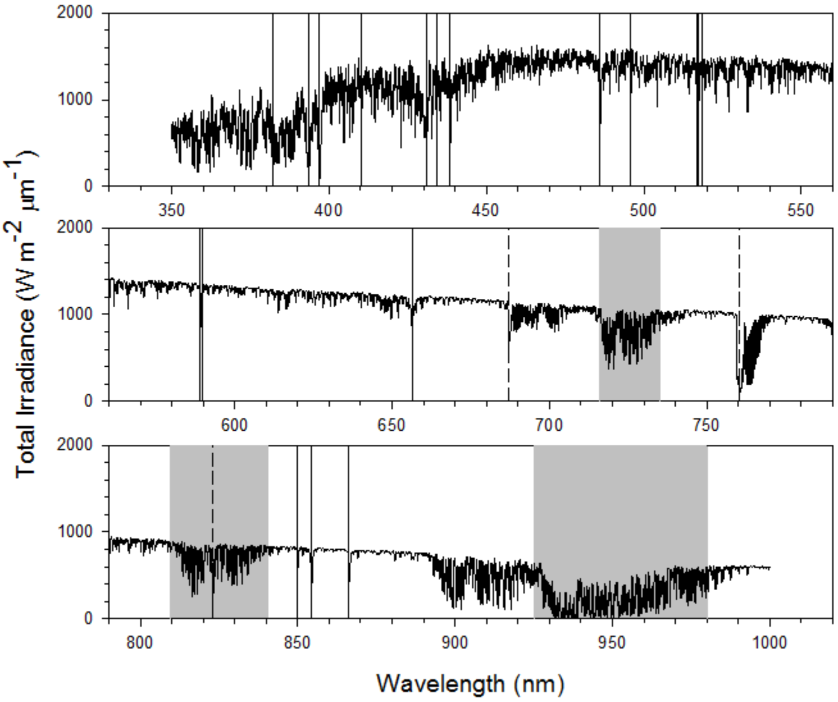

Both absorption features present in the Earth atmosphere and *Fraunhofer* lines present in the exo-atmospheric irradiance have been selected on the basis of their width and depth (Table 3.5). In order to make the method less dependent on sky conditions, absorption features considered for the calibration are preferentially solar *Fraunhofer* lines.

The retrieval of spectrometer parameters is performed by simultaneously resampling the MODTRAN4 reference irradiance spectrum to different FWHMs and imposing a variable SS until the best match with the measured irradiance is found. The retrieval is conducted at each spectral window separately. The FWHM and the SS that give the best match between the MODTRAN4 reference irradiance and the measured irradiance are expected to correspond to the actual parameters of the spectrometer.

*Table 3.5: Fraunhofer lines and atmospheric absorption features exploited: window progressive number, element/elements causing the feature/features, origin (solar or terrestrial), wavelengths of irradiance minimum (numbers in bold italic refer to the shortest and longest wavelength of the range interested by absorption), width of the features (FWHM), and spectral range of the window considered in the optimization procedure.*

| **Window** | **Element** | **Origin (Solar/Terrestrial)** | **Wavelength (nm)** | | | **Width (nm)** | | | **Window range (nm)** | |
|---|---|---|---|---|---|---|---|---|---|---|
| 1 | Fe, Ca+ | *S* | 382.05 | 393.37 | 396.84 | 0.24 | 1.46 | 1.35 | 382 | 397 |
| 2 | Hδ | *S* | 410.16 | | | 0.28 | | | 410 | 410.3 |
| 3 | Fe and Ca, Hγ, Fe | *S* | 430.8 | 434.06 | 438.34 | 0.98 | 0.51 | 0.30 | 430 | 438 |
| 4 | Hβ, Fe | *S* | 486.13 | 495.75 | | 0.29 | 0.16 | | 486 | 496 |
| 5 | Mg, Fe | *S* | 516.73 | 517.27 | 518.37 | 0.36 | 0.24 | 0.24 | 516 | 518 |
| 6 | Na | *S* | 589.01 | 589.6 | | 0.20 | 0.19 | | 589 | 590 |
| 7 | Hα | *S* | 656.29 | | | 0.33 | | | 656.1 | 656.5 |
| 8 | $O_2$ (-B) | *T* | 686.85 | | | 1.54 | | | 686 | 688 |
| 9 | Water vapor | *T* | ***716*** | ***735*** | | contiguous features ~0.5 nm | | | 716 | 735 |
| 10 | $O_2$ (-A) | *T* | 760.41 | | | 2.80 | | | 759 | 770 |
| 11 | $O_2$ (-Z), Water vapor | *T* | ***809.5*** | 822.85 | ***840.5*** | $O_2$: 1.3 nm; WV: ~0.5 nm | | | 809 | 841 |
| 12 | Ca II | *S* | 849.82 | 854.25 | 866.24 | 0.38 | 0.56 | 0.48 | 849 | 866 |
| 13 | Water vapor | *T* | ***925*** | ***980*** | | contiguous features ~0.5 nm | | | 925 | 980 |

The best matching spectral parameters can be retrieved using two different methods, named respectively $C_{ratio}$ and $C_r$, both of them are based on an iterative numerical minimization of an appropriate cost function. The $C_{ratio}$ method (Guanter et al., 2006) is based on the computation of the ratio (ρ) between the measured spectrum and the MODTRAN4 reference spectrum resampled to a given SS and FWHM:

$$\rho\ (SS, FWHM, \lambda) = \frac{E_{meas_{sc}}\ (\lambda)}{E_{mod}\ (SS, FWHM, \lambda)}$$

*Equation 3.6*

where $E_{mod}\ (SS, FWHM, \lambda)$ is the resampled reference MODTRAN4 spectrum and $E_{meas_{sc}}\ (\lambda)$ is the measured spectrum linearly normalized to the oscillation of $E_{mod}$ (i.e., min-max scaling). This linear scaling is performed in order to make the depth of the measured absorption feature similar to the modeled one. This reduces the mismatch between measured and modeled data due to differences between the atmospheric optical properties at the time of the measurement and those used for the MODTRAN4 simulation. If the FWHM and/or the SS used to compute $E_{mod}\ (SS, FWHM, \lambda)$ are different from the actual ones, $\rho$ will present large fluctuations due to the mismatch of width and position of the absorption feature between the measured and modeled spectra. The spectrometer parameters can therefore be retrieved by finding the SS and FWHM values that produce a $\rho$ characterized by the smoothest shape across the considered spectral window. This can be achieved by minimizing the following window-wise cost function which compares $\rho$ to its low-pass filtered spectrum with respect to SS and FWHM:

$$C_{ratio}(SS, FWHM, N, \lambda_0, \lambda_1) = \sum_{\lambda_0}^{\lambda_1} \left( \frac{\rho(SS, FWHM, \lambda) - \rho^{smooth}(\rho, \lambda, N)}{\rho^{smooth}(\rho, \lambda, N)} \right)^2$$

*Equation 3.7*

where $\lambda_o$ and $\lambda_1$ define the lower and upper boundary of the spectral range considered, while $\rho^{smooth}(\rho, \lambda, N)$ is computed applying a low pass filter of width *N* (expressed in number of neighboring channels) to $\rho(SS, FWHM, \lambda)$.

The *C<sub>r</sub>* method is instead based on the hypothesis that $E_{meas_{sc}}\ (\lambda)$ and $E_{mod}\ (SS, FWHM, \lambda)$ should be highly spectrally correlated when the SS and FWHM used for the resampling of the MODTRAN4 simulation match the true parameters of the spectrometer analyzed. Therefore, SS and FWHM are retrieved minimizing the following window-wise cost function with respect to SS and FWHM:

$$C_r(SS, FWHM, \lambda_0, \lambda_1) = 1 - r_{Emeas\_Emod}(SS, FWHM, \lambda_0, \lambda_1)$$

*Equation 3.8*

where $r_{Emeas\_Emod}(SS, FWHM, \lambda_0, \lambda_1)$ is the Pearson's correlation coefficient between $E_{meas_{sc}}\ (\lambda)$ and $E_{mod}\ (SS, FWHM, \lambda)$ evaluated in the interval [$\lambda_o$, $\lambda_1$].

With both methods, the iterative minimization is started imposing values for SS and FWHM equal to the nominal values for the spectrometer analyzed (i.e., nominal calibration). In the following analysis the $C_{ratio}$ method has been used.

A single MODTRAN4 parameterization is used to run the algorithm for all the spectrometers investigated. The atmospheric parameters necessary for irradiance simulation were specified as follows: target at sea level, mid-latitude summer atmospheric model, rural aerosol model, 23 km visibility, 30° solar zenith angle, 0° solar azimuth angle, DISORT 8 streams scattering option, 1 $cm^{-1}$ MODTRAN band model, and corrected Kurucz database for the solar top of atmosphere irradiance. Two model simulations with the same output SSI (0.01 nm) and different FWHM (0.064 and 0.1 nm) were generated. The former is used as the reference spectrum for the "*ultra-fine*" resolution spectrometer, while the latter is used for the "*fine*" resolution spectrometer. MODTRAN4 output wavelengths are corrected for the refractive index of air using the formula of Edlen (1966).

The proposed algorithm was implemented in an Interactive Data Language (IDL) development environment (ITTvis IDL 7.1.1). Minimization of the cost functions was based on the IDL routine TNMIN (Markwardt, 2008), a nonlinear optimization algorithm based on the truncated- Newton method, which was used in the constrained mode. SS and FWHM were allowed to vary in a ± 2nm interval and between a quarter and four times the nominal FWHM, respectively.

At each spectral window of Table 3.5, the width of the range to be considered for the retrieval of the spectral parameters was arbitrarily selected in order to include the absorption feature and its surroundings. We chose to set the range keeping into account the SSI of the instrument being used as follows: $[\lambda_0, \lambda_1] = [Range_{min} - 10\ SSI, Range_{max} + 10\ SSI]$, where $Range_{min}$ and $Range_{max}$ represent the shortest and longest wavelengths of the spectral window considered (Table 3.5), and 10 is a "scale" factor which extends the range of analysis to the left and to the right of the feature shoulders, thus determining the proportion of the spectrum unaffected by the absorption. The width N of the smoothing kernel used in equation 3.5 was set to 5 channels, a value that allows to obtain a smooth spectrum without losing the original shape (Guanter et al., 2006).

At each step of the minimization, the algorithm resamples the reference spectrum to a new FWHM and SS. While the imposition of the SS is straightforward, the resampling from the MODTRAN4 original resolution ($FWHM_o$) to a degraded one ($FWHM_d$) needs some mathematical manipulation. Assuming that the spectral response function can be approximated by a Gaussian function, the resampled spectrum is computed as the convolution of the original spectrum with a kernel K computed as a function of the original and degraded FWHMs:

$$E_{mod}(\lambda, SS, FWHM_d) \approx \int_{\lambda'=\lambda-hw}^{\lambda'=\lambda+hw} E_{mod}(\lambda', SS, FWHM_o)\, K(\lambda-\lambda')d\lambda'$$

$$K(\lambda-\lambda') = \frac{2\sqrt{2\ln 2}}{\sqrt{FWHM_d^2 - FWHM_o^2}\ \sqrt{2\pi}}\, exp\left(-\frac{4(\ln 2)\lambda'^2}{FWHM_d^2 - FWHM_o^2}\right)$$

*Equation 3.9*

where $\lambda$ is the wavelength, $\lambda'$ is the integration variable, and hw is the half width of the kernel, which was set to 10 times $FWHM_d$ to limit computing time without loss of accuracy. Note that for $FWHM_o \rightarrow 0$, K is a Guassian with $FWHM_d$.

Spectral characterization of the developed instruments is done routinely to keep upgraded the spectral calibration coefficients of the instruments along the time window of field activities. A dataset of downwelling spectral irradiance ($E^{TOT}$) collected by HSI during summer 2010 is used to evaluate the instrument spectral behavior in the time. Three different days (June 22; August 25, September 22) spread through the measurement operation time window (May 20 – October 15) have been selected to apply the SpecCal algorithm. Spectral data collected in the morning, at midday and in the afternoon are included in the dataset in order to assess the diurnal behavior of SS and FWHM. Such dataset would be representative of the variation of the instrument spectral behavior at both diurnal and seasonal time scales.

Results of the spectral characterization obtained using *SpecCal* algorithm are reported in this section. *Spectral Shift* (SS) and the *Full Width at Half Maximum* (FWHM) detected on June 22, August 25 and September 22 during field operations are reported in Figure 3.12. "*Fine*" (SPEC1) and "*ultra-fine*" (SPEC2) resolution spectrometers are reported in the upper (A) and lower (B) graphs respectively.

The spectral coverage provided by SPEC1 allows to use all the absorption features listed in Table 3.5 to accurately evaluate the spectral calibration of the spectrometer The SS is referred to the wavelength vector upgraded with the factors estimated in the last laboratory calibration (January 29, 2010). SS shows variable values in the three days analyzed. Negative values indicate that the measured spectral irradiance ($E^{TOT}_{meas}$) is shifted to greater wavelengths.

*Figure 3.12: Spectral characterization of HSI during field operation in 2010. Results of SS detection using SpecCal algorithm for "fine" (SPEC1) and "ultra-fine" (SPEC2) resolution spectrums are reported in upper (A) and lower (B) panels, respectively. The small spectral coverage provided in the NIR range by SPEC2 allows using only one absorption feature: the $O_2$-A absorption band (760nm).*

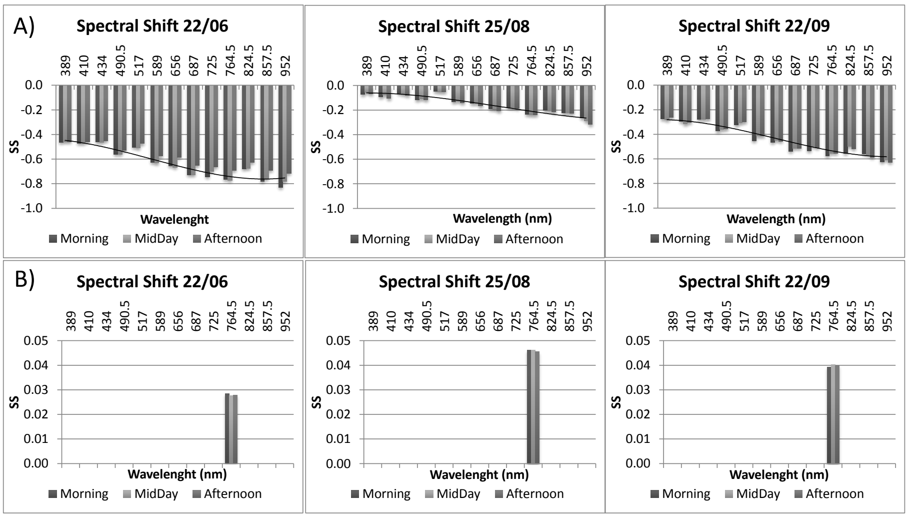

Maximum values are observed on June 22 (from -0.451 nm to -0.830 nm), while the minimum ones on August 25 (from -0.046 nm to -0.315 nm). Intermediate values are observed on September 22 (from -0.262 nm to -0.628 nm). Such behavior indicates that the spectral calibration doesn't undergo a (constant) progressive degradation during the season. Variations in air temperature may affect the SS, in fact maximum air temperatures were 12.0°C, 13.2°C and 18.4°C for June 22, September 22 and August 25 respectively. Since the *Spectral Sampling Interval* (SSI) of the "*fine*" resolution spectrums is fixed to 0.24 nm, the absolute values of the *Spectral Shift* expressed in terms of number of SSI (minimum measurable unit in the spectral domain) are less than 4. Daily variations of SS are smaller than the seasonal ones and they are always lower than the SSI. *Spectral Shift* depends on the wavelength, in particular SS increases with wavelength.

Spectral irradiance data collected by the "*ultra-fine*" resolution spectrometer (SPEC2) provide a spectral coverage of about one hundred nanometers centered at $O_2$-*A* absorption band (760 nm). The spectral range investigated allows applying SpecCal algorithm only at the absorption feature at 760 nm (window #10 in Table 3.5).

As observed for SPEC1, maximum variation of SS are detected on August 25 (from 0.045 nm to 0.046 nm), minimum on June 22 (from 0.027 nm to 0.028 nm), while intermediate values are detected on September 22 (from 0.039 nm to 0.040 nm). Contrary to SPEC1, SS values of the "*ultra-fine*" resolution spectrums are positive, thus spectrums are shifted towards shorter wavelengths. Since the *Spectral Sampling Interval* (SSI) of the "*ultra-fine*" resolution spectrums is 0.02 nm, *Spectral Shift* variation expressed in terms of number of SSI units is less than 3 (thus comparable to the ones observed for SPEC1). Daily variations of SS are smaller than the SSI, consequently they are negligible.

The SpecCal algorithm developed by Meroni et al. (2010) was tested on the automatic systems HSI in order to routinely check the spectral calibration of the instrument during long-term field measurement operations (seasons). The retrieved information were used to correct the spectrums collected in order to provide continuously spectrally calibrated data.

## 3.4.2.2 Radiometric Calibration

The radiometric calibration consists in the determination of the coefficients (gains) to calculate the spectral irradiance $W*m^{-2}*nm^{-1}$ or radiance $W*m^{-2}*sr^{-1}*nm^{-1}$ in physical units from the raw values (counts) recorded by the instrument. The development of an empirical procedure to in situ calibrate the automatic spectrometric systems is presented in this section. The need to carry out radiometric calibration during instrument field operation comes from the particular foreoptic used. The cosine response receptor optic of HSI and MRI is in fact difficult to calibrate in laboratory because it requires expensive devices available only in well-equipped calibration facilities. In order to overcome this limitation a *Field Intercalibration* procedure (FI) was used to calibrate the HSI and MRI during field measurements. Furthermore this approach allows to upgrade the instrument calibration factors/coefficients without the need to bring them to the laboratory. The proposed FI methodology is based on simultaneous measurements of spectral sun incident radiance using the reference manual system during the daily operations of the “non-calibrated” systems. Determination of the radiometric calibration coefficients is made comparing band-by-band the calibrated values (reference manual system) whit those measured by the automatic systems. Simultaneous measurements were repeated throughout the day in order to record data with wide variations of Sun Zenith Angle (SZA) and to obtain calibration values that are independent of the lighting conditions.

Reference spectral data were recorded employing traditional field spectroscopy techniques (Milton et al., 2009) during a fully clear sky day. Spectrometers equipped with bare fiber optic (FOV = 25°) were used to measure the sun incoming radiance reflected by the calibrated Spectralon panel (Labsphere, USA). Manual system and HSI/MRI share the same detectors (spectrometers), technical features of the reference and non-calibrated systems used are summarized in Table 3.6. The incident irradiance measured with different instruments and foreoptics (cosine receptors/bare fibers) is expected to differ at large SZA (e.g. greater than 70°) due to the worsening of the cosine response and/or the Spectralon panel's non-lambertian response. For this reason, measurements acquired at large SZA are not considered in the radiometric calibration and subsequent data analysis.

*Table 3.6: Technical features of the detectors used in the Field Intercalibration activity*

| System | Spectrometer ID (*serial*) | Spectral range (nm) | Nominal FWHM (nm) | Actual FWHM (nm) |
|---|---|---|---|---|
| **manual** | manual_SPEC1<br>*(HR4C1078)* | 400-1000 | 1.0 | 0.955 |
| **manual** | manual_SPEC2<br>*(HR4C1076)* | 700-800 | 0.1 | 0.162 |
| **HSI** | HSI_SPEC1<br>*(HR4C1077)* | 400-1000 | 1.0 | 0.802 |
| **HSI** | HSI_SPEC2<br>*(HR4C1168)* | 700-800 | 0.1 | 0.192 |
| **MRI** | MRI_SPEC1<br>*(HR4C1178)* | 400-1000 | 1.0 | 1.067 |
| **MRI** | MRI_SPEC2<br>*(HR2A707)* | 700-800 | 0.1 | 0.164 |

*Nominal* FWHM is the value indicated by the spectrometer factory while the *actual* FWHM was estimated in laboratory before the installation of the instrument in field using the methodology reported in section 3.4.1.

Simultaneous spectral measurements were collected at the same time, in the same area, in order to have comparable spectrums.

As an example, measurement set-up used for the cross-calibration of MRI is depicted in Figure 3.13, instrument FOV of both systems (reference manual and MRI) observes a calibrated white reference panel with a nadir view.

*Figure 3.13: Field set-up used for FI between the reference and the MRI system. The tripod on the left supports the terminations of the optical channels of MRI, while the tripod on the right leads the optical fibers of the reference system. The down-looking optical fibers of MRI observe the Spectralon reference panel as well as the optical fibers of the reference system. The uplooking cosine foreoptics of MRI point the sky (zenith view).*

As an example, spectrums acquired in field with the MRI and the reference system are shown in Figure 3.14. The MRI spectrums are in digital number while the reference spectra in radiance units (W $m^{-2}$ $sr^{-1}$ $nm^{-1}$). The objective of the procedure is to calculate the coefficients to convert the raw digital numbers measured by MRI (blue line) to the absolute radiance values measured by the reference system (red line), under the same measurement conditions, i.e. same target measured at the same time. In order to compare spectrums collected by different spectrometers, the following pre-processing steps have to be applied to the spectral data:

1. Correction of spectral-shift using SpecCal algorithm;
2. Homogenization of instrument FWHM;
3. Homogenization of SSI.

More in detail, once corrected for the spectral shift, the data acquired with the reference system are resampled to the FWHM and SSI of the system to be calibrated.

*Figure 3.14: Examples of spectral dataset used in the Field Intercalibration. Upper charts: spectrums collected with the VNIR spectrometers (SPEC1). Lower charts: spectrums collected with NIR high resolution spectrometers (SPEC2). On the left the full spectral cover of the spectrometers is depicted; on the right a detail of the $O_2$ absorption band at 760nm.*

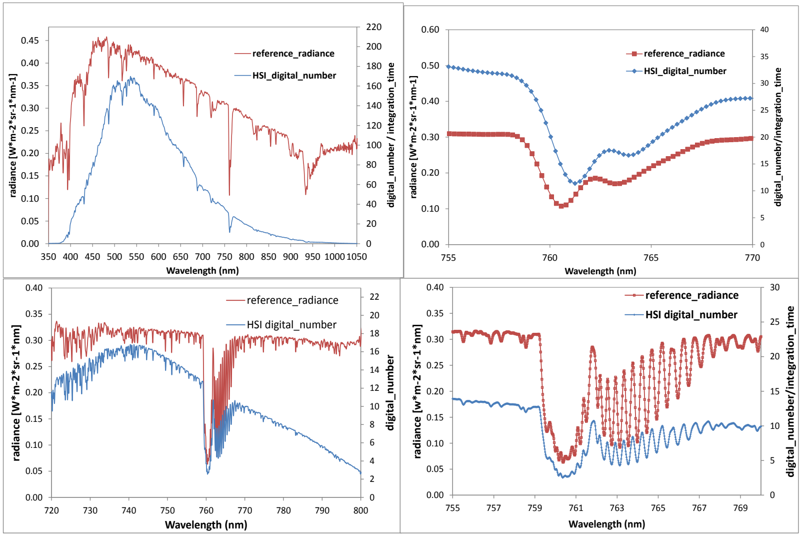

Band-by-band regression analysis between reference radiance values (manual system) and raw digital numbers (MRI) allows the estimation of the radiometric coefficients. A slope regression model Y = m*X, where y is the digital number measured by the MRI and x is the radiance recorded by the reference system was used to fit the spectral data (as an example in Figure 3.15 the regression analysis for the band at 600 nm is reported). The slope value of the model represents the radiometric gain factor. The calculation is done for each of the 3648 bands of the spectrometer.

*Figure 3.15: Example of linear regression between radiance values measured by the reference system and raw values measured by the automatic system.*

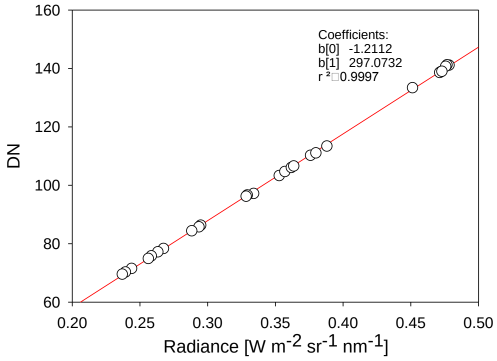

Radiometric gains computed in the spectral range covered by the spectrometers are smoothed using the Lowees algorithm. It provides a robust locally weighted regression and it's well suited to smooth data for which no formal model exists.

Results of the Field Intercalibration process are reported in Figure 3.16. The spectral shift detected in the SPEC1 of MRI was corrected, a new vector of wavelength values was computed and the result can be observed in Figure 3.16. MRI spectrums in radiance units derived by the calibration procedure agree quite well with the reference spectrums at all wavelengths. Slight differences are probably caused by the small differences in the instrument FWHM (intrinsic instrument feature).

Nevertheless the FI process was applied independently to the SPEC1 and SPEC2, a good agreement in spectral and radiometric behavior was observed (Figure 3.16).

*Figure 3.16: Results of the Field Intercalibration. Upper charts: spectrums collected with the VNIR spectrometers (SPEC1). Middle charts: spectrums collected with NIR high resolution spectrometers (SPEC2). On the left the full spectral cover of the spectrometers is depicted; on the right a detail of the $O_2$ absorption band at 760 nm. Lower charts: comparison of the spectral radiance measured by the spectrometers employed in the MRI (SPEC1, SPEC2)*

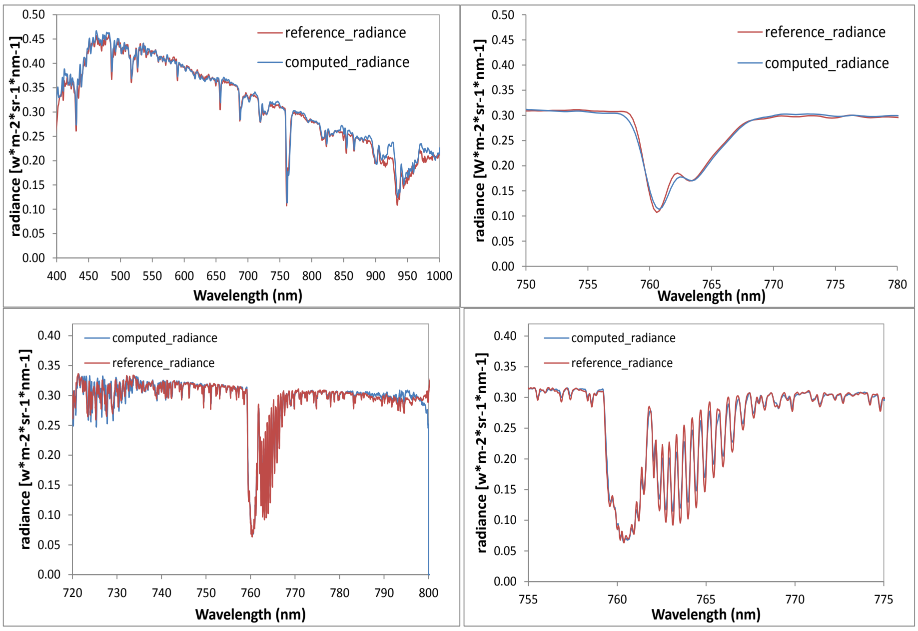

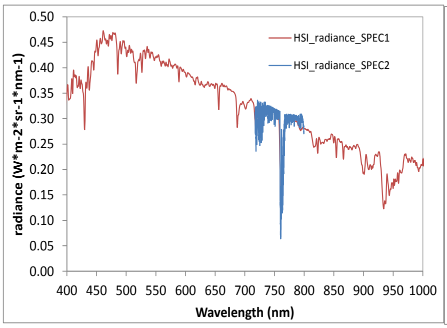
0.50
0.45
0.40
0.35
0.30
0.25
0.20
0.15
0.10
0.05
0.00
radiance (W*m-2*sr-1*nm-1)
400 450 500 550 600 650 700 750 800 850 900 950 1000
Wavelength (nm)
HSI_radiance_SPEC1
HSI_radiance_SPEC2

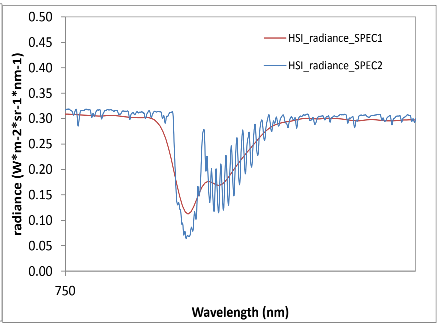
0.50
0.45
0.40
0.35
0.30
0.25
0.20
0.15
0.10
0.05
0.00
radiance (W*m-2*sr-1*nm-1)
750
Wavelength (nm)
HSI_radiance_SPEC1
HSI_radiance_SPEC2

# Bibliography

Baldocchi, D., 2008. Breathing of the terrestrial biosphere: lessons learned from a global network of carbon dioxide flux measurement systems. Australian Journal of Botany, 56(1): 1-26.

Berk, A. et al., 1998. MODTRAN cloud and multiple scattering upgrades with application to AVIRIS. Remote Sensing of Environment, 65(3): 367-375.

Damm, A. et al., 2010. Remote sensing of sun induced fluorescence to improve modelling of diurnal courses of Gross Primary Production (GPP). Global Change Biology, 16(1): 171-186.

Daumard, F. et al., 2010. A Field Platform for Continuous Measurement of Canopy Fluorescence. Ieee Transactions on Geoscience and Remote Sensing, 48(9): 3358-3368.

Edlen, B., 1966. The refractive index of air. Metrologia, 2: 71–80.

Gamon, J.A., Penuelas, J. and Field, C.B., 1992. A Narrow-Waveband Spectral Index That Tracks Diurnal Changes in Photosynthetic Efficiency. Remote Sensing of Environment, 41(1): 35-44.

Gamon, J.A., Rahman, A.F., Dungan, J.L., Schildhauer, M. and Huemmrich, K.F., 2006. Spectral Network (SpecNet) - What is it and why do we need it? Remote Sensing of Environment, 103(3): 227-235.

Gao, B.C., Montes, M.J. and Davis, C.O., 2004. Refinement of wavelength calibrations of hyperspectral imaging data using a spectrum-matching technique. Remote Sensing of Environment, 90(4): 424-433.

Grace, J. et al., 2007. Can we measure terrestrial photosynthesis from space directly, using spectral reflectance and fluorescence? Global Change Biology, 13(7): 1484-1497.

Green, R.O., Pavri, B.E. and Chrien, T.G., 2003. On-orbit radiometric and spectral calibration characteristics of EO-1 Hyperion derived with an underflight of AVIRIS and in situ measurements at Salar de Arizaro, Argentina. Ieee Transactions on Geoscience and Remote Sensing, 41(6): 1194-1203.

Guanter, L., Estelles, V. and Moreno, J., 2007. Spectral calibration and atmospheric correction of ultra-fine spectral and spatial resolution remote sensing data. Application to CASI-1500 data. Remote Sensing of Environment, 109(1): 54-65.

Guanter, L., Richter, R. and Moreno, J., 2006. Spectral calibration of hyperspectral imagery using atmospheric absorption features. Applied Optics, 45(10): 2360-2370.

Guanter, L. et al., 2009. Scene-based spectral calibration assessment of high spectral resolution imaging spectrometers. Optics Express, 17(14): 11594-11606.

Hilker, T., Coops, N.C., Nesic, Z., Wulder, M.A. and Black, A.T., 2007. Instrumentation and approach for unattended year round tower based measurements of spectral reflectance. Computers and Electronics in Agriculture, 56(1): 72-84.

Hilker, T. et al., 2008a. Effects of mutual shading of tree crowns on prediction of photosynthetic light-use efficiency in a coastal Douglas-fir forest. Tree Physiology, 28(6): 825-834.

Hilker, T., Coops, N.C., Wulder, M.A., Black, T.A. and Guy, R.D., 2008b. The use of remote sensing in light use efficiency based models of gross primary production: A review of current status and future requirements. Science of the Total Environment, 404(2-3): 411-423.

Inoue, Y., Penuelas, J., Miyata, A. and Mano, M., 2008. Normalized difference spectral indices for estimating photosynthetic efficiency and capacity at a canopy scale derived from hyperspectral and CO2 flux measurements in rice. Remote Sensing of Environment, 112(1): 156-172.

Jacquemoud, S. et al., 2009. PROSPECT plus SAIL models: A review of use for vegetation characterization. Remote Sensing of Environment, 113: S56-S66.

Leuning, R., Hughes, D., Daniel, P., Coops, N.C. and Newnham, G., 2006. A multi-angle spectrometer for automatic measurement of plant canopy reflectance spectra. Remote Sensing of Environment, 103(3): 236-245.

Markwardt, C.B., 2008. TMIN function minimization. http://cow.physics.wisc.edu/~craigm/idl/idl.html.

Meroni, M. et al., 2010. Characterization of fine resolution field spectrometers using solar Fraunhofer lines and atmospheric absorption features. Applied Optics, 49(15): 2858-2871.

Meroni, M., Cogliati, S., Rossini, M., Panigada, C., Migliavacca, M., Barducci, A., Castagnoli, F., Colombo, R., 2010. Ground-based long-term unattended hyperspectral measurements of vegetated surfaces: instrumentation and collected data., Proceedings of ESA Hyperspectral Workshop, ESRIN, Frascati, Italy.

Meroni, M. and Colombo, R., 2006. Leaf level detection of solar induced chlorophyll fluorescence by means of a subnanometer resolution spectroradiometer. Remote Sensing of Environment, 103(4): 438-448.

Meroni, M. et al., 2009. Remote sensing of solar induced chlorophyll fluorescence: review of methods and applications. Remote Sensing of Environment, 113: 2037-2051.

Meroni, M. et al., 2008. Assessing steady-state fluorescence and PRI from hyperspectral proximal sensing as early indicators of plant stress: The case of ozone exposure. Sensors, 8(3): 1740-1754.

Milton, E.J., Schaepman, M.E., Anderson, K., Kneubuhler, M. and Fox, N., 2009. Progress in field spectroscopy. Remote Sensing of Environment, 113: S92-S109.

Nakaji, T., Ide, R., Oguma, H., Saigusa, N. and Fujinuma, Y., 2007. Utility of spectral vegetation index for estimation of gross CO2 flux under varied sky conditions. Remote Sensing of Environment, 109(3): 274-284.

Nakaji, T. et al., 2008. Utility of spectral vegetation indices for estimation of light conversion efficiency in coniferous forests in Japan. Agricultural and Forest Meteorology, 148(5): 776-787.

Painter, T.H., Paden, B. and Dozier, J., 2003. Automated spectro-goniometer: A spherical robot for the field measurement of the directional reflectance of snow. Review of Scientific Instruments, 74(12): 5179-5188.

Plascyk, J.A., 1975. Mk Ii Fraunhofer Line Discriminator (Fld-Ii) for Airborne and Orbital Remote-Sensing of Solar-Stimulated Luminescence. Optical Engineering, 14(4): 339-346.

Plascyk, J.A. and Gabriel, F.C., 1975. Fraunhofer Line Discriminator Mkii - Airborne Instrument for Precise and Standardized Ecological Luminescence Measurement. Ieee Transactions on Instrumentation and Measurement, 24(4): 306-313.

Rascher, U. et al., 2009. CEFLES2: the remote sensing component to quantify photosynthetic efficiency from the leaf to the region by measuring sun-induced fluorescence in the oxygen absorption bands. Biogeosciences Discussions, 6(1): 2217-2266.

Rossini, M. et al., 2010. High resolution field spectroscopy measurements for estimating gross ecosystem production in a rice field. Agricultural and Forest Meteorology, 150(9): 1283-1296.

Running, S.W. et al., 2004. A continuous satellite-derived measure of global terrestrial primary production. Bioscience, 54(6): 547-560.

Sims, D.A. et al., 2008. A new model of gross primary productivity for North American ecosystems based solely on the enhanced vegetation index and land surface temperature from MODIS. Remote Sensing of Environment, 112(4): 1633-1646.

## *Chapter 4*

# Data Acquisition and Processing

Automatic operation of the *HyperSpectral Irradiometer* (HSI) and *Multiplexer Radiometer Irradiometer* (MRI) spectrometric systems is based on the interaction between their hardware and software segments. Mechanical and optical hardware is described in chapter 3. This chapter instead discusses the development of the software for *Data Acquisition* and Processing. The *Auto3S* program described in the first section controls the data acquisition while the processing (calibration, radiometric index computation, data quality control and filtering) of the collected spectral data is described in the second section.

## 4.1 Data acquisition – Auto3S

Data acquisition of the HSI/MRI systems is carried out through a custom software, named *Auto3S*, which allows the automatic collection of unattended, continuous, long-term spectral measurements. This software:

- controls the opto-mechanical devices (e.g. step motors, multiplexer);
- manages the spectrometer settings (i.e. Integration Time and number of spectra averaged);
- manages the instrument measurement settings (i.e. temporal frequency of the acquisitions, system boot and shutdown time, maximum integration time allowed);
- initializes the acquisition scheme and stores the measured spectrums in a useful data format.

*Auto3S* is the automatic version of the 3S program previously developed by Meroni and Colombo, 2009 for manual acquisition of field spectroscopy measurements. All the characteristics of 3S software are conserved in Auto3S. In addition specific automatic features are added in Auto3S to control the HSI/MRI instruments. In particular it specifically designed to automate the acquisition of field spectroscopy measurements: downwelling light flux (eg. irradiance/radiance) and upwelling light flux (eg. irradiance/radiance) of the investigated surface.

The program is originally developed for plant status detection studies where "*fine*" and "*ultra-fine*" spectral resolutions are needed (i.e., 0.1 nm), for this reason it allows the simultaneous control of two spectrometers. The software package is designed to run with the automatic spectrometric systems HSI and MRI which are equipped with commercial visible/near-infrared Ocean Optics (Dunedin, USA) spectrometers, but it can be interfaced with any Ocean Optics spectrometer to collect continuous spectral measurements.

The data acquisition program is a Graphic User Interface (GUI) program developed in ANSI C integrated in the development environment LabWindows/CVI 2009 (National Instruments), compiled into an executable file to run under the Microsoft Windows operating system.

Since the two instruments developed have different hardware characteristics, *Auto3S* allows to keep the same operation scheme, but at the same time it fits with the specific characteristics of each one. Both the systems have three interfaces with the personal computer that controls them, two USB interfaces are dedicated to communication with the spectrometers, one RS232 interface is used to control the mechanical segment. The software application exploits the libraries provided with the driver OOIWinIP (OOIDrv32.lib, Ocean Optics, USA) to control the spectrometers, while simply ASCII commands are sent through the RS232 serial communication to interact with the mechanical devices.

### 4.1.1 Spectrometry techniques employed

Field spectroscopy is the quantitative measureme of light fluxes in the field. Incident solar irradiance and upwelling radiance (or irradiance) spectra are usually collected to estimate the spectral reflectance factor (ρ). The reflectance factor represents the fraction of radiant energy that is reflected by a surface. It can't be directly measured but it must be estimated from field spectroscopic measurements of incident and reflected radiance (or irradiance).

The *Auto3S* software is intended to collect measurements using the 'S*ingle Beam Sandwiched*' method (Milton et al., 2009). The methodology consists in the sequential measurement of the solar spectral irradiance (White Reference, WR), the sample surface (Sample, S) radiance (or irradiance) and a second solar spectral irradiance. Resulting acquisition scheme is: WR–S–WR. The incoming irradiance at the time of sample acquisition is estimated by linear interpolation of two solar irradiance measurements taken immediately before and after the acquisition of the sample (which is therefore 'sandwiched', e.g., Walter-Shea and Biehl, 1990).

The acquisition scheme also includes the optimization (OPT) of the spectrometer integration time (IT) and the measurement of the Dark Current (DC). The IT is the amount of time the detector "looks" at the incoming photons. This determines the amount of energy reaching the sensor (i.e., the longer the integration time the more energy it receives), and it is generally chosen to maximize the signal-to-noise ratio (SNR). DC is the electric current that flows through photosensitive devices (i.e. charge-coupled device, CCD) when no photons are entering the device and it is the main source of noise in CCD. DC is measured at the beginnin of the acquisition session, immediately after the OPT, blocking the light path to the spectrometer. Thus the resulting acquisition scheme is: OPT-DC-WR-S-WR.

Despite HSI and MRI instruments have different technical characteristics (hardware), autonomously operations are driven by the *Auto3S* program that uses the same data acquisition scheme.

## 4.1.2 Acquisition procedures and system settings

The systems can be initialized using the set-up GUI (Figure 4.1) by selecting the corresponding spectrometer configuration file (spectrometer_serial_number.spec). This configuration file is an ASCII file containing the basic spectrometer characteristics: the spectrometer type, its serial number, the third degree polynomial coefficients for wavelength calibration, the array of the radiometric gains for each spectral band. Two spectrometer units are usually operated at the same time (SPEC1/SPEC2). After the spectrometer configuration, the measurement settings are defined: COM port to use for serial communication with the instrument mechanics, temporal frequency of the acquisitions (i.e. how often an acquisition session is initialized) and the maximum integration time allowed. This last parameter prevents that the instrument acquires meaningless measurements with particularly low light conditions (i.e. early morning/late evening or overcast condition).

*Figure 4.1: Auto3S set-up Graphical User Interface. In the "Head" section (Head1/Head2) the spectrometers (Spec1/Spec2) are configured. In the "Auto_Log" section instead the automatic acquisition settings are configured*

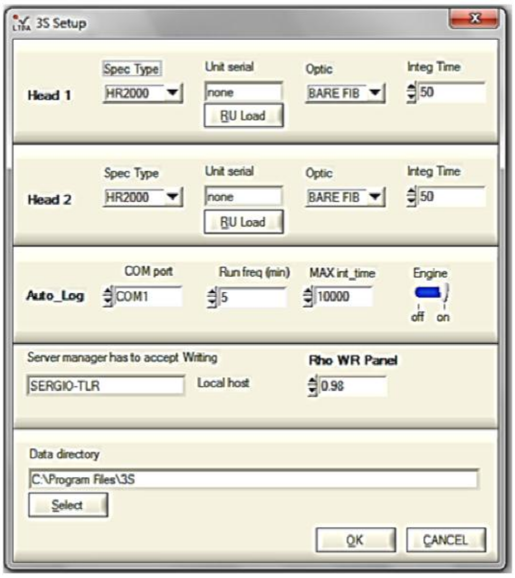

| | Spec Type | Unit serial | Optic | Integ Time |
|---|---|---|---|---|
| **Head 1** | HR2000 | none | BARE FIB | 50 |
| **Head 2** | HR2000 | none | BARE FIB | 50 |

| | COM port | Run freq (min) | MAX int_time |
|---|---|---|---|
| **Auto_Log** | COM1 | 5 | 10000 |

Server manager has to accept Writing: SERGIO-TLR Local host

**Rho WR Panel**: 0.98

Data directory: C:\Program Files\3S

Finally the set-up GUI allows the user to specify the directory in which the data will be saved and, when closed, the set-up configuration is saved to a text file (ini.txt) which is loaded automatically at the next use.

Otherwise in order to provide fully unattended operation of the HSI and MRI the AutoLog.txt file can be configured. This file contains all the information required in the set-up GUI and it is autonomously loaded when unattended start-up of the system is required. Furthermore the AutoLog.txt file allows to set the shutdown of the system at night to save power and to boot autonomously in the morning, initializing the spectrometers and all the measurement settings.

Afterwards, the data acquisition GUI is launched (Figure 4.2). The GUI panels are the same of the 3S version of the software. They are designed to be user friendly: all commands (i.e., buttons) and parameters (i.e., acquisition settings) are located in the upper part of the panel, whereas the lower part describes graphically and numerically the data being acquired.

*Figure 4.2: Example of the data acquisition GUIs for field acquisition of a vegetated surface. White, blue and yellow curves in the graphs on the left are target, white reference and dark current spectra, respectively. Red curve on the right refers to current raw reflectance spectrum. Upper GUI refers to SPEC1 (MASTER) while lower GUI refers to the SPEC2 (SLAVE).*

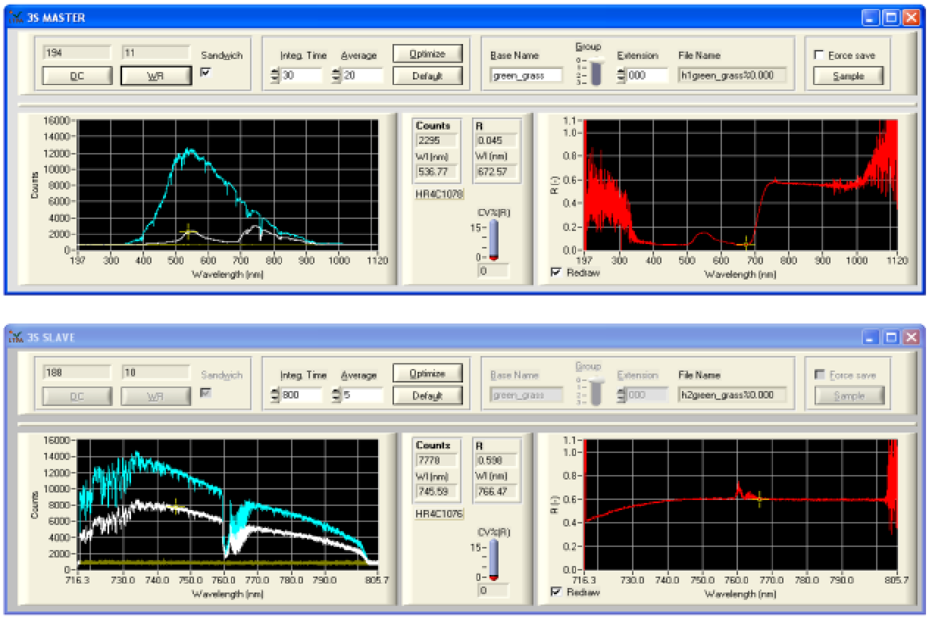

3S MASTER

194 11 Sandwich ☑

Integ. Time 30 Average 20

Base Name green_grass Extension 000 File Name h1green_grass%0.000

☐ Force save

Counts 2295 Wl (nm) 536.77

R 0.045 Wl (nm) 672.57

HR4C1078

CV%(R) 0

☑ Redraw

3S SLAVE

188 10 Sandwich ☑

Integ. Time 800 Average 5

Base Name green_grass Extension 000 File Name h2green_grass%0.000

☐ Force save

Counts 7778 Wl (nm) 745.59

R 0.598 Wl (nm) 766.47

HR4C1076

CV%(R) 0

☑ Redraw

Graphical interfaces have the only purpose to display run-time spectral data and the measurement settings because all the measuring operations are managed autonomously by *Auto3S*. A single acquisition session is launched at regular time defined before to run the unattended session.

Two identical Graphical User Interfaces are displayed, the MASTER GUI is linked to the “fine” resolution VNIR spectrometer (SPEC1) that covers the VNIR optical domain, the SLAVE GUI to the “ultra-fine” resolution spectrometer (SPEC2) that covers the 700-800 nm spectral range.

The graph on the bottom-left part of each GUI panel (Figure 4.2) shows the run-time intensity spectrum of the surface currently observed (white curve) and the stored spectra (DC and WR, yellow and blue curves, respectively). The Y-axis range (Counts) is set automatically and depends on the spectrometer dynamic range. After the DC and WR spectra are stored, the raw reflectance of the current target (red curve) appears in the bottom-right graph. The reflectance Y-axis range is editable by the user, default is (0, 1.1). For example, in Fig. 4.2 we see a typical green vegetation reflectance curve in the wavelength range 200–1120 nm as acquired at canopy level by an High Resolution Spectrometer HR4000 (Ocean Optics, USA). When a file is saved, the corresponding reflectance curve turns green for an instant to inform the user that the operation was successful.

The box between the graphs provides some key numeric indicators regarding the current spectral acquisition. On the topleft frame of the box we see the intensity of the current spectrum (label ‘Counts’) at the wavelength specified below (label ‘Wl’) which is selected by the user by moving the cursor in the intensity graph. In the same manner, on the top-right frame of the box we see the raw reflectance value (label ‘R’) at the wavelength controlled by the cursor on the reflectance graph. If the reflectance value is lower than zero or greater than one, the framework is highlighted in red to indicate a possible erroneous measurement. Below these boxes, there is a virtual thermometer showing the coefficient of variation (CV, %) of the last four reflectance measurements, computed as the ratio of the standard deviation to the mean at the wavelength specified by the reflectance cursor.

For every acquisition measurement session, *Auto3S* stores a single file containing all the basic measurements needed to compute the reflectance

(‘DC’, ‘WR’ and ‘Sample’) and additional information, such as time stamp, spectrometer settings and other information. Measurements from both the spectrometers are saved in separate files (the prefixes H1 and H2 are added to filename for the first and second spectrometer, respectively). Filename is automatically set by Auto3S, it’s format is “HX_ YYYYMMDD%0.000” where: YYYYMMDD is the date of measurement, YYYY are 4 digits containg indication of year, MM the month and DD the day indication. The file extension autoincrements, so files are saved with an extension starting from .000 and incremented by a unit every time a new file is saved to disk (i.e., .001, .002 and so on).

Spectrometer settings are fundamental parameters of each acquisition session: Integration Time (IT) and spectra Average (AVG). IT (ms) is the period in which the spectrometer is measuring photons. This key acquisition parameter determines the amount of energy reaching the sensor (i.e., the longer the integration time the more energy it receives), and it is generally chosen to maximize the signal-to-noise ratio (SNR). Therefore, when observing downwelling irradiance, it should be set to a value that provides a peak intensity of the spectrum ‘just’ below the saturation value (the maximum reading of an individual CCD pixel, before saturation).

$$T(i+1) = T(i)\,\frac{Opt}{Peak(i)} \qquad \textit{Equation 4.1}$$

Integration time is setted automatically at the beginning of each session using an iterative search of the ‘optimal’ integration time, defined here as the one providing a maximum intensity of the spectrum falling in the signal interval [sv -sv/8, sv - sv/20], where sv is the saturation value. The constants 8 and 20 were chosen with the intention of finding a reasonable compromise between high SNR and rapidity of execution. They can be interpreted as follows: the intensity peak has to be above 7/8 and below 19/20 of the maximum of the dynamic range. The algorithm implemented in the software searches for ‘optimal’ integration time adjusting it iteratively. Troubles may arise when sky conditions are extremely variable (e.g. overcast), in these cases if the iterative search of the optical IT cannot be concluded in 120 sec, the measurement session is aborted and the event traced into a log file. The same log file is updated with any event connected with software or hardware failures that precluded the normal completion of the measurement cycle. In this latter case, the acquisition software reboots the computer.

Spectra average is the number of spectral acquisitions that are internally accumulated and averaged by the spectrometer before *Auto3S* receives a spectrum. Its value is therefore valid for all measurement types (WR, DC and S). For every acquisition, 10 and 4 scans (for VNIR and NIR spectrometers, respectively) are averaged and stored as a single file.

Output files are saved to disk as binary files (details reading them are given in the distribution kit provided with the software package). Besides wavelength, DC, WR and S arrays, information stored in these files relate to measurement and spectrometer settings (integration time and number of spectra averaged, sandwich, date and time of sample measurement, a double precision number indicating the number of milliseconds elapsed since previous midnight for the DC, first WR, second WR if sandwiched and Sample) and to the spectrometer characterisation (spectrometer type, serial number, CCD pixel number).

# 4.2 Data processing – OO_IDL

The processing of large amounts of spectral data produced by the automatic systems HSI and MRI is carried out with a specially developed computer code, named OO_IDL, that automates the processing operations of the raw data collected. The computation code allows to perform several elaborations/computations of the spectral data collected using *Auto3S* software package.

Data recorded by *Auto3S* software (section 4.1) are stored in binary files which contain the wavelengths array and the raw counts spectrums of the DC-WR-S-WR collected during a single acquisition session. All the information related to the settings of the system and the spectrometers are also stored. OO_IDL is developed in IDL (ITTvis IDL 7.1.1®) development environment and tested on MS Windows and GNU/Linux operative systems (OS). It has a small Graphycal User Interface (GUI) to afford the users to launch different processing tasks, but it can be also run as a command line tool giving the chance to use simply OS scripts to schedule the processing of large amounts of collected spectral data.

The computer code provides several computation tools that can be launched from the inizial GUI:

- "*Bin to ASCII*" tool converts the binary files saved by *Auto3S* to *Comma Separated Value* text files (file extention is "*.csv");
- "Basic Process Data Flow" is the standard processing tool chain: it coverts Auto3S raw data to calibrated spectrums then calculates the reflectance spectrums and a series of radiometric indices;
- "Spectral MATRIX" tool creates a single data matrix contaning the series of the selected reflectance spectral values;
- "Half-Hourly Average" tool computes the average of the radiometric indices for each half-hourly period according to the Eddy Covarinace standards, it's useful when radiometric time series have to be compared with those recorded by micro-meteorological EC stations;
- "Data quality and filtering" function applies a series of criteria to verify the data quality of the processed spectral data.

Other spectral tools (e.g. "*Compute FWHM*", "*Degrade to a given FWHM*") are available, but they are not described in this manuscript.

The main functions composing the full data processing chain of HSI /MRI spectral data are: “*Basic Process Data Flow*”, “*Data quality and filtering*” and optionally“*Half-Hourly Average*”. Details of the first two processing tool chains are descripted in the following sections.

## 4.2.1 Basic Process Data Flow

Data processing is performed using the routine "*Basic Process Data Flow*”. It provides a series of operations that are routinely carried out on spectral raw data (Digital Numbers, DN) acquired by HSI and MRI systems in order to compute spectrally and radiometrically calibrated solar irradiance (downwelling) and the irradiance (or radiance) emerging (upwelling) from the investigated surface. It allows to calculate the reflectance spectrums and to compute a series of radiometric indices.

This routine requires as input data the *Auto3S* files, the configuration file "*measurements_info.txt*" and the spectrometer calibration file. The text file "*measurements_info.txt*" allows configuring the processing settings. A detailed list of configuration parameters included in this file is reported in Table 4.1. When program runs as a GUI application, the "*measurements_info.txt*" is displayed at the beginning of the pre-processing so that it can be edited with the required information, otherwise if OO_IDL runs as command line application the file is automatically loaded.

*Table 4.1: List of parameters configurable in the "measurements_info.txt" file*

| PARAMETER | VALUES | DESCRIPTION |
|---|---|---|
| **Use_List_From_File.In** | yes/no | Enables the function to read input files list from an ASCII text file, it’s useful for large data series (seasonal analysis) |
| **PcTime** | timesaving/solar | Indicates if the time of the PC is time saving or solar |
| **OutputTime** | solar_local,UTC | Configures the time stamp in the output file |
| **Latitude** | # | Latitude of measurement |

| | | |
|---|---|---|
| | | site |
| **Longitude** | # | Longitude of measurement site |
| **Correct_Dc_Drift** | (yes/no) | Enables the correction for the drift of the Dark Current (DC) |
| **First_Optical_Black** | # | Number of the first black pixel of the spectrometer |
| **Last_Optical_Black** | # | Number of the last black pixel of the spectrometer |
| **Correct_Non_Linearity** | (yes/no) | Enables the correction for the non-linearity effect of the spectrometer |
| **Nansymbol_For_Output** | #N/D | Character used where a value is not available |
| **List_Separator** | | Delimiter for the output files |
| **Fs_Unit** | (Watts/µmol) | Output absolute values of the radiometric indices can be expressed as Watts or µmole |

The spectrometer calibration file contains the spectral and radiometric calibration coefficients. A calibration file is available for each detector (spectrometer) embedded in the automatic systems HSI and MRI.

Outputs of the "*Basic Process Data Flow*" are text files CSV (one for each input *Auto3S* file) containg calibrated spectra of WR, S, reflectance and a summary CSV file containig the values of the radiometric indices calculated for each input file processed.

## *Data calibration and reflectance computation*

The basic processing steps carried out to calibrate the spectral data and compute the reflectance spectrums includes:

1. removal of saturated spectra;
2. correction for dark current drift by using the optically black pixels;
3. Dark Current subtraction;
4. correction for CCD detector Non Linearity Effect;
5. wavelength calibration;

6. linear resampling to a constant sampling step;
7. radiometric calibration;
8. estimation of WR at the time of target measurement by linear interpolation;
9. Savitzky-Golay smoothing filter;
10. Computation of the reflectance factor.

After the removal of the saturated spectrums (1), the spectrometer Dark Current (DC) drift (2) is corrected using the optically black pixels of the spectrometers. They are a small number (20 of a total amount of 3648 pixels) of blind pixels available in the initial part of the spectrometer "CCD array" that can be used to detect DC variations during measurements. The corrected DC at the time of the sample measurement (DC($t_s$)) is computed as follows:

$$DC\ (t_S) = DC\ (t_{DC})\ \frac{\overline{DC(t_S)}}{\overline{DC(t_{DC})}} \qquad \textit{Equation 4.2}$$

where *DC ($t_{DC}$ )* is the DC measured at the beginning of the acquisition scheme (section 4.1.1), $\overline{DC(t_{DC})}$ is the average of the black optical pixels at the time of the DC measurements and $\overline{DC(t_S)}$ is the average of the black optical pixels at the time of S measurements. DC($t_s$) computed using the Equation 4.2 is then substracted to the S spectrum (3). The same DC correction is applied also to WR measurments.

CCD detector non linearity effect (4) is corrected applying a polynomial equation to the instrument raw data (*Digital Number*, DN). A 7th degree polynomial equation was used to estimate the *Non Linear Coefficients* (NLC) ($a_0$, $a_1$, $a_2$…$a_i$, i = 7) from laboratory measurements. NLC values are store in the spectrometer calibration file and used to compute the *Non Linearity Correction Array* (NLCA):

$$NLCA(\lambda) = a_0 + \sum_{i=1}^{i=7} a_i\, DN(\lambda)^i \qquad \textit{Equation 4.3}$$

It represents the correction array to be applied to the raw DN(λ) to obtain the raw DN corrected *($DN_{NLCA}$)* for the *Non Linearity Effect* according the equation 4.4.

$$DN_{NLCA}(\lambda) = {}^{DN(\lambda)}\!\big/_{NLCA(\lambda)}$$ *Equation 4.4*

Wavelength array (5) is computed using equation 4.5 which relates the wavelength (λ) with the pixel-number (p) through the Spectral Calibration Coefficients ($a_0$, $a_1$, $a_2$…$a_i$):

$$\lambda = a_0 + \sum_{i=1}^{i=n} a_i\, p^i$$ *Equation 4.5*

The degree of the polynomial equation suitable to accurately calculate the wavelength array is empirically determined with laboratory spectral calibration. A 3rd-degree polynomial equation is used in this work. The resulting wavelength array is then linearly resampled to a constant sampling step (6).

Radiometric calibration (7) of the spectral data consists in the conversion of the digital numbers measured by a spectrometer in physical units (W $m^{-2}$ $sr^{-1}$ $nm^{-1}$ for radiance (L) and W $m^{-2}$ $nm^{-1}$ irradiance (E)). The calculation in OO_IDL is done as follows:

$$L\,(\lambda) = \frac{DN(\lambda)}{IT}\, gain(\lambda)$$ *Equation 4.6*

where DN are the raw data recorded by the spectrometer, the *Integration Time* (IT) is the amount of time the detector “looks” at the incoming photons and *gains* are the spectral *Radiometric Calibration Coefficients* inferred through cross-calibration measurements performed with a reference system (section 3.4.2.2).

Finally the computation of the reflectance factor is performed estimating the sun incoming irradiance ($E^{TOT}_S$) at the time of target measurement (S) by linear interpolation techniques (8):

$$E_s^{TOT}\,(\lambda) = \left(\frac{t_s - t_0}{t_1 - t_0}\right)[E_1^{TOT}\,(\lambda) - E_0^{TOT}]\, E_0^{TOT}(\lambda)$$ *Equation 4.7*

$t_s$, is the time of S measurements while $t_0$, $t_1$ are the time of WR collected before ($E^{TOT}_0$) and after ($E^{TOT}_1$) the S measurements respectevely.

In order to remove the instrumental noise, the calibrated spectrums are then smoothed (9) using the *Savitzky-Golay* (Savitzky and Golay, 1964) low pass filter. The width of the smoothing kernel used is set to 5 channels, a value that allows to obtain a smooth spectrum without losing the original shape (Guanter et al., 2006).

The reflectance spectrum (10) is computed rationing the radiance (or irradiance) emerging from the investigated surface ($L^S/E^S$) and the incoming irradiance ($E^{TOT}$).

With HSI collecting hemispherical measurements of both downwelling ($E^{TOT}$) and upwelling ($E^S$) light fluxes, the *BiHemispehrical Reflectance* (BHR) factor is computed as:

$$BHR\ (\lambda) = \left(\frac{E^S(\lambda)}{E^{TOT}(\lambda)}\right) \qquad \textit{Equation 4.8}$$

On the contrary MRI has two different optical channels: the up-looking channel has a hemispherical FOV (measurement of $E^{TOT}$), while the down-looking channel has a FOV of about of 25° (measurement of $L^S$). The resulting reflectance factor is named *Hemispherical Conical Reflectance Factor* (HCRF) and it's calculated as follows:

$$HCRF\ (\lambda) = \left(\frac{L^S(\lambda)}{E^{TOT}(\lambda)}\right) \qquad \textit{Equation 4.9}$$

The resulting spectrums of $E^{TOT}$, $E^S/L^S$ (spectrally/radiometrically calibrated) and the derived spectral reflectance (eg. BHR/HCRF) are stored in a single CSV text file.

## *Computation of radiometric indices*

Once the pre-processing chain of the "*Basic Process Data Flow*" tool (described in the previous section) is completed, a summary file for each spectrometer (SPEC1/SPEC2) is saved. Each summary file contains indices related to the illumination conditions (SZA, $E^{TOT}$, PPFD etc.), indices related to the quality of the measurement (*Data Quality,* DQ) and a series of vegetation indices relevant for vegetation monitoring studies (eg. NDVI, PRI, F@760 etc.).

The most important radiometric indices derived from "*fine*" resolution spectrums collected by vnir spectrometer (SPEC1) are reported in Table 4.2, while a detailed description of the *DQ criteria* used in this sudy is reported in the next section (4.2.2).

*Table 4.2: List of the most important radiometric indices derived from "fine" resolution spectrums (SPEC1). Computed values are reported into a CSV summary file produced by the "Basic Process Data Flow" tool of OO_IDL. Indices are grouped in three major classes, according to their suitability in inferring illumination conditions (I), data quality (Q) and vegetation properties (V).*

| Label | Description | Reference | Target |
|---|---|---|---|
| **solar_local** | Solar time of target measurement | | |
| **DOY.dayfraction** | Time variable composed by: DOY=Day of the Year and Dayfraction | | |
| **SZA (deg)** | Solar Zenith Angle | | Q |
| **SAA (deg)** | Solar Azimuth Angle | | Q |
| **COS(SZA)** | Cosine of SZA | | Q |
| **Qs** | index related to the stability of the WR measurements | | Q |
| **Qd** | Index related to the variations of illumination intensity between WR and S meas. | | Q |
| **Ql** | Evaluation of signal optimization | | Q |
| **Qh** | Evaluation of signal optimization | | Q |
| **Qsat** | Index related to spectrums saturation | | Q |
| **totalQ** | Summary index of data quality | | Q |
| **$E^{TOT}$@400nm** | solar irradiance (WR) at 400 nm | | I |
| **$E^{TOT}$@500nm** | solar irradiance (WR) at 500 nm | | I |
| **$E^{TOT}$@600nm** | solar irradiance (WR) at 600 nm | | I |
| **$E^{TOT}$@700nm** | solar irradiance (WR) at 700 nm | | I |
| **$E^{TOT}$@800nm** | solar irradiance (WR) at 800 nm | | I |

| | | | |
|---|---|---|---|
| **$E^{TOT}$@890nm** | solar irradiance (WR) at 890 nm | | I |
| **$E^{TOT}$@990nm** | solar irradiance (WR) at 990 nm | | I |
| **PPFD** | Photosynthetic Photon Plux Density | | I |
| **R531** | Reflectance at 531 nm | | V |
| **R570** | Reflectance at 570 nm | | V |
| **PRI** | Photochemical Reflectance Index | (Gamon et al., 1992) | V |
| **R680** | Reflectance at 680 nm | | V |
| **R800** | Reflectance at 800 nm | | V |
| **SR** | Simple Ratio | (Jordan, 1969) | V |
| **NDVI** | Normalized Difference Vegetation Index | (Rouse et al., 1974) | V |
| **SAVI** | Soil Adjusted Vegetation Index | (Huete, 1988) | V |
| **MTCI** | Meris Terrestrial Chlorophyll Index | (Dash and Curran, 2004) | V |
| **EVI** | Enhanced Vegetation Index | (Huete et al., 2002) | V |
| **GEMI** | Global Environmental Monitoring Index | (Pinty and Verstraete, 1992) | V |

Radiometric indices derived from "*ultra-fine*" spectrums collected using nir spectrometer (SPEC2) are described in Table 4.3.

*Table 4.3: List of the most important radiometric indices derived from "ultra-fine" resolution spectrum (SPEC2). Computed values are reported into a CSV summary file produced by the "Basic Process Data Flow" tool of OO_IDL. Indices are grouped in three major classes, according to their suitability in inferring illumination conditions (I), data quality (Q) and vegetation properties (V).*

| Label | Description | Reference | Target |
|---|---|---|---|
| **solar_local** | Solar time of target measurement | | |
| **DOY.dayfraction** | Time variable composed by: DOY=Day of the Year and Dayfraction | | |
| **SZA (deg)** | Solar Zenith Angle | | Q |
| **SAA (deg)** | Solar Azimuth Angle | | Q |
| **COS(SZA)** | Cosine of SZA | | Q |
| **Qs** | index related to the stability of the WR measurements | | Q |
| **Qd** | Index related to the variations of illumination intensity between WR and S meas. | | Q |
| **Ql** | Evaluation of signal optimization | | Q |
| **Qh** | Evaluation of signal optimization | | Q |
| **Qsat** | Index related to spectrums saturation | | Q |
| **totalQ** | Summary index of data quality | | Q |
| **Wl of min $E^{TOT}$ at $O_2$-A** | Wavelength of minimum radiance in the $O_2$-A absorption band | | I |
| **$E^{TOT}$ _narrow** | solar irradiance (WR) averaged in a narrow band of 0.08 nm outside the $O_2$-A | | I |

| | | | |
|---|---|---|---|
| | band | | |
| **$E^{TOT}$ _broad** | solar irradiance (WR) averaged in a large band of 5.2 nm outside the $O_2$-A band | | I |
| **F_Fld** | sun induced Chlorophyll Fluorescence estimated at 760.36 nm using the FLD method (determined system) | (Meroni et al., 2009) | V |
| **R_Fld** | Reflectance retrieved at 760.36 nm using the FLD method | “ | V |
| **NF_fld_narrow** | Normalized Fluorescence computed rationing F_Fld and $E^{TOT}$ _narrow | “ | V |
| **NF_fld_broad** | Normalized Fluorescence computed rationing F_Fld and $E^{TOT}$ _broad | “ | V |
| **min_WL_Sfm** | Shorter wavelengthused in SFM | (Meroni et al., 2010) | V |
| **max_WL_Sfm** | Longer wavelength used in SFM | “ | V |
| **n_bands_Sfm** | Number of spectral bands employed in SFM | “ | V |
| **R0_Sfm** | Reflectance computed at *min_WL_Sfm* | “ | V |
| **dR/dwl** | Derivative of the reflectance in the (*min_WL_Sfm - max_WL_Sfm*) *range* | “ | V |
| **F0_Sfm** | sun induced Chlorophyll Fluorescence estimated at *min_WL_Sfm* | “ | V |
| **dF/dwl** | Derivative of sun induced Chlorophyll Fluorescence in the (*min_WL_Sfm - max_WL_Sfm*) *range* | “ | V |
| **F@760** | Fluorescence computed at | “ | V |

| | | |
|---|---|---|
| | 760 nm using Sfm | |
| **NF_Sfm_narrow** | Normalized Fluorescence computed rationing F@760 and $E^{TOT}$ _narrow | V |
| **NF_Sfm_broad** | Normalized Fluorescence computed rationing F@760 and $E^{TOT}$ _broad | V |

## 4.2.2 Data Quality and Filtering

The quality of the spectral data continuously collected by the automatic systems must be considered in order to reject inaccurate data affected by changing in illumination conditions during the completion of the whole acquisition scheme, or affected by instrumental causes. It's worth noting that non-autonomous field spectrometric campaigns are commonly conducted for only few days characterized by clear sky conditions, because changing in illumination conditions during measurements results in inaccurate measurement of light fluxes and consequently erroneous reflectance. On the contrary, automatic systems acquired measurements during the whole season every 3/5 minutes, from early morning until late evening. Therefore *Data Quality* (DQ) control procedures have to been defined to obtain accurate spectral data time series.

For such reason a number of DQ indices have been established to evaluate the quality of data collected autonomously. These indicators are based on the assessment of two major criteria: stability of the illumination conditions and performance of instrument autonomous operations (e.g. problem in optimization procedure) and they are systematically calculated by OO_IDL computer code. Subsequently, the definition of a threshold for each DQ indicator allows to automatically reject or retain each single file. These thresholds were defined analyzing data collected during the experimental field tests reported in Chapter 5. DQ indicators developed and routinely calculated by OO_IDL computer code and their thresholds are reported in Table 4.4.

*Table 4.4: List of Data Quality indicators developed to select and filter poor-quality data. Threshold is the criteria for which data are rejected.*

| ID | Label | Description | Computation | Threshold |
|---|---|---|---|---|
| 1 | **SZA** | Solar Zenith Angle | | >70 deg |
| 2 | **Qsat** | spectrum saturation | 1, if $E^{TOT}_{1}$, $E^{TOT}_{2}$ are not saturated | |
| 3 | **Qs** | stability of WR measurements | $\frac{\lvert E_1^{TOT} - E_2^{TOT} \rvert}{E_1^{TOT}} 100$ | >10% |
| 4 | **Qd** | illumination intensity variations between WR and S meas. | $E^{TOT}/E^{S}$ | >50 |
| 5 | **Ql** | evaluation of signal optimization, | $E^{TOT}/DC$ | <3 |
| 6 | **Qh** | evaluation of signal optimization, if the dynamic range is used to an extent greater than 5/8 | 1, if max($E^{TOT}$)>5/8 *sat_value | |

The indicator (1) is related to the sun position at the time of measurement; high Sun Zenith Angles cause a decrease in cosine-response of cosine-receptor foreoptics. For these reason data acquired with SZA greater than a certain threshold are rejected. Qsat (2) verifies that the collected spectrums do not present saturated values. The third indicator takes into account the stability of the irradiance measurement ($E^{TOT}$) during the completion of an acquisition session. For example if sky overcast occurs during the 2nd irradiance measurement, the quality index (3) computed as the percent variation between the first ($E^{TOT}_{1}$) and the second ($E^{TOT}_{2}$) irradiance measurement increases. Variations of the illumination conditions during S measurement ($E^{S}$) are detected assessing Qd, computed as the ratio between $E^{TOT}$ and $E^{S}$ (4). Ql (5) evaluates the ratio between $E^{TOT}$ and DC, which is a sort of signal to noise ratio, to exclude data acquired with a too low $E^{TOT}$ or a too high DC. Qh (6) allows checking that $E^{TOT}$ values are comprised between 5/8 of the saturation value and saturation (maximum of instrument dynamic range). This latter indicator is useful to exclude data collected with non-optimal spectrometer optimization parameters (i.e. spectrometer Integration Time).

Subsequently, for each indicator a threshold was defined analyzing data collected during the experimental field tests reported in Chapter 5. DQ indicators were then compared to their thresholds and any measurement is validated if it satisfies the conditions. Whenever the above criteria are not met, the acquisition is rejected and not considered further.

# Bibliography

Dash, J. and Curran, P.J., 2004. The MERIS terrestrial chlorophyll index. International Journal of Remote Sensing, 25(23): 5403-5413.

Gamon, J.A., Penuelas, J. and Field, C.B., 1992. A Narrow-Waveband Spectral Index That Tracks Diurnal Changes in Photosynthetic Efficiency. Remote Sensing of Environment, 41(1): 35-44.

Guanter, L., Richter, R. and Moreno, J., 2006. Spectral calibration of hyperspectral imagery using atmospheric absorption features. Applied Optics, 45(10): 2360-2370.

Huete, A. et al., 2002. Overview of the radiometric and biophysical performance of the MODIS vegetation indices. Remote Sensing of Environment, 83(1-2): 195-213.

Huete, A.R., 1988. A soil-adjusted vegetation index (SAVI). Remote Sensing of Environment, 25: 295-309.

Jordan, C.F., 1969. Derivation of leaf area index from quality of light on the forest floo. Ecology, 50: 663-666.

Meroni, M. et al., 2010. Performance of Spectral Fitting Methods for vegetation fluorescence quantification. Remote Sensing of Environment, 114(2): 363-374.

Meroni, M. et al., 2009. Remote sensing of solar induced chlorophyll fluorescence: review of methods and applications. Remote Sensing of Environment, 113: 2037-2051.

Milton, E.J., Schaepman, M.E., Anderson, K., Kneubuhler, M. and Fox, N., 2009. Progress in field spectroscopy. Remote Sensing of Environment, 113: S92-S109.

Pinty, B. and Verstraete, M.M., 1992. GEMI - A NONLINEAR INDEX TO MONITOR GLOBAL VEGETATION FROM SATELLITES. Vegetatio, 101(1): 15-20.

Rouse, J.W., Haas, R.H., Schell, J.A., Deering, D.W. and Harlan, J.C., 1974. Monitoring the Vernal Advancements and Retro Gradation of Natural Vegetation, Greenbelt, MD, USA.

Savitzky, A. and Golay, M.J.E., 1964. Smoothing and differentiation of data by simplified least squares procedures. Analytical Chemistry, 36: 1627 - 1639.

# Chapter 5

# Field Tests

In order to assess the capabilities of the developed automated spectrometric systems HSI and MRI, field surveys have been carried out in the framework of two international research projects. Testing activities have been focused on continuous and long-term optical sampling of vegetation to investigate optical properties of vegetation and their link with the photosynthetic activity at local scale. To address this issue HSI and MRI were installed in experimental sites equipped with micro-meteorological stations for the measurement of $CO_2$ and water vapor gas exchange between vegetation and the atmosphere using the *Eddy Covariance* technique. However the instruments developed would be useful also in other fields of application to study optical properties of other environmental compartments such as ocean, atmosphere, cryosphere, etc. Natural ecosystems (alpine pasture) and crops (alfalfa) were both investigated and the field surveys have been conducted operating the automatic systems for at least one complete growth cycle of the investigated vegetation.

HSI has been tested and operated for two years in a permanent experimental site established in the framework of the PhenoAlp project. The aim of this research activity is the study of the phenology in the Alps. Multi-year seasonal time series of hyperspectral data ("*fine*" and "*ultra-fine*") have been recorded during the 2009 and 2010 growing seasons.

MRI has been instead operated in support to the *Sen3Exp* field survey promoted by the European Space Agency (ESA) as consolidation study to the development of the *Sentinel-3* mission. Several research teams from European countries have been involved in 2009 for the characterization of land, ocean and atmosphere in a selected study area. As part of the survey, MRI was employed to monitor an entire growing cycle (27 days) of an alfalfa crop.

In this chapter the description of the measurement sites, the set-up of the instruments and the discussion of the acquired results (time series) are reported. Diurnal and seasonal behaviors of the *Vegetation Index*es (VIs), including the *Photochemical Reflectance Index* (PRI), the *sun-induced chlorophyll Fluorescence* at 760 nm (F@760) and *Gross Primary Production* (GPP) derived *by Eddy Covariance* measurements are showed. The first section refers to the activity related to HSI (PhenoAlp) while the second focuses on the MRI instrument (Sentinel-3 Experiment).

# 5.1 PhenoAlp project - HSI

*PhenoAlp*[1] is an Interreg project, co-founded by the European Regional Development Found, under the operational program for territorial cooperation Italy-France (ALCOTRA) 2007-2013. The project aims to get better understanding of phonological changes in the Alps. Project leader is the Environmental Protection Agency of the Aosta Valley (ARPA Valle d'Aosta – IT). The main research goals of this project are:

- To implement a network of observations in the involved territories (Valle d'Aosta and Savoies);
- To implement a network of observations in the involved territories (Valle d'Aosta and Savoies);
- To define a common strategy of observation and common protocols;
- To involve local communities and schools in observing phenology, with the aim of increasing people's awareness on the issue of climate change.

The project is structured in seven tasks: *Pheno-Plantes*, *Pheno-Detection* and *Phenol-Zoo* concern the observation of alpine plant and animal species through field observations, satellite data and webcam images. *Pheno-Flux* aims to assess the effects of variations in the plant growing season length on ecosystem productivity, in terms of sequestration of carbon dioxide

---

[1] Website: http://www.phenoalp.eu/

($CO_2$) from vegetation. *Inter-Pheno* concerns the evaluation of the effects of change on plant and animal phenology season. *Pheno-Form* aims to involve local communities in phenological observation activities to raise public awareness on the issue of climate change.

The PhD research activity is related to the *Pheno-Flux* action, in particular the scientific objective is to contribute to the quantification of the net carbon balance of terrestrial ecosystems on the Alps to assess the rule of climate change on these ecosystems and their ability to mitigate the impacts (Baldocchi, 2008; Baldocchi, 2003; Goulden et al., 1996; Heimann and Reichstein, 2008; Law et al., 2002; Soussana et al., 2004; Wohlfahrt et al., 2003) High-altitude ecosystems are of particular interest because, according to the IPCC scenarios (2007), they are among the most sensitive ecosystems subjected to changes in the climate system.

During this project, permanent measurement stations able to measure $CO_2$ gas-exchange using the *Eddy Covariance* (EC) technique were installed on alpine ecosystems in order to analyze *seasonal* and *interannual* variability of carbon fluxes. Such stations have been established on two experimental sites: from June 2008 in an alpine pasture (Torgnon, 2160 m a.s.l.) and from January 2010 a second EC station (with a height of 21 m) was installed in a European larch forest (*Larix decidua* Mill.) close to the pasture experimental site.

Remote Sensing (RS) techniques are widely used tools to monitor temporal and spatial evolution of structural and functional parameters of vegetation cover, type and seasonal/interannual development. Several RS studies dealt with the estimation of the carbon balance using remotely sensed information (VIs) and actually innovative in situ RS methodologies (“near-surface”) have been developed to observe key variables related to the energy dissipation pathways of vegetation (PRI and F) which would improve the modeling of the  carbon cycle components on a larger scale (Gamon et al., 2006; Meroni and Colombo, 2006; Moya et al., 2004). In particular the use of “near-surface” remote sensing observations has great potential to improve our understanding of the link between photosynthesis and optical signals.

In the framework of the PhenoAlp project, HSI has been installed in the alpine pasture site (Torgnon) to evaluate the instrument capabilities to collect seasonal time series of vegetation optical properties. The instrument has been operated in the 2009 and 2010 snow-free period (from May to October).

### 5.1.1. Experimental site and measurement station description

The study site is an abandoned pasture of the subalpine belt composed mainly by matgrass (*Nardus stricta*, *Arnica montana*, *Trifolium alpinum* and *Carex sempervirens* as dominant species), located at 2160 m a.s.l. (45°50'40'' N, 7°34'41'' E), in the North-Western Italian Alps (Torgnon - Aosta Valley). It is the measuring station of $CO_2$ gas fluxes at the highest altitude in Italy and Europe.

*Figure 5.1: Satellite mosaic (Envisat MERIS images) of Italy with the geographic localization of the experimental measurement site.*

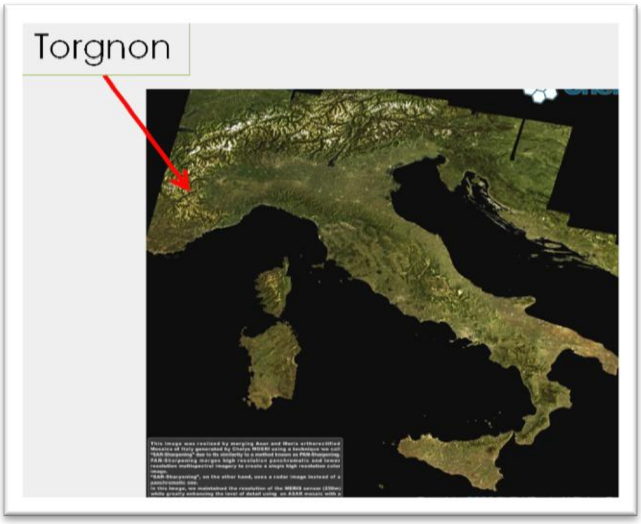

The area is classified as intra-alpine region with semi-continental climate with an annual mean temperature of 3.1 °C and mean annual precipitation of about 920 mm. The snow-free period lasts generally from late May to late October. The growing season 2009 was less rainy than 2010 with a total amount of precipitation during the snow-free period of 172.4 mm and 362 mm, respectively. The soil is classified as sandy loam according to the texture (40-50% of silt, 50-60% of sand and 4-6% of clay). The main charcteristics of the experimental site are summarized in Table 5.1.

A permanent micro-meteorological station for measurement of $CO_2$ exchanges with EC technique was installed at the experimental site (Figure5.2), moreover the automatic spectrometric system HSI regularly operated during the snow-free period (spring-summer). The measurement site is managed by ARPA Valle d'Aosta (IT) and from the Remote Sensing of Environmental Dynamics Lab. (LTDA) of the University of Milano Bicocca (IT).

*Table 5.1: Summary of the main characteristics of the experimental site.*

| Site | Torgnon (AO) |
|---|---|
| Latitude | **45°50'40'' N** |
| Longitude | **7°34'41'' E** |
| Altitude | **2160 m a. s. l.** |
| Slope | **0-5°** |
| Annual mean air temperature | **3.1 °C** |
| Annual total precipitation | **920 mm** |
| Snow-free period | **May - Oct** |
| Climate | **semi-continental** |
| Vegetation species | ***Nardus stricta***<br>***Arnica montana***<br>***Trifolium alpinum***<br>***Carex sempervirens.*** |

*Figure5.2: Picture of the permanent measurement station on the alpine pasture.*

The HyperSpectral Irradiometer allows to record unattended, continuous and long term spectrometric measurements using a rotating arm able to observe alternately the sky and the target surface (pasture). A cosine-response optic is used to measure the irradiance incident $E^{TOT}$ and upwelling from the surface $E^{S}$, allowing the computation of the Bi-Hemispherical Reflectance factor.

The VNIR data collected by the first spectrometer allows the retrieval of the reflectance spectrum and the associated vegetation indices (VIs), while higher spectral resolution NIR data from the second spectrometer permit the estimation of sun-induced fluorescence in the $O_2$-A oxygen absorption band located around 760 nm (F@760).

HSI is positioned at a height of 3.5 m above the investigated canopy using a dedicated tower depicted in figure 5.3. In this configuration, 97% of the optical footprint of HSI is represented by a circular ground area with a radius of about 20 m.

*Figure 5.3: Picture of the HyperSpectral Irradiometer operated at the PhenoAlp measurement site (Torgnon).*

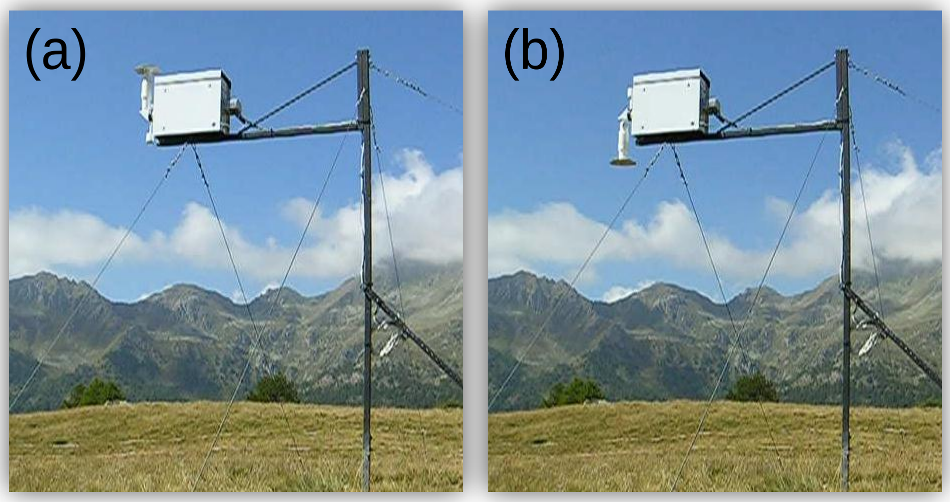

The automatic system HSI has been used to collect spectral measurements during two successive growing seasons of the investigated pasture. To avoid potential problems to the optical system and to the spectrometers due to the extreme cold temperature in winter, unattended operations have been carried out during the snow-free season, from June until October. During 2009 the instrument has been operated between June 9 and October 17 (130 measurements days), in 2010 from 20 May to 15 October (148 days). Instrument is regularly maintained (every 2 weeks): leveling and cleaning of foreoptics, silica-gel substitution and download of the stored data. A power supply system composed by 9 photovoltaic panels, 6 storage batteries and 1 tension reducer is used to feed the electronic devices.

During summer traditional field spectroscopy measurements were acquired with a portable spectrometric system operated manually (2 OceanOptics HR4000 spectrometers, for a description of the field setup see 3.3.1) over the same grassland area investigated by HSI. Spectrums were acquired using bare fibers with an angular field of view of 25°. The canopy was observed from nadir at a distance of 130 cm resulting in an observed circular area of 57.6 cm diameter. The manual rotation of a mast mounted horizontally on a tripod allowed observation of a white reference standard (Spectralon plate manufactured by Labsphere, USA) and three different circular areas of the target. The Hemispherical-Conical Reflectance Factor (HCRF) is measured with such configuration. Data collected are useful i) to radiometric cross-calibrate HSI; ii) to collect "reference" spectral properties of vegetation with traditional field spectroscopy technique.

$CO_2$, water and energy fluxes are measured using the Eddy Covariance (EC) (e.g. Baldocchi et al., 1996) technique starting from June 2008. The EC station (Figure 5.4) is part of the international *FluxNet*, a global monitoring network aimed at measuring the exchange of carbon dioxide, water vapor and energy between terrestrial ecosystems and atmosphere. Wind velocity components were measured using a three-dimensional sonic anemometer (CSAT-3 Campbell Scientific Inc., Logan UT, USA) positioned at a height of 2.5 m. Water vapor and $CO_2$ fluctuations were measured with a fast-responding open-path infrared gas analyzer (IRGA, LI-7500, LI-COR Inc., Lincoln NE, USA). Eddy fluxes were calculated with a time step of 30 minutes according to EUROFLUX methodology (Aubinet et al., 2000). Along with EC fluxes, the main meteorological variables were measured every 30 minutes, among these photosynthetically active radiation (PAR), air temperature ($T_{Air}$) and relative humidity (RH) were measured above the grassland by means of a quantum sensor (LI-190s, LI-COR Inc.) and a shielded thermo-hygrometer (HMP45C, Vaisala, Inc. Woburn MA, USA), respectively. Vapor pressure deficit (VPD) was computed from $T_{Air}$ and RH. Precipitation was measured using a tipping bucket rain gage (CS700, Campbell Scientific); soil water content (SWC) was measured with water content reflectometers (CS-616, Campbell Scientific), installed at different depth (10-25 cm) while snow height was measured with an ultrasonic distance sensor (SR50, Campbell Scientific).

*Figure 5.4: Eddy Covariance system for $CO_2$ flux measurement.*

The EC data were filtered and post-processed according to the standard procedure followed by the Carboeurope-IP project (Papale et al., 2006). For the gap-filling and the partitioning of fluxes, the marginal distribution sampling (MDS) method and the partitioning method described in Reichstein et al., (2005a), implemented in the online tool[2], were used. We selected this method because it is one of the methods adopted by the Carboeurope-IP project and FLUXNET, as standardized gap-filling and partitioning technique (Moffat et al., 2007; Papale et al., 2006). The data collected were processed by ARPA Valle D'Aosta.

---

[2] Website: http://gaia.agraria.unitus.it/database/eddyproc/

## 5.1.2. Results

### 5.1.2.1. Spectral data

This section shows the spectral data collected using the *HyperSpectral Irradiometer* during 2009 and 2010 at Torgnon. Unattended spectral data collected using the acquisition software *Auto3S* (paragraph 4.1) are pre-processed using the data processing computer code OO_IDL (paragraph 4.2). The data processing procedures include the spectral and radiometric calibration of the measured raw spectrums.

HSI has been operated for 130 days in 2009, from 9 June to 17 October, recording 9225 acquisition sessions (36900 spectrums collected). During 2010 HSI has been operated for the whole growing season, from the snow-melt (20 May 2010) until the end of the growing season (15 October 2010), for a total of 148 days. In this time range 13215 acquisition sessions were recorded (52860 spectrums) (Table 5.2).

*Table 5.2: HSI operation periods in 2009 and 2010.*

| *Year* | *From* | *To* | *Days* | *# acquisition sessions* | *# spectra collected* |
|---|---|---|---|---|---|
| **2009** | 9 Jun (DOY=160) | 17 Oct (DOY=290) | 130 | 9225 | 36900 |
| **2010** | 20 May (DOY=140) | 15 Oct (DOY=288) | 148 | 13215 | 52860 |

In 2009 only two gaps are present in the spectral time series (4 days in total) and they are due to operating system failures, while in 2010 mechanical problems were encountered during instrument operations for a total of 7 days (no data are available for DOY 184-187 and 192-194). Seasonal behaviors of the collected spectral data are commented in relation to the $CO_2$ gas fluxes measured by the Eddy Covariance technique.

### 5.1.2.2 Data quality control and filtering

The data processing code provides specific routines to assess the quality of the collected spectral data to exclude low quality data from the subsequent analyses. Data are excluded if collected with variable illumination conditions, e.g. meteorological conditions (clouds, rain or fog) cause variable irradiance during one complete set of measurements ($E^{TOT}$-$E^{S}$-$E^{TOT}$). Other sources of error can also be due to instrumental causes, for example in the automatic optimization procedure.

The fraction of data rejected amounts to 41% in 2009 and 48% in 2010. Figure 5.5 shows the amount of retained/rejected spectral data recorded by HSI in the 2009 (left panel) and 2010 (right panel) for each half-hourly interval.

*Figure 5.5: Occurrence of data rejection in the 2009 (left panel) and 2010 (right panel). time series. Rejection is higher in early morning and late afternoon when one measurement session takes longer time*

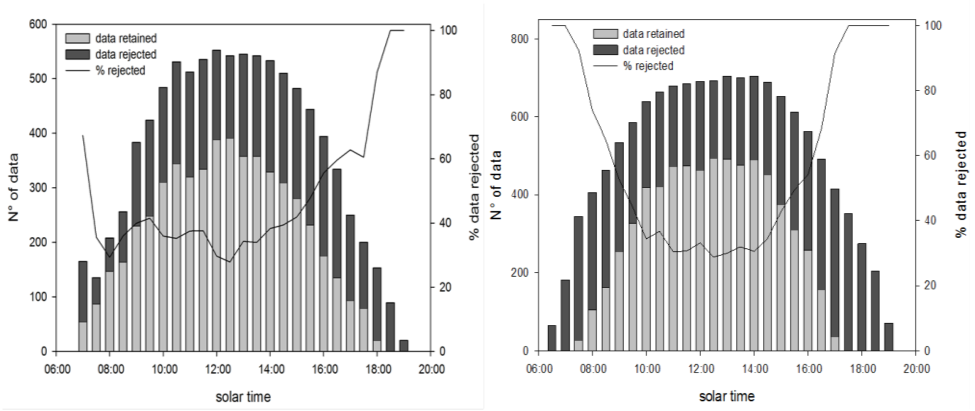

The occurrence of data rejection is always higher in early morning and late afternoon when the intensity of incident light changes quickly (due to the variation of sun position) and one acquisition session ($E^{TOT}$-$E^{S}$-$E^{TOT}$) takes longer time due to the greater spectrometer integration times. In the central part of the day the rejection is in most cases related to the instability of the incident irradiance due to frequent overcast conditions (Figure 5.5).

### 5.1.2.3 Time Series of Reflectance

Figure 5.6 shows the temporal changes of the canopy reflectance spectrums during 2009 with a ten-day step (each measurement is the average of ten spectra collected around solar noon).

*Figure 5.6: Temporal changes of average grassland reflectance spectra (n = 10) collected around solar noon during 2009 (data every 10 days are plotted). Measurements are acquired with the VNIR spectrometer.*

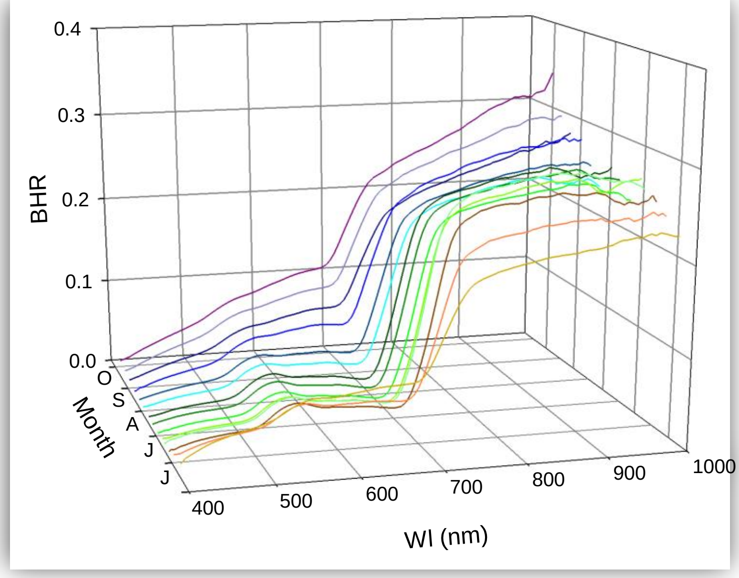

Measurements started two weeks after snow-melt when the grassland was already greening. As the growing season proceeded, reflectance in the NIR region increased as a result of increased light scattering by leaves, and the reflectance in the visible region decreased due to absorption by pigments. Maximum plant development was reached in late July. Thus in the senescent phase of the grassland (from August on) opposite behaviors occur, reflectance in near-infrared and absorption in the visible domain decrease.

### 5.1.2.4 Time Series of spectral indexes and $CO_2$ fluxes

Seasonal evolution of the most representative radiometric quantitates recorded by HSI and $CO_2$ gas flux recorded in 2009 and 2010 at the experimental site of Torgnon are presented in this section. In Figure 5.7-A, Time *Series* (TS) of the *Gross Primary Production* (GPP) derived using the *Eddy Covariance* technique, are depicted. GPP begins to rise immediately after the snow-melt at approximately DOY 150 for both years. In 2009 the time series of GPP has a gap from DOY 156 to DOY 183 due to technical failure of the micrometeorological measurement station. Maximum values of GPP are observed around DOY 185. Over the further weeks $CO_2$ uptake reaches a plateau and then slowly decreases due to autumn yellowing and senescence. In 2009, during late summer/autumn, GPP decrease shows some fluctuations at DOY 240 and 278 and in in the window DOY 172-183 in response to variations of the meteorological conditions (data not showed).

The 2009 and 2010 TS of the incident *Photosynthetic Photon Flux Density* (PPFD), which represents the total amount of incident sun light that could be absorbed by vegetation (400-700nm), are reported in Figure 5.7-B. Highly variable weather conditions are visible in the first half of the time series, in particular frequent overcast conditions occurred around noon. Better illumination conditions usually started in August.

The *Normalized Difference Vegetation Index* (NDVI) (Rouse et al., 1974) is a widely used *Vegetation Index* (VIs) related to the "*greenness*" of the investigated surface. NDVI shows similar behaviors in the two years (Figure 5.7-C) characterized by a strong increase during the vegetative phase, reaching a maximum value in early July (DOY 190). Afterwards, from August on (DOY 220), NDVI declines due to a progressive decrease of "greenness".

The *Photochemical Reflectance Index* (PRI) (Gamon et al., 1992) is a spectral index related to the carotenoid pigments of plants and it is an indicator of photosynthetic light use efficiency. The PRI seasonal trend is related to variations of both photosynthetic pigment contents and *Light Use Efficiency*, while at shorter time scales (e.g. hours or days) PRI is principally related to variations in *Light Use Efficiency*. Both the TS (Figure

5.7-D) have the same behavior in 2009 and 2010, only small differences can be identified. PRI doesn't show a strong seasonal pattern as the NDVI index.

The previously spectral quantities are computed from spectral measurements acquired with the VNIR spectrometer. The *sun-induced chlorophyll Fluorescence* at 760 nm (F@760 nm) was estimated from the high resolution data acquired with the NIR spectrometer. The seasonal behavior of F@760 nm (Figure 5.7-E) is driven by the amount of incident light and to the amount of green biomass and it is strictly related to the photosynthetic canopy APAR (Rossini et al., 2010).

*Figure 5.7: Seasonal Time Series (TS) of Gross Primary Production (GPP)(A), Photosynthetic Photon Flux Density (PPFD)(B), Normalized Difference Vegetation Index (NDVI)(C), Photochemical Reflectance Index (PRI)(D) and Sun-Induced Chlorophyll Fluorescence at $O_2$-A absorption band (F@760)(E). TS of 2009 are in dark dots, TS of 2010 in light dots. DOY is day of the year.*

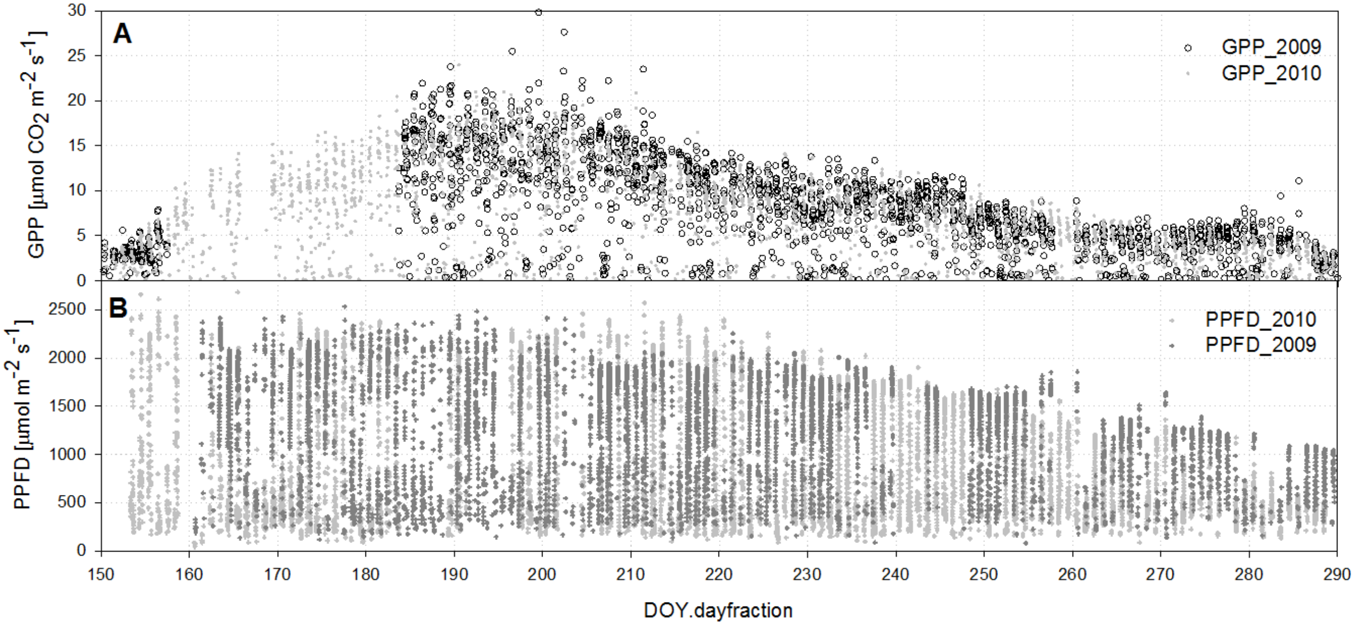

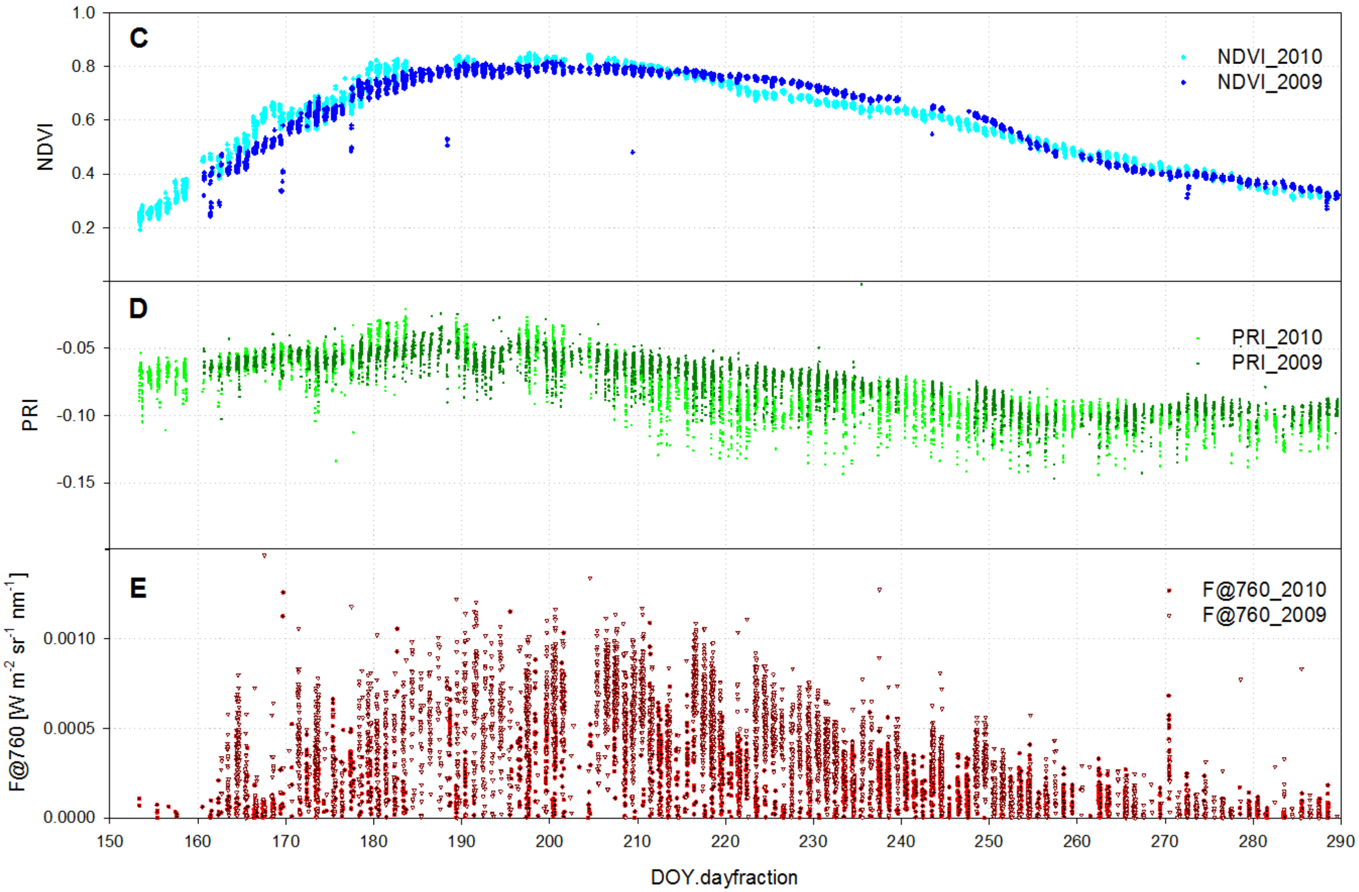
C
NDVI
1.0
0.8
0.6
0.4
0.2
NDVI_2010
NDVI_2009
D
PRI
-0.05
-0.10
-0.15
PRI_2010
PRI_2009
E
F@760 [W m-2 sr-1 nm-1]
0.0010
0.0005
0.0000
F@760_2010
F@760_2009
150
160
170
180
190
200
210
220
230
240
250
260
270
280
290
DOY.dayfraction

Monthly average of GPP and most relevant radiometric quantities investigated (PPFD, NDVI, PRI and F@760 nm) are reported in Figure 5.8. *Gross Primary Production* (Figure 5.8-A) shows a similar diurnal course for the different months, it quickly rises in the morning up to reach maximum values at about 11 AM, then it decreases slowly around midday before to drop in the afternoon. Largest annual values are observed on July when the investigated ecosystem is at its maximum development. Values of GPP in 2009 and 2010 are similar, even if they are slightly higher in 2009, in particular in July, August and October.

Diurnal courses of *Photosynthetic Photon Flux Density* (Figure 5.8-B) follow the typical daylight course characterized by maximum values at midday. Maximum values are not observed in June, as expected, but in July. This is due to the frequent overcast conditions that happen around midday in late spring. In fact, in June PPFD values show a great dispersion due to the variable weather conditions. Despite the average values recorded at midday for both years are comparable, the diurnal behaviors are affected by changes in the instrument foreoptic. Optical setup of HSI was modified in 2010 removing the 2$^{nd}$ holographic diffuser of the cosine receptor. As expected a worse cosine response is observed in the morning and in the afternoon when the Sun Zenith Angle (SZA) is far from the zenith position. This affects also the optical indices (NDVI, PRI and F@760nm) measured in 2010. It is worth noting that the aim of the modification was to reduce the time required to collect a session of measurements in order to reduce the number of data rejected due to instable illumination conditions.

The diurnal variation of the NDVI (Figure 5.8-C) is mainly related to changes in the sun-target-sensor geometry and to the architectural characteristics of the investigated vegetation (surface reflectance bidirectional effects). In June and July high values of NDVI are recorded in early morning and late evening, while minimums are at midday, when the optical path of light into the canopy is shorter. Diurnal patterns of the other months are less pronounced with similar NDVI values in the morning, at midday and in the afternoon.

*Figure 5.8: Monthly average of: A) Gross Primary Production (GPP); B) Photosynthetic Photon Flux Density (PPFD); C) Normalized Difference Vegetation Index (NDVI); D) Photochemical Reflectance Index (PRI) and E) Sun-Induced Chlorophyll Fluorescence at $O_2$-A absorption band (F@760). The vertical bars represent the standard deviation.*

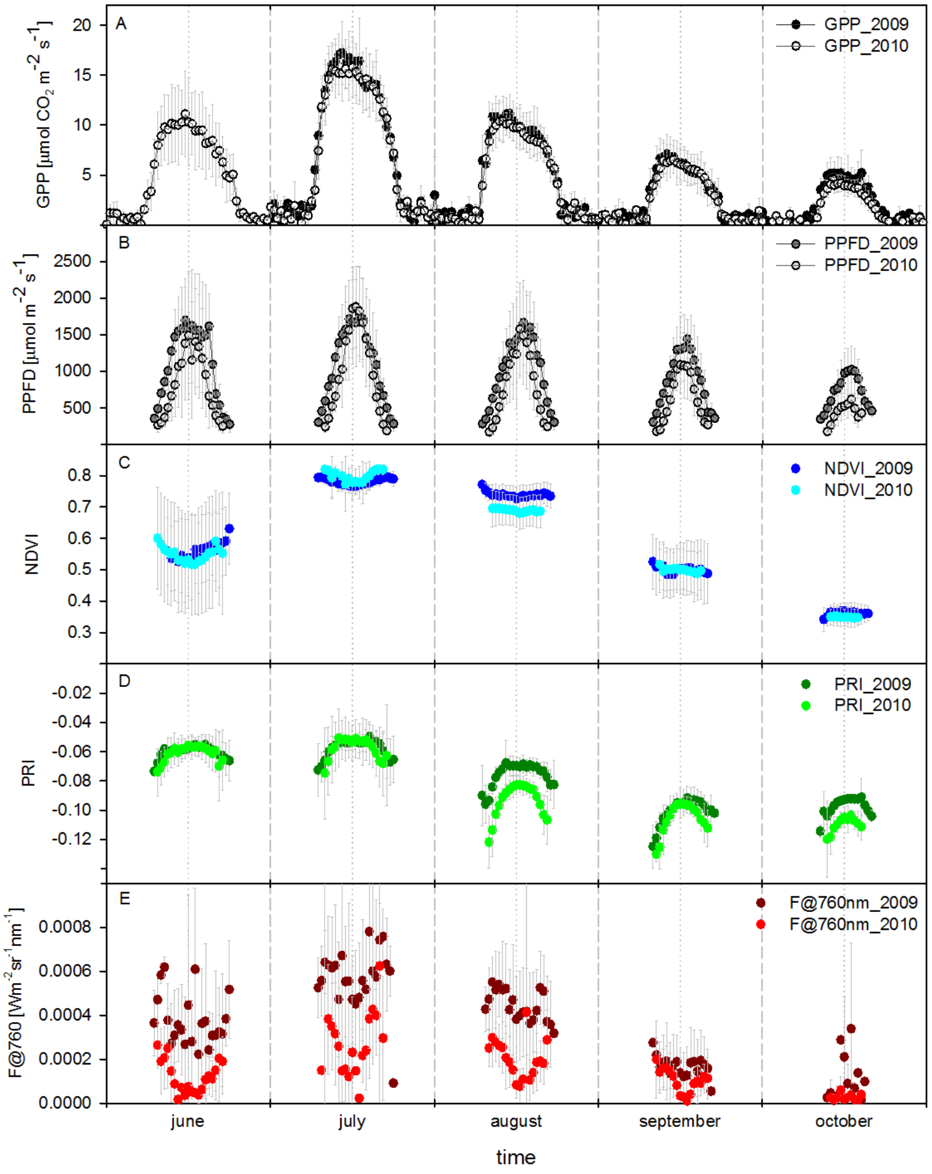

These differences in the monthly diurnal patterns are manly related to the structural characteristics of the canopy, which change during the growing season. NDVI reaches maximum values at the peak of the growing season, in July. The dispersion of the average values is higher in June, due to the fast development of the ecosystem at the beginning of the growing season, as shown in Figure 5.7-C. Diurnal and seasonal behaviors are similar in 2009 and 2010; major differences are measured in August.

The monthly average diurnal behavior of PRI is shown in Figure 5.8-D). Its diurnal course is related to the activation of the xanthophyll cycle and thus to the LUE of the vegetation. The same diurnal pattern is detected for the entire growing season: maximum values at midday and minimum values in the early morning and late afternoon. This diurnal trend of PRI is opposite to other experiments (Meroni et al., 2008a; Meroni et al., 2008b); this may be caused by the vertical posture (erectophile) of leaves that minimizes the potential for light stress at midday, even though PPFD is maximum. seasonal variation of PRI is driven by variations in the total content of xanthophyll pigments. Contrary to NDVI, PRI reaches maximum values in June, remains quite stable in July and then decreases during late summer. Values recorded in 2009 and 2010 are different in August (as for the NDVI) and on October.

*Sun-induced chlorophyll Fluorescence* values estimated at the $O_2$-A absorption band are highly scattered (i.e. large standard deviation) (Figure 5.8-E). The main reasons which could explain this behavior are: i) fluorescence represents only 1-5% of the total radiance at the sensor in the near-infrared; ii) highly variable illumination conditions could induce fast variations of the fluorescence emission (Kautsky effects). As a result, the diurnal courses of F@760 nm are more difficult to be interpreted compared with those of the optical indices. However, high values are measured in the morning and evening, while minimums appear at midday, when the optical path of light in the investigated canopy (erectophile) is smaller. The seasonal pattern of F@760 is mostly driven by PPFD, canopy biomass, canopy architecture and it is related to the photosynthetic canopy APAR (Rossini et al., 2010). Mean values measured in

2009 are generally greater than in 2010 for the entire season, only in October the F@760 values are similar.

## 5.2 Sentinel-3 Experiment -MRI

Part of the development process of new Earth observation missions concerns the assessment of future performance of sensors and evaluation of algorithms to transform the satellite data into useful information products. These assessments are made through field surveys that involve satellite, airborne and field measurements in order to collect a dataset of imagery and ground-truth information that can be used to achieve the performance analysis.

The '*Sentinel-3 Experiment'* campaign (*Sen3Exp*) was carried out in 2009 as consolidation study for the development of the Sentinel-3[3] mission, which is the third in a series of five ESA space missions developed within the Global Monitoring for Environment and Security (GMES[4]) initiative. The purpose of GMES is to ensure that in the future Europe will have autonomous access to the best, up-to-date information on the global environment, in order to define, implement and assess its policies on Environment and Security. Sen3Exp involved a series of coordinated activities with scientists making ground-based measurements in Spain, Italy and the Ligurian and Adriatic Seas, while aircraft with sensitive instrumentation passed overhead and satellites acquired data simultaneously from space. The mission's complement of optical sensors will comprise an Ocean Land Colour Instrument (OLCI), which is based on Envisat's Medium Resolution Imaging Spectrometer (MERIS), and a Sea Land Surface Temperature Radiometer (SLSTR), which is a successor to Envisat's Advanced Along Track Scanning Radiometer (AATSR).

The *Sen3Exp* campaign began in June in Barrax (Spain), then it moved to Pisa (Italy) around the San Rossore pine forest area and finally in July activities focused on the marine environment were carried out at two oceanic sites: the

---

[3] Website: http://www.esa.int/esaLP/SEMTST4KXMF_LPgmes_0.html

[4] Website: http://www.gmes.info/

Boussole monitoring buoy in the Ligurian Sea and the Aqua Alta Oceanographic Tower (AAOT) in the Adriatic Sea, close to Venice. At the same time, ground teams made atmospheric radiometric and biophysical measurements of the areas under investigation. Research teams from different European countries were involved in the field campaign to characterize atmosphere and land surface optical, thermal and biophysical properties.

In the framework of the *Sen3Exp* field survey, the automatic spectrometric system MRI was used to make unattended, continuous and long-term spectral measurements of an agricultural field (alfalfa). The possibility to work in conjunction with other research teams was very useful to evaluate MRI data and its capabilities. A mobile micrometeorological station (CNR-IBIMET) for the measurements of atmosphere/vegetation gas-exchange using EC technique was installed in the same experimental area of MRI. This allows studying the link between optical signals and photosynthetic rates of the investigated crop.

## 5.2.1. Experimental site and measurement station description

The San Rossore Natural Reserve (Riserva di San Rossore) is part of the Regional Park of San Rossore, Migliarino and Massaciuccoli, located on the Tyrrenian coast in Tuscany (Italy) (Figure 5.9) at about 10 km from Pisa (43°40’11.04’’N, 10°18’09.90’’E). The Reserve presents a wide variety of vegetation types, including maquis vegetation on the sand dunes, coniferous forest plantations dominated by *Pinus pinaster* and *P. pinea* further away from the sea, then broadleaf forests of *Quercus robur*, *Q. ilex*, *Fraxinus spp*., *Alnus glutinosa*, *Populus spp.*, as well as shrubland vegetation, grassland and agricultural crops. More intensive agricultural crops can be found 1 km south of the Reserve, in the “Centro Avanzi” experimental estate of the University of Pisa. The experimental site is located in the Pisa plain, at an elevation of 0-7 m a.s.l. The climate is Mediterranean, with a mean annual rainfall of 932 mm and a mean annual temperature of 14.8 °C; the dry or semi-arid period starts in

June and lasts until the end of September, with summer precipitation of less than 100 mm (Table 5:3 ).

*Figure 5.9: Satellite (MERIS) mosaic of Italy with the geographic localization of the experimental measurement site*

In this agriculture area a semi-permanent measurement station of optical properties and Eddy Covariance gas-flux was established in an *alfalfa* field. *Alfalfa* (*Medicago sativa L.)* is a flowering plant of the pea family Fabaceae cultivated as an important forage crop. It's a cool season perennial plant that grows to a height of 1 meter and has a deep root system that makes it very resilient to droughts. This crop is cut three to four times a year.

*Table 5:3: Summary of the main characteristics of the San Rossore experimental site.*

| Site | **San Rossore** |
|---|---|
| Latitude | **43°40'11.04''N** |
| Longitude | **10°18'09.90''E** |
| Altitude | **0-7 m a.s.l** |
| Slope | **0** |
| Annual mean air temperature | **14.8 °C** |
| Annual total precipitation | **932 mm** |
| Climate | **Mediterranean** |
| Vegetation species | ***Alfalfa* (*Medicago sativa L.)*** |

### Spectral measurements

Assessment of the MRI capabilities to collect unattended, continuous and long-term spectral data was carried out in the framework of the Sen3Exp field campaign during summer 2009. The automatic instrument is based on a commercial optical multiplexer (MPM-2000, Ocean Optics, Inc., USA) that switches the input of the spectrometers between a channel measuring the incident irradiance ($E^{TOT}$) through a fiber connected to an up-looking cosine-response optic and a channel measuring the radiance upwelling ($L^{S}$) from the surface through a down-looking bare fiber with a 25° FOV (Figure 5.10).

MRI allows the measurement of the *Hemispherical-Conical Reflectance Factor* (Schaepman-Strub et al., 2006). Two *High Resolution Spectrometer HR4000* (OceanOptics, USA) characterised by different spectral resolution are embedded in MRI: spectrometer 1 provides "*fine*" resolution spectrums in the VNIR domain (FWHM = 1.4 nm, 400 - 1000 nm spectral range); spectrometer 2 (SPEC2) has "*ultra-fine*" resolution (FWHM of 0.13 nm and a 700-800 nm spectral range). Optical and electronic components of the automatic system (optical multiplexer, spectrometers and logging computer) were housed in a thermally controlled box keeping the internal temperature at 25°C. Detailed description of the automatic system is reported in chapter 3.1.2.

The automatic MRI has been installed in field from June 13th (DOY=164) until July 19th (DOY=200) 2009 (27 days) and almost two growing cycles of the investigated crop were recorded during the instrument operations. Spectral data were measured with a three-minute time step between 7.30 a.m. and 5.00 p.m. solar time.

The average canopy plane was observed from nadir at a distance of 1.2-1.9 m, corresponding to an area of 0.53-0.84 m diameter. Four optical fibers of 5 m length were mounted on a tripod placed in the alfalfa field in the footprint area of the Eddy Covariance gas flux mobile measurement station. For every spectral acquisition, 15 and 4 scans (for Spectrometer 1 and 2, respectively) were averaged and stored as a single file using the data collection software *Auto3S* (chapter 4.1). The automatic instrument has been calibrated, in laboratory before the installation and in situ during measurement operation, according to the methodology reported in section 3.4.2.

*Figure 5.10: Multiplexer Radiometer Irradiometer MRI operated in the framework of the Sen3Exp field campaign at the alfalfa measurement site. On the left the MRI automatic system, the thermally-regulated box hosts the optical system and electronics. On the right detail of the terminations of the instrument optical system, red and green circles highlight the uplooking (cosine receptor) and downlooking (25° FOV) foreoptics, respectively.*

In order to check the reliability of the spectral data recorded by MRI, independent reflectance measurements were collected using traditional field spectroscopy techniques simultaneously with MRI operations. Traditional field spectroscopy measurements were obtained with a portable spectrometer operated manually (OceanOptics HR4000 covering the range from 400nm up to 900 nm) over the same area investigated by MRI. Spectra were acquired using bare fiber with an angular field of view of 25°. The canopy was observed from nadir at a distance of 130 cm resulting in an observed circular area of 57.6 cm diameter. The manual rotation of a mast mounted horizontally on a tripod allowed observation of a white reference standard (Spectralon plate manufactured by Labsphere, USA) and the target.

### Eddy Measurements

A complete set of meteorological variables were recorded continuously from June 2009 to the end of July. Soil temperature is recorded by temperature probes which provide the average temperature of 6 to 8 cm of soil (model TCAV-L averaging thermocouples, Campbell Scientific, Logan, Utah, USA). These probes parallel four Type-E thermocouples together into one, 24-gauge wire, and were inserted at different depths (0-30 cm, 0-20 cm, 0-10 cm in different locations). Air temperature and relative humidity are being recorded both on a must at about 2m above the ground (where also net radiometer and pyranometer were installed) and on the eddy flux tower using Vaisala HMP45C probes (Vaisala, Helsinki, Finland) (at an approximate height of 5.4 m above ground surface). Net radiation has being recorded using a net radiometer (NR Lite from 200 to 100.000nm), total radiation intensity was measured using a Kipp & Zonen model (CMP 3, 300 to 2800 nm). The net radiometer and the pyranometer were mounted on the top of the mast (where also temperature sensors were installed). Precipitation is being recorded using tipping bucket rain gauge (model 3665R, Spectrum Technologies Inc., Plainfield, IL, USA) installed on top of the cabin where the instrument were stored. All the instruments were connected to CR-10 data logger (Campbell Scientific, Logan, Utah, USA) and each environmental variable is read once every 0.1-10 seconds and the 30 minutes averages are output to a PC.

An *Eddy Covariance* (EC) flux station was installed in alfalfa field at the Centro Avanzi Experimental Fields, and was operated during the entire study period. A mast of 2.5 m was mounted at 0 meter above the sea level. Turbulent fluxes of $CO_2$, momentum, sensible and latent heat were collected using a sonic anemometer (R.M. Young Co. model 81000V) and an open-path $CO_2/H_2O$ infrared gas analyzer (IRGA; Li-Cor, Inc., Model 7500). The distance between the two sensors was approximately 0.4 m. The IRGA was inclined toward the north by an angle of 30° to minimize solar radiation interference (Li-Cor recommendation) and to facilitate the shedding of water droplets from the sensor lenses. It was calibrated before the installation and in the end of the campaign using reference gas tanks and a portable dewpoint generator (Li-Cor

Model 610). Raw data were acquired at the frequency of 20 hz. The meteorological station used is depicted in Figure 5.11.

*Figure 5.11: Mobile micrometeorological station installed at the alfalfa experimental field.*

Half-hourly fluxes of energy (i.e. sensible heat flux H, and latent heat flux LE), momentum (i.e. friction velocity u*) and carbon (i.e. net ecosystem exchange NEE) were derived from high frequency data using state of the art eddy covariance processing; custom processing software was developed in the Matlab environment. Case-specific procedures that have been applied include:

1. despiking procedure specifically tuned to remove erroneous IRGA data (rainy or foggy conditions);
2. an high-pass filtering with linear detrending (Aubinet et al., 2000);
3. coordinate axis rotations as described in (Aubinet et al., 2000);
4. corrections of CO2 and water (H2O) fluxes applied for air density fluctuations (Webb et al., 1980).

Quality-control procedures, including stationarity analysis and integral turbulence tests, were applied as described in Foken and Wichura (1996). Half-hourly integration time of eddy covariance measurements is commonly accepted as a good compromise between the need of accounting for proper statistics and that of reducing non stationarity problems.

Measured carbon fluxes represent net exchange (NEE), which is the result of two opposite sign components: ecosystem photosynthetic activity which is a sink or negative flux and is represented as *Gross Primary Production* (GPP), and ecosystem total respiration (i.e. the sum of autotrophic and heterotrophic components) which is a source and is represented as Reco. The convention is that both GPP and Reco have positive values, while NEE is negative for prevailing sinks and positive for prevailing sources:

$$GPP = -NEE + Reco \qquad \text{Equation 5.1}$$

A flux partioning methodology aims at partioning NEE into the components GPP and Reco

$$NEE = Reco - GPP \qquad \text{Equation 5.2}$$

The methodology we applied is explained in Reichstein et al. (2005b). Briefly, the approach is based on using night time fluxes where only respiration is going on, to characterize the functional response of respiration towards air temperature, and to derive a statistical model expressing Reco as a function of air (or soil) temperature. Then such model is applied to daytime values, and GPP is derived from Equation 5.1. Critical aspects of such methodology are:

- night time conditions typically exhibit low turbulence, thus making eddy covariance theory and requirements hard to apply; for this, sufficiently turbulent conditions only are used to estimate Reco;
- air/soil temperature at night is lower than at daytime, thus the functional relation (exponential) that is fitted with night data, is then extrapolated to daytime conditions where no direct observations exist.

To partially overcome such limitations, alternative approaches have been proposed in the literature (Gylmanov 2007, Lasslop 2009).

## 5.2.2. Results

### 5.2.2.1 Spectral data

This section shows the spectral data collected using the Multiplexer Radiometer Irradiometer during the Sen3Exp field campaign at the alfalfa field. “*Fine*” resolution data recorded by the first spectrometer allow the retrieval of the VNIR reflectance spectrum and the computation of the associated *Vegetation Indices* (VIs), the largely used *Normalized Difference Vegetation Index* (NDVI) and the *Photochemical Reflectance Index* (PRI). “*Ultra-fine*” resolution spectrometer NIR data from the second instrument permit the estimation of *Sun-Induced Chlorophyll Fluorescence* in the $O_2$-A oxygen absorption band located around 760 nm (F@760).

Unattended spectral data collected using the acquisition software *Auto3S* (paragraph 4.1) are processed using the data computer code OO_IDL (paragraph 4.2). The data processing procedures include the spectral and radiometric calibration of the raw spectra.

### 5.2.2.2 Data quality control and filtering

Data processing computer code provides specific routines to assess the quality of the collected spectral data to exclude uncertain data from the subsequent processing steps. Data are excluded if collected with variable illumination conditions due to the presence of clouds, rain or fog that may cause irradiance variations during one complete set of measurements ($E^{TOT}$-$L^{S}$-$E^{TOT}$). Other sources of error can be due to instrument failures, i.e. events connected with software or hardware failures that preclude the normal completion of the measurement cycle. Figure 5.12 shows the amount of retained/rejected spectral data. The fraction of rejected data amounts to 20.8%.

The occurrence of data rejection is always higher in early morning and late afternoon when the intensity of incident light changes quickly (due to the variations of sun position) and one acquisition session ($E^{TOT}$-$L^{S}$-$E^{TOT}$) takes longer time due to the greater spectrometer integration times. In the central part of the day the rejection are in most cases related to the instability of the incident irradiance.

*Figure 5.12: Occurrence of data rejection in the time series recorded by MRI during the Sen3Exp field campaign at the alfalfa measurement site.*

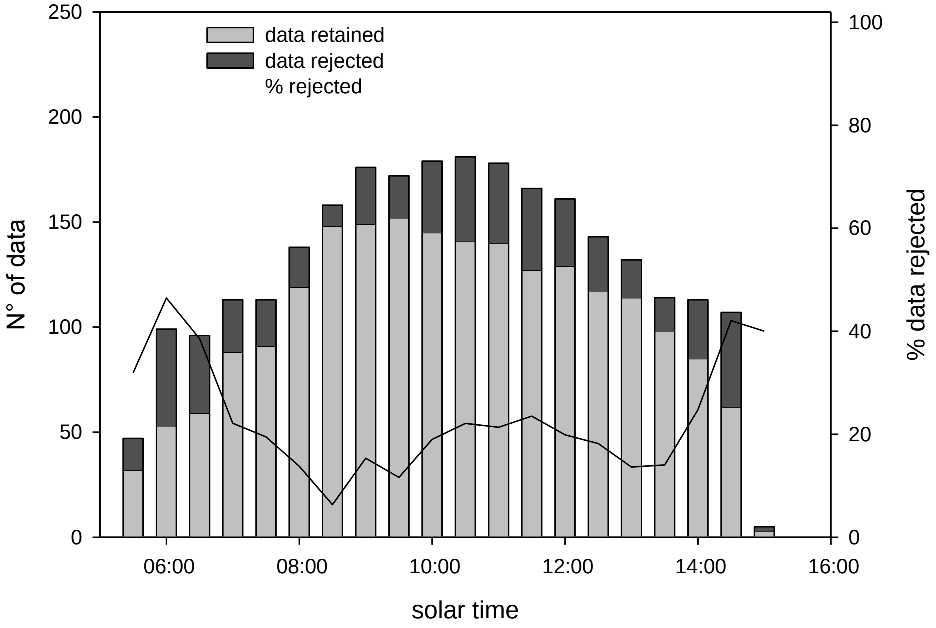

## 5.2.2.3 Time Series of spectral indexes and $CO_2$ fluxes

Time series of spectral data recorded by the *Multiplexer Radiometer Irradiometer* and Eddy Covariance $CO_2$ fluxes (GPP) are reported in this section. MRI has been operated for 27 days and collected 17 thousand spectrums covering two growth cycles of an alfalfa crop. The automatic instrument MRI has been installed at the end of the first crop growing cycle (DOY = 164) and operated until the harvesting of the second growing cycle (DOY = 207). Gaps in the spectral time series are due to crop management operations and the harvesting between the first and the second growing cycle occurred at DOY 180.

$CO_2$ fluxes measured with the mobile micro-meteorological station are available from 15 June (DOY = 163) to 31 July (DOY = 212). GPP evolution is depicted in Figure 5.13 A. It shows high values in the early days of measurement when the investigated crop was at maximum development. After the harvesting GPP drops to low values then increases quickly following the regrowth of the alfalfa. The second growth cycle shows higher carbon uptake and lower evapotranspiration, due to higher stomatal resistance (data not shown). This may be explained by a moderate water limitation in the second cycle, causing stomata closure which affects water but not carbon exchanges. Diurnal courses of GPP show a maximum around midday for most of the days. Such behavior is driven by the *Photosynthetic Photon Flux Density* (PPFD). Series of PPFD calculated using the spectral data recorded by MRI is showed in Figure 5.13 B. It represents the total amount of light that could be potentially absorbed by vegetation (spectral integral of the 400 – 700 nm range). Data show that clear sky conditions were frequent during the field campaign.

As an example of optical signals derived from the optical system Figure 5.13 shows the evolution of NDVI, PRI and sun-induced chlorophyll. Time series of the largely used *Normalized Difference Vegetation Index* (NDVI) related to the "*greenness*" of the investigated surface is reported in Figure 5.13 C. NDVI strongly responds to vegetation growth. During the early measurement days NDVI values are almost constant, except for DOY= 173 and DOY = 174 in which there was a small decrease. Following the harvesting (DOY = 180) NDVI values fall and it' is interesting to note that NDVI value undergoes a further reduction due to progressive drying of biomass waste remained on the ground. After this initial phase a rapid increasing of NDVI follows the increase of the crop biomass until it reaches a constant value, corresponding to the maximum canopy development (full cover). Strong anisotropy effects related to the sun-canopy-sensor relative position are observable in the daily courses of the spectral indices. Maxima for NDVI occur at large Solar Zenith Angles when direct sunlight beam enters obliquely the canopy and has the highest probability of interacting with foliage elements. Minimum values are observed near solar noon when light has the shortest path length through the canopy to the soil. The largest daily variation of NDVI is observed with low canopy cover (new regrowth alfalfa), where midday values are only half those observed earlier in the morning. NDVI values are significantly higher in mature alfalfa and also change appreciably with solar zenith.

The evolution of the *Photochemical Reflectance Index* (PRI) (Gamon et al., 1992) related to the excess energy dissipation of plants through the activation of the xanthophyll cycle, is shown in Figure 5.13 D. Also PRI strongly responds to vegetation growth. Both PRI and NDVI decrease sharply after harvesting (DOY 180), but PRI response is quicker because it is more related to photosynthetic activity while NDVI to the greenness of the canopy. Another difference that we can observe between NDVI and PRI is that NDVI reaches saturation before PRI when the canopy fully developed. During the second growing cycle maximum PRI values are slightly lower than in the previous cycle, accordingly to the moderate water limitation suffered by the alfalfa canopy as observed with eddy covariance data. Contrary to the NDVI, the intra-day variation does not appear to change magnitude during the growth cycle, but always presents a significant intensity also when crop is at maximum development. This may be explained by the fact that PRI diurnal variations are not only due to variations in the sun-canopy-sensor geometry but also to variations of the plant physiological status.

The previously spectral quantities are computed from spectral measurements acquired with the VNIR spectrometer. The *Sun-Induced Chlorophyll Fluorescence* at 760 nm (F@760 nm) was instead estimated from the "*ultra-fine*" resolution data acquired with the SPEC2 detector. Time series of the F@760 nm is depicted in Figure 5.13 E. The intensity of F@760 is due to the interaction of the incident photosynthetic photon flux density (PPFD), being maximum at solar noon, and the presence/efficiency of chlorophyll photosystems, being low at the beginning of the growing cycle (e.g., DOY 189) and maximum at the end of it (e.g., DOY 199).

For this reason the fluorescence signal results more influenced by variable illumination conditions compared to the other spectral indexes investigated. F@760 nm has very low values at DOY=180, but not zero values probably due to a part of biomass present on the ground. Values close to zero are reached some days (around DOY 185-186) later, when also NDVI and PRI show minimum values. From DOY 186 on F@760 quickly rises up following biomass accumulation. As already observed for PRI, F@760 reaches maximum values some days later than NDVI. Quantitative analysis of the relationships between the spectral indexes NDVI, PRI and F@760 and the $CO_2$ flux data are reported in chapter 6.

*Figure 5.13: Time Series (TS) of Gross Primary Production (GPP)(A), Photosynthetic Photon Flux Density (PPFD)(B), Normalized Difference Vegetation Index (NDVI)(C), Photochemical Reflectance Index (PRI)(D) and Sun-Induced Chlorophyll Fluorescence at $O_2$-A absorption band (F@760)(E).*

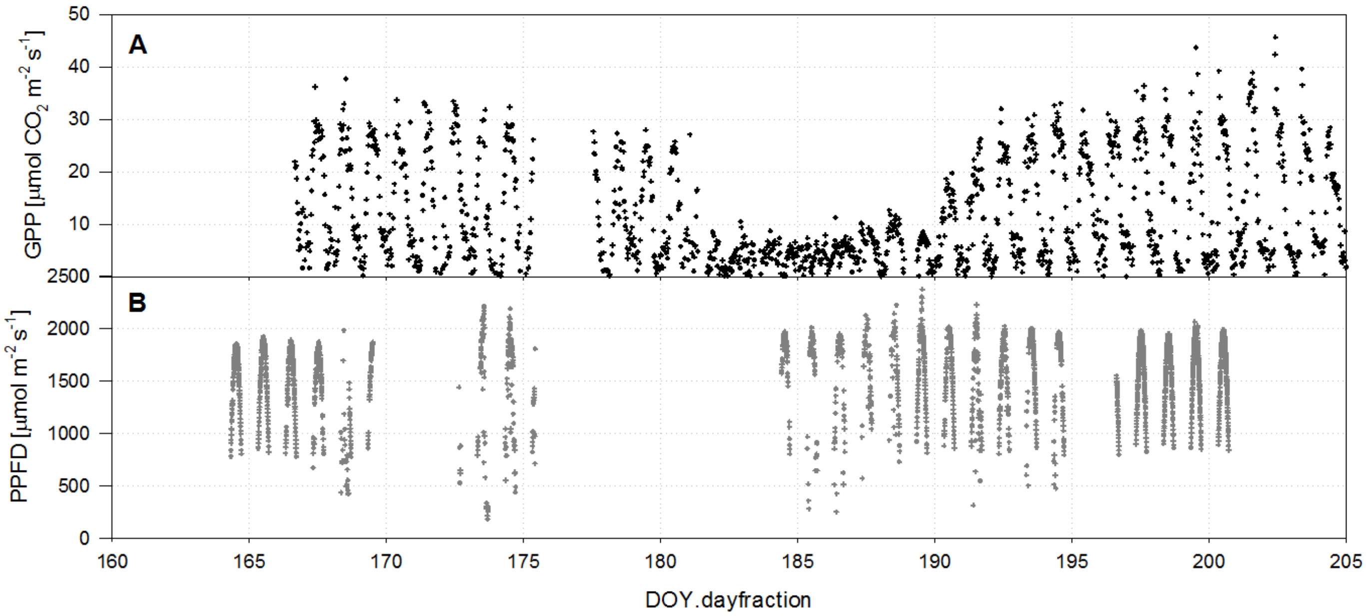

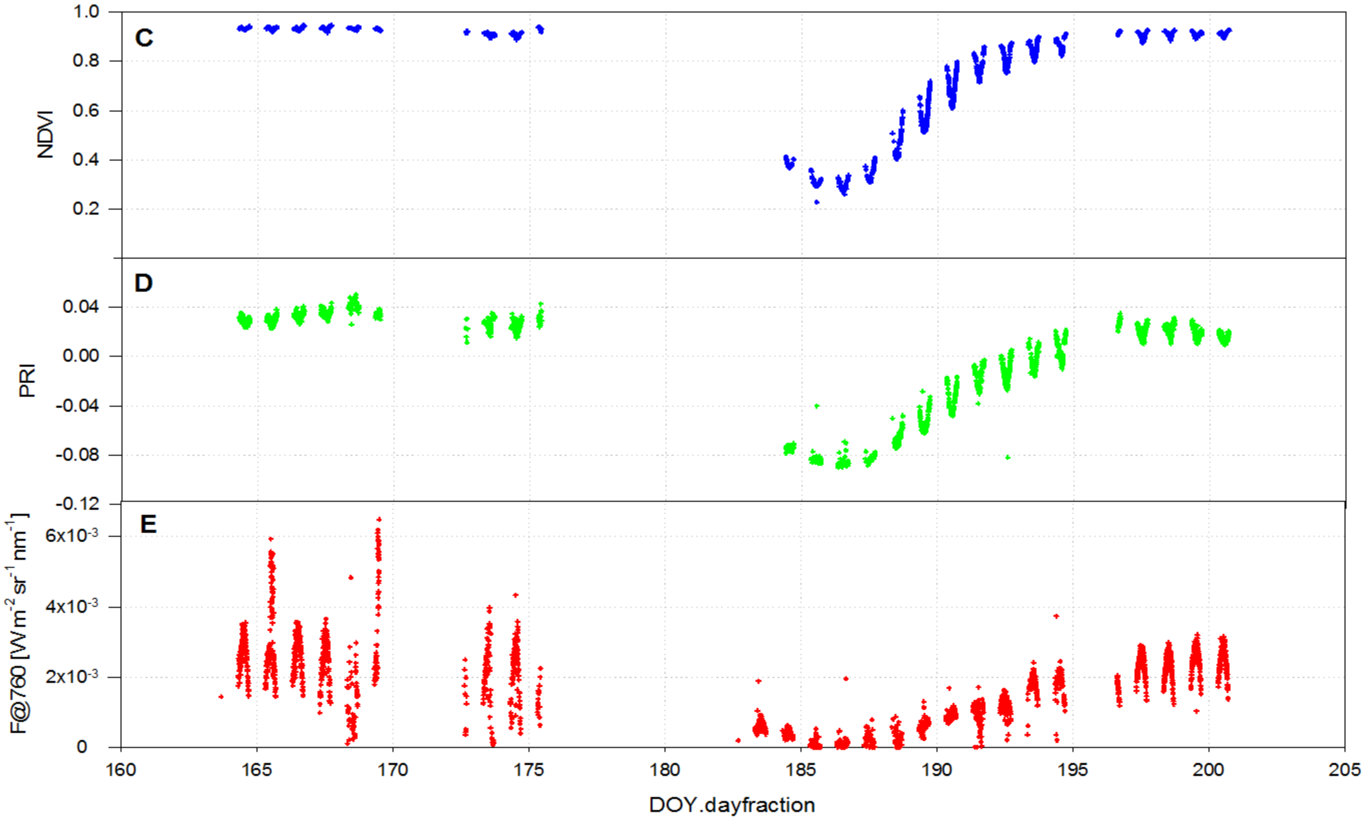
C
D
E
NDVI
PRI
F@760 [W m-2 sr-1 nm-1]
1.0
0.8
0.6
0.4
0.2
0.04
0.00
-0.04
-0.08
-0.12
6x10-3
4x10-3
2x10-3
0
160
165
170
175
180
185
190
195
200
205
DOY.dayfraction

# Bibliography

Aubinet, M. et al., 2000. Estimates of the annual net carbon and water exchange of forests: The EUROFLUX methodology, Advances in Ecological Research, Vol 30. Advances in Ecological Research, pp. 113-175.

Baldocchi, D., 2008. Breathing of the terrestrial biosphere: lessons learned from a global network of carbon dioxide flux measurement systems. Australian Journal of Botany, 56(1): 1-26.

Baldocchi, D., Valentini, R., Running, S., Oechel, W. and Dahlman, R., 1996. Strategies for measuring and modelling carbon dioxide and water vapour fluxes over terrestrial ecosystems. Global Change Biology, 2(3): 159-168.

Baldocchi, D.D., 2003. Assessing the eddy covariance technique for evaluating carbon dioxide exchange rates of ecosystems: past, present and future. Global Change Biology, 9(4): 479-492.

Foken, T. and Wichura, B., 1996. Tools for quality assessment of surface-based flux measurements. Agricultural and Forest Meteorology, 78(1-2): 83-105.

Gamon, J.A., Penuelas, J. and Field, C.B., 1992. A Narrow-Waveband Spectral Index That Tracks Diurnal Changes in Photosynthetic Efficiency. Remote Sensing of Environment, 41(1): 35-44.

Gamon, J.A., Rahman, A.F., Dungan, J.L., Schildhauer, M. and Huemmrich, K.F., 2006. Spectral Network (SpecNet) - What is it and why do we need it? Remote Sensing of Environment, 103(3): 227-235.

Goulden, M.L., Munger, J.W., Fan, S.M., Daube, B.C. and Wofsy, S.C., 1996. Measurements of carbon sequestration by long-term eddy covariance: Methods and a critical evaluation of accuracy. Global Change Biology, 2(3): 169-182.

Heimann, M. and Reichstein, M., 2008. Terrestrial ecosystem carbon dynamics and climate feedbacks. Nature, 451(7176): 289-292.

Law, B.E. et al., 2002. Environmental controls over carbon dioxide and water vapor exchange of terrestrial vegetation. Agricultural and Forest Meteorology, 113(1-4): 97-120.

Meroni, M. and Colombo, R., 2006. Leaf level detection of solar induced chlorophyll fluorescence by means of a subnanometer resolution spectroradiometer. Remote Sensing of Environment, 103(4): 438-448.

Meroni, M. et al., 2008a. Leaf level early assessment of ozone injuries by passive fluorescence and photochemical reflectance index. International Journal of Remote Sensing, 29(17-18): 5409-5422.

Meroni, M. et al., 2008b. Assessing steady-state fluorescence and PRI from hyperspectral proximal sensing as early indicators of plant stress: The case of ozone exposure. Sensors, 8(3): 1740-1754.

Moffat, A.M. et al., 2007. Comprehensive comparison of gap-filling techniques for eddy covariance net carbon fluxes. Agricultural and Forest Meteorology, 147(3-4): 209-232.

Moya, I. et al., 2004. A new instrument for passive remote sensing 1. Measurements of sunlight-induced chlorophyll fluorescence. Remote Sensing of Environment, 91(2): 186-197.

Papale, D. et al., 2006. Towards a standardized processing of Net Ecosystem Exchange measured with eddy covariance technique: algorithms and uncertainty estimation. Biogeosciences, 3(4): 571-583.

Reichstein, M. et al., 2005a. On the separation of net ecosystem exchange into assimilation and ecosystem respiration: review and improved algorithm. Global Change Biology, 11(9): 1424-1439.

Reichstein, M., Subke, J.A., Angeli, A.C. and Tenhunen, J.D., 2005b. Does the temperature sensitivity of decomposition of soil organic matter depend upon water content, soil horizon, or incubation time? Global Change Biology, 11(10): 1754-1767.

Rossini, M. et al., 2010. High resolution field spectroscopy measurements for estimating gross ecosystem production in a rice field. Agricultural and Forest Meteorology, 150(9): 1283-1296.

Rouse, J.W., Haas, R.H., Schell, J.A., Deering, D.W. and Harlan, J.C., 1974. Monitoring the Vernal Advancements and Retro Gradation of Natural Vegetation, Greenbelt, MD, USA.

Schaepman-Strub, G., Schaepman, M.E., Painter, T.H., Dangel, S. and Martonchik, J.V., 2006. Reflectance quantities in optical remote sensing-definitions and case studies. Remote Sensing of Environment, 103(1): 27-42.

Soussana, J.F. et al., 2004. (Carbon cycling and sequestration opportunities in temperate grasslands. Soil Use and Management, 20: 219-230.

Webb, E.K., Pearman, G.I. and Leuning, R., 1980. CORRECTION OF FLUX MEASUREMENTS FOR DENSITY EFFECTS DUE TO HEAT AND WATER-VAPOR TRANSFER. Quarterly Journal of the Royal Meteorological Society, 106(447): 85-100.

Wohlfahrt, G. et al., 2003. Canopy structure versus physiology effects on net photosynthesis of mountain grasslands differing in land use. Ecological Modelling, 170(2-3): 407-426.

## Chapter 6

# Using the Spectral Data in LUE Based Models

Tower-based *Eddy Covariance* (EC) measurements are essential for the comprehension of the main processes governing the carbon cycle in terrestrial ecosystems and represent an important data source for the development of both data-oriented and process-based models to simulate carbon fluxes at different time scales. Fundamental differences existing between EC and Satellite Remote Sensing observations, however, make upscaling of spatially discrete findings to landscape and global levels challenging. The development of automatic spectrometric systems: *HyperSpectral Irradiometer* (section 3.1) and *Multiplexer Radiometer Irradiometer* (section 3.2), can help to provide a link between the physiological status of vegetation measurable from $CO_2$ exchange and the associated changes in spectral properties (reflectance and fluorescence) of the plant canopy.

As a demonstration of the potential of such instruments for productivity estimate, last chapter of this dissertation concerns the application of the spectral indices described in the previous chapters (VIs, PRI and F) in *Light-Use Efficiency* (LUE, Monteith, 1972; 1977). Such models states that carbon fixation is a function of the incident *Photosynthetically Active Radiation Absorbed* by vegetation (APAR), determined as the product of the *Fraction Of Photosynthetically Active Radiation Absorbed* by vegetation (ƒAPAR) and the Incident *Photosynthetically Active Radiation* (PAR), and *Light-Use Efficiency* (ε) which represents the conversion efficiency of absorbed energy to fixed carbon.

From a RS perspective, LUE models are attractive because their entire set of input parameters can in principle be derived from RS measurements (for a review see Hilker et al., 2008b). The determination of *f*APAR from RS data has matured over a number of years supported by the close relationship between absorbed solar energy and spectral vegetation indices exploiting the visible and near-infrared regions - such as the well-known *Normalized Difference Vegetation Index* (NDVI) (Rouse et al., 1974).

In current RS-based LUE models, ε is generally implemented as a constant (sometimes assigned according to plant functional type) or as a potential maximum ε adjusted for unfavorable environmental conditions (e.g., limitations of temperature, humidity, soil moisture, etc.) (Heinsch et al., 2006; Nouvellon et al., 2000; Veroustraete et al., 2002) and other environmental factors affecting ε such as the composition of solar radiation (i.e., the ratio of direct to diffuse radiation; (i.e., the ratio of direct to diffuse radiation Cook et al., 2008). Other approaches propose to directly infer ε from RS exploit variations in vegetation spectral properties resulting from two processes closely linked to photosynthesis: photoprotection and Chl fluorescence.

Determining ε using photoprotection is based on the narrow-band detection of xanthophyll de-epoxidation, a photoprotective mechanism involved in the heat dissipation of excess energy used by plants to prevent oxidative damage to the photosynthetic apparatus in leaves (Demmig-Adams and Adams, 2000). The interconversion of the xanthophyll cycle pigments in intact leaves can be tracked by the Photochemical Reflectance Index (PRI, Gamon et al., 1992) using two wavelengths: 531 nm, which is affected by the xanthophyll de-epoxidation state, and 570 nm which is used as a reference to normalize other confounding effects (e.g., leaf structure). Several studies have shown a good relationship between PRI and photosynthetic rates and ε when measuring at leaf (Gamon et al., 1997; Meroni et al., 2008a) and canopy scale (Garbulsky et al., 2008; Meroni et al., 2008b; Nakaji et al., 2008; Nichol et al., 2000; Nichol et al., 2002; Nichol et al., 2006). However, (Rascher and Pieruschka, 2008) have shown that PRI may fail to detect changes in ε in crops because of the strong effect of canopy structure on the relationship between ε and PRI (Barton and North, 2001; Hilker et al., 2008a; Suarez et al., 2008).

An alternative way of inferring ε remotely is to exploit the relationship between carbon fixation (GPP or photosynthesis) and Chl fluorescence. Some studies have recently shown that F can be used to estimate ε at leaf (Meroni et al., 2008a) and canopy level (Damm et al., 2010; Meroni et al., 2008b). For a given canopy, the intensity of F is driven by the amount of the incident photosynthetic active radiation. Therefore, F has been normalized with PAR to get an apparent fluorescence yield, $Fy^*$ (Amoros-Lopez et al., 2008; Meroni and Colombo, 2006; Meroni et al., 2008a; Meroni et al., 2008b; Rascher and Pieruschka, 2008), to estimate ε. Changes in $Fy^*$ have been attributed to changes in the status and vitality of photosystems, and thus related to $CO_2$ assimilation. However, the translation of F data to photosynthesis is not trivial and still requires more theoretical and experimental research. In fact, the competition between F and photosynthesis for the use of absorbed light (which would result in a negative correlation between the two variables) is observed only under low light unstressed conditions (no non-photochemical protection mechanisms activated). On the contrary, most studies have observed a positive correlation between F and photochemistry in presence of plant stress and high light conditions. F declines with photosynthesis as a result of protective mechanisms (e.g., deactivation of the antenna, activation of the xanthophyll cycle and non-photochemical protection) that take place in the leaf to prevent damage from overexcitation under stressful conditions (van der Tol et al., 2009). In this chapter, several versions of LUE models were tested to understand the most effective formulation for estimating EC-derived GPP.

# 6.1 Data used

Data series of $CO_2$ gas-exchange and spectral data collected by HSI and MRI during the field tests reported in chapter 5 are used in LUE model to test the capabilities to estimate GPP (derived by EC data) using spectral indexes. In particular are utilized the database collected in both the field survey carried out in summer 2009: *PhenoAlp* and *Sentinel-3 Experiment*. Spectral indexes and $CO_2$ gas-exchange EC data acquired between 11.00 a.m. and 1.00 p.m. are used in this study to test different versions of the LUE model. Spectral indexes computed from the canopy reflectance spectra acquired with the automatic systems developed during this research were averaged for each half-hourly period according the methodology reported in chapter 4.2, in order to obtain data comparable to those acquired at the EC tower. Spectral indexes investigated in this study are reported in Table 6.1.

*Table 6.1: Spectral vegetation indices investigated in this study. R is the reflectance at the specified wavelength (nm). Spectral indices are grouped in three classes according to their suitability in inferring fAPAR, APAR and ε (E indexes).*

| Index | Formulation | References |
|---|---|---|
| ***fAPAR*** | | |
| NDVI | $(R_{800}-R_{680})/(R_{800}+R_{680})$ | Rouse et al., 1974 |
| ***APAR*** | | |
| F@760 | | Meroni and Colombo, 2006 |
| ***ε (E indexes)*** | | |
| sPRI | $[(R_{531}-R_{570})/(R_{531}+R_{570}) + 1]/2$ | Gamon et al., 1992 |
| Fy@760 | F@760/PAR | Meroni and Colombo, 2006 |

Among various VIs proposed in the literature as a proxy of *f*APAR, we selected the well-known normalized difference vegetation index (NDVI, Rouse et al., 1974). The selection of the best index for *f*APAR estimation is beyond the aim of this thesis, but I am aware that other VIs can perform better (or worse).

To estimate ε by RS indices we compute a scaled value of PRI according to Rahman et al. (2004) and the apparent fluorescence yield at 760 nm ($Fy_{760}$), computed as the ratio between F@760 and PAR (chapter 2). F@760 was estimated by exploiting the spectral fitting method described in Meroni and Colombo (2006) and Meroni et al. (2010a), assuming a linear variation of reflectance and fluorescence in the $O_2$-A absorption band region (chapter 2). Since fluorescence is driven by the intensity of PAR and by the amount of canopy biomass and structure and considering that at 760 nm it is not influenced by reabsorption (Louis et al., 2005), F@760 is used in this study as a proxy of photosynthetic canopy APAR (Rossini et al., 2010).

## 6.2 Light-Use Efficiency Models

Several versions of the basic LUE model were test in order to select the most effective formulation for the description of GPP. Linearity is always assumed between the spectral index and its target variable. Models investigated rely on different assumptions concerning APAR estimation and ε, which can be considered constant or estimated from RS data. GPP estimation accuracy of different models, including sun-induced fluorescence was then compared. Different model formulations together with their underlying assumptions are reported in Table 6.2. The resulting model formulation is reported in the far right column of Table 6.2. Models are grouped into three major sets according to the assumptions employed. The coefficients to be empirically determined are in bold print.

*Table 6.2: Formulation of LUE models used for the estimation of GPP. The coefficients to be empirically determined are in bold print.*

| Model code | ε | APAR | Model formulation |
|---|---|---|---|
| **1** | Const. | *f*(NDVI, PAR) | GPP = ε ·($a_0$NDVI + $a_1$) · PAR = ($\mathbf{b_0}$NDVI + $\mathbf{b_1}$) · PAR |
| **2** | *f*(E) | *f*(NDVI, PAR) | GPP = ($a_0$E + $a_1$) · ($a_2$NDVI + $a_3$) · PAR = ($\mathbf{b_0}$E + $\mathbf{b_1}$NDVI + $\mathbf{b_2}$NDVI · E + $\mathbf{b_3}$) · PAR |
| **3** | *f*(E) | *f*(F@760) | GPP = ($a_0$E + $a_1$) · ($a_2$F@760 + $a_3$) = $\mathbf{b_0}$E + $\mathbf{b_1}$F@760 + $\mathbf{b_2}$F@760 · E + $\mathbf{b_3}$ |

The first model holds ε constant and estimates total APAR as the product of fAPAR and PAR with *f*APAR assumed to be linearly related to NDVI. PAR is an ancillary input to be provided to the model. In this study it is derived from measurements at the EC tower.

These models assume a constant ε, therefore they are sensitive to the amount of light absorbed, but not to the efficiency with which vegetation uses this to fix carbon. They can only detect variations in ε caused by prolonged stress, which causes a degradation of photosynthetic pigment but not short-term (hours or days) stresses, which do not immediately degrade the pigment pool but reduce photosynthesis through a variety of physiological mechanisms.

To overcome the limitation of constant ε, a second set of models evaluates the possibility of directly determining both APAR (or fAPAR) and ε from RS data. ε is expressed in terms of physiologically-based remote indices sPRI and Fy*760 using a linear relationship. Linear relationships with ε have been reported for both PRI (Nakaji et al., 2008; Nichol et al., 2000; Nichol et al., 2002) and $Fy^*_{760}$ (Damm et al., 2010; Meroni et al., 2008a). Model 2 uses the same formulations of previous model as concerns APAR and incorporates the estimation of ε based on linear functions of sPRI and $Fy^*_{760}$. Finally model 3 uses the same formulations of previous model as concerns ε and estimates APAR as a function of F@760. This latter model is attractive from a RS point of view because it is based only on the knowledge of the remotely sensed F@760 without requiring ancillary measurements of the PAR like the other model formulations.

Model coefficients and their relative standard errors were estimated using the Gauss-Newton nonlinear least square optimization method (Bates and Watts, 1988), implemented in the R standard package (R, version 2.6.2). The main fitting statistics such as the determination coefficient ($r^2$), the root mean square error (RMSE) and the relative RMSE (rRMSE) between observed and modeled GPP were computed to evaluate the overall accuracy of fitted models. The cross-validated statistics ($r^2_{cv}$, $RMSE_{cv}$ and $rRMSE_{cv}$) obtained with the leave-one-out cross-validation procedure were computed to compare performances of different models in predicting GPP. The various model formulations show different number of parameters, p. With the intent of penalizing the more complex formulations, we computed the information criterion (AIC) developed by Akaike (1973).

$$AIC = 2(p+1) + n\left[ln\left(\frac{RSS_{cv}}{n}\right)\right] \qquad \textit{Equation 6.1}$$

where p is the number of parameters, n is the number of observations and $RSS_{cv}$ is the residual sum of squares generated by the cross validation procedure. The AIC allows estimation of the best model formulation considering the trade-off between model complexity and maximum likelihood (here calculated as $RSS_{cv}$). The lower the AIC the better the model considered. Since n is fixed for any given data set, AIC essentially balances better model explanatory power against increasing complexity.

# 6.3 Results

The summary statistics in fitting and cross-validation of different models tested in this study are reported in Table 6.3. Model 1 showed a $RMSE_{cv}$ in GPP estimation of 4.85 and 2.75 µmol $CO_2$ $m^{-2}$ $s^{-1}$, for the alfalfa field and the pasture, respectively, corresponding to a rRMSE of about 23% for both sites. To overcome the assumption of constant ε, model 2 in which ε is estimated with physiologically based vegetation indices was considered. The use of sPRI and/or $Fy_{760}$ to describe ε slightly increased the accuracy of GPP estimation; this is probably due to the redundancy of part of the information associated with ε-related indices and NDVI. Models using sPRI to estimate ε had generally an average RMSEcv lower than the corresponding models based on Fy*760. Model 3 estimating APARPV as a function of F@760 and ε as a function of either sPRI or Fy*760 showed the best performances, demonstrating that besides sPRI also Fy760 is a promising candidate powerful RS parameter that can be used to directly quantify light use efficiency. In particular, the model with F@760 and sPRI showed an RMSEcv of 2.87 and 2.01 µmol $CO_2$ m-2 s-1, for the alfalfa field and the pasture, respectively, corresponding to a rRMSEcv from about 13.5% to 17%. Model 3 is based entirely on RS variables and does not require any ground-based meteorological inputs. This model had also the lowest AIC, thus the increase of model complexity with respect to model 2 is fully compensated by its better performances.

Results of Table 6.3 were graphically summarized in Figure 6.1. GPP values estimated from EC measurements (EC-GPP) of each half-hourly period considered in the analysis were compared with those modeled with the best-performing RS model (RS-GPP) for each of the three model sets: model 1 in which fAPAR is estimated as a function of NDVI (Figure 6.1, a, b); model 2 in which fAPAR is estimated as a function of NDVI and ε as a function of sPRI (Figure 6.1 c, d); and model 3 where APAR is estimated as a function of F@760 and ε as a function of sPRI (Figure 6.1 e, f).

*Table 6.3: Summary of statistics in fitting ($r^2$, RMSE and rRMSE) and cross-validation ($r^2_{cv}$, $RMSE_{cv}$, $rRMSE_{cv}$ and AIC) of different models tested in this study. The best-performing model for each dataset is in bold print.*

| Model code | RS data | | $r^2$ | $r^2_{cv}$ | RMSE | $RMSE_{cv}$ | AIC | rRMSE | $rRMSE_{cv}$ |
|---|---|---|---|---|---|---|---|---|---|
| | ***f*APAR** | **ε** | | | (µmol $CO_2$ $m^{-2}$ $s^{-1}$) | | | (%) | |
| ***Alfalfa field*** | | | | | | | | | |
| Model 1 | NDVI | | 0.77 | 0.76 | 4.79 | 4.85 | 214.5 | 22.68 | 22.98 |
| Model 2 | NDVI | $Fy^{*}_{760}$ | 0.80 | 0.77 | 4.44 | 4.76 | 216.0 | 21.05 | 22.55 |
| | NDVI | sPRI | 0.80 | 0.78 | 4.42 | 4.67 | 212.2 | 20.94 | 22.14 |
| Model 3 | F@760 | $Fy^{*}_{760}$ | 0.80 | 0.76 | 4.48 | 4.94 | 220.8 | 21.21 | 23.39 |
| | **F@760** | **sPRI** | **0.93** | **0.92** | **2.69** | **2.87** | **149.0** | **12.75** | **13.58** |
| ***Pasture 2009*** | | | | | | | | | |
| Model 1 | NDVI | | 0.52 | 0.51 | 2.71 | 2.75 | 220.5 | 22.61 | 22.93 |
| Model 2 | NDVI | $Fy^{*}_{760}$ | 0.53 | 0.50 | 2.69 | 2.78 | 226.8 | 22.46 | 23.17 |
| | NDVI | sPRI | 0.68 | 0.64 | 2.23 | 2.35 | 189.8 | 18.62 | 19.61 |
| Model 3 | F@760 | $Fy^{*}_{760}$ | 0.48 | 0.44 | 2.84 | 2.93 | 237.6 | 23.65 | 24.39 |
| | **F@760** | **sPRI** | **076** | **0.74** | **1.92** | **2.01** | **157.9** | **16.04** | **16.75** |

A significant linear relationship was found for all models. As expected, model 3 shows the higher coefficient of determination ($r^2 = 0.93$ and $r^2 = 0.76$, $p < 0.0001$, for MRI and HSI, respectively) and a slope equal or very close to 1.0. Model 1, describing the GPP as a function of the total absorption capacity only, appears to be inadequate to explain the variance of measured GPP, in particular for HSI, with an underestimation at low GPP values where saturation occurs. In addition, the lower amount of EC-GPP variance explained by this model ($r^2 = 0.79$ and $r^2 = 0.54$, for MRI and HSI, respectively) with respect to the others suggests a failure to the description of the seasonal pattern of EC-GPP. Model 1 and 2 perform better in the alfalfa crop field compared to the pasture, because the vegetation cycle of alfalfa was characterized by a strong dynamic of biomass growth, thus of NDVI, so that $\varepsilon$ plays a minor role in controlling GPP.

In conclusion, results show that the use of the apparent fluorescence yield and the Photochemical Reflectance Index to model $\varepsilon$ instead of holding $\varepsilon$ constant slightly improves the estimation of GPP. The major improvement in midday GPP estimation occurs when F@760 is used to model the photosynthetically active radiation absorbed by the photosynthetic components of vegetation. This latter model is very attractive because it is entirely based on remotely sensed quantities without requiring any ancillary measurement, like other LUE model formulations which require ancillary measurements of the incident PAR to estimate APAR, and it is very interesting in the perspective of a spatial estimation of GPP.

In conclusion, results show that the use of the apparent fluorescence yield and the Photochemical Reflectance Index to model $\varepsilon$ instead of holding $\varepsilon$ constant slightly improves the estimation of GPP. The major improvement in midday GPP estimation occurs when F@760 is used to model the photosynthetically active radiation absorbed by the photosynthetic components of vegetation. This latter model is very attractive because it is entirely based on remotely sensed quantities without requiring any ancillary measurement, like other LUE model formulations which require ancillary measurements of the incident PAR to estimate APAR, and it is very interesting in the perspective of a spatial estimation of GPP.

*Figure 6.1: Relationship between GPP values of each half-hourly period considered in the analysis (solar noon ± 1 hour) estimated from EC measurements (EC-GPP) and modeled (RS-GPP) with model 1 (fAPAR = f(NDVI)) (a, MRI and b, HSI), the best-performing model 2 (fAPAR = f(NDVI) and ε = f(sPRI)) (c, MRI and d, HSI) and the best-performing model 3 (APAR = f(F@760) and ε = f(sPRI)) (e, MRI and f, HSI) (c). Linear regression equations, determination coefficients and p values are reported.*

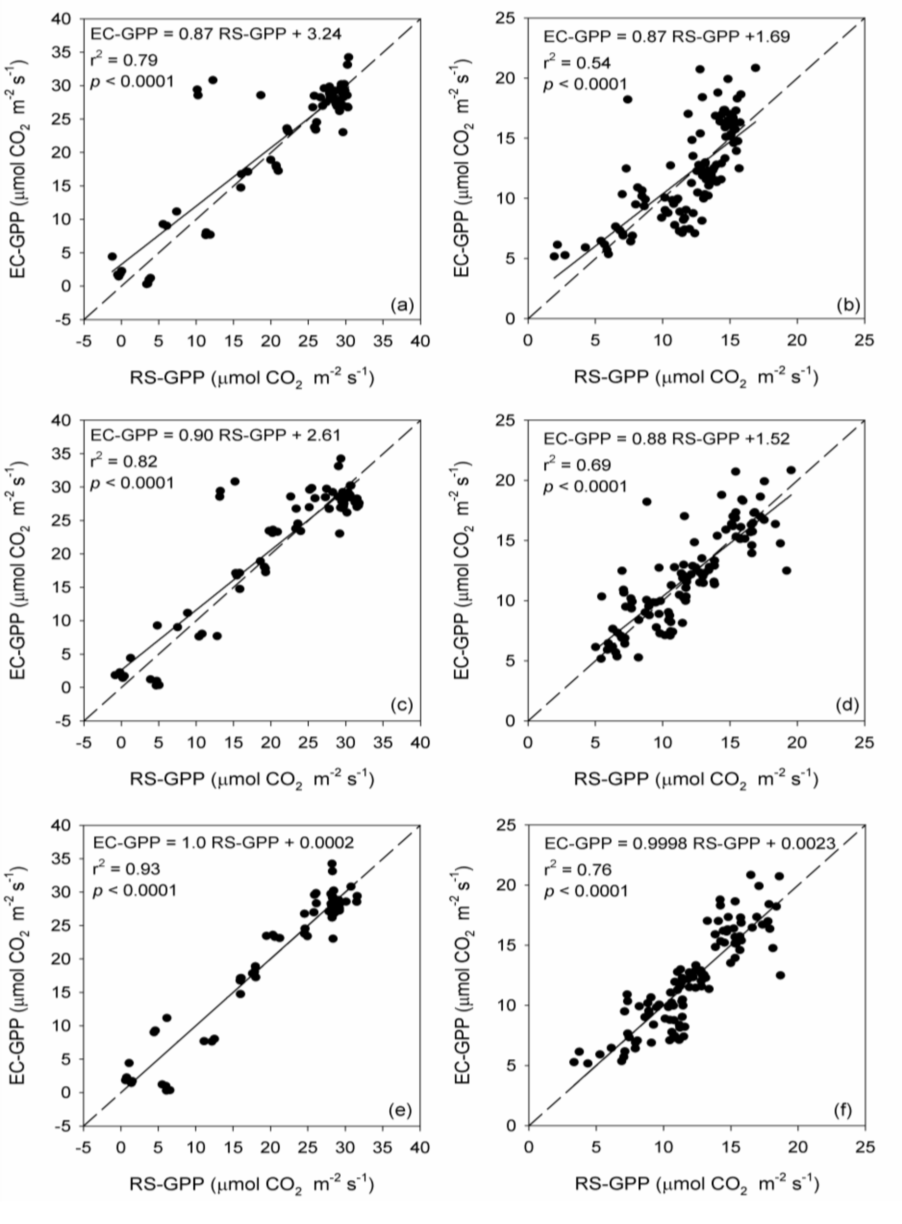

# Bibliography

Amoros-Lopez, J. et al., 2008. Evaluation of remote sensing of vegetation fluorescence by the analysis of diurnal cycles. International Journal of Remote Sensing, 29(17-18): 5423-5436.

Barton, C.V.M. and North, P.R.J., 2001. Remote sensing of canopy light use efficiency using the photochemical reflectance index - Model and sensitivity analysis. Remote Sensing of Environment, 78(3): 264-273.

Cook, B.D. et al., 2008. Using light-use and production efficiency models to predict photosynthesis and net carbon exchange during forest canopy disturbance. Ecosystems, 11(1): 26-44.

Damm, A. et al., 2010. Remote sensing of sun induced fluorescence to improve modelling of diurnal courses of Gross Primary Production (GPP). Global Change Biology, 16(1): 171-186.

Demmig-Adams, B. and Adams, W.W., 2000. Photosynthesis - Harvesting sunlight safely. Nature, 403: 371-374.

Gamon, J.A., Penuelas, J. and Field, C.B., 1992. A Narrow-Waveband Spectral Index That Tracks Diurnal Changes in Photosynthetic Efficiency. Remote Sensing of Environment, 41(1): 35-44.

Gamon, J.A., Serrano, L. and Surfus, J.S., 1997. The photochemical reflectance index: an optical indicator of photosynthetic radiation use efficiency across species, functional types, and nutrient levels. Oecologia, 112(4): 492-501.

Garbulsky, M.F., Penuelas, J., Papale, D. and Filella, I., 2008. Remote estimation of carbon dioxide uptake by a Mediterranean forest. Global Change Biology, 14(12): 2860-2867.

Heinsch, F.A. et al., 2006. Evaluation of remote sensing based terrestrial productivity from MODIS using regional tower eddy flux network observations. Ieee Transactions on Geoscience and Remote Sensing, 44(7): 1908-1925.

Hilker, T. et al., 2008a. Separating physiologically and directionally induced changes in PRI using BRDF models. Remote Sensing of Environment, 112(6): 2777-2788.

Hilker, T., Coops, N.C., Wulder, M.A., Black, T.A. and Guy, R.D., 2008b. The use of remote sensing in light use efficiency based models of gross primary production: A review of current status and future requirements. Science of the Total Environment, 404(2-3): 411-423.

Louis, J. et al., 2005. Remote sensing of sunlight-induced chlorophyll fluorescence and reflectance of Scots pine in the boreal forest during spring recovery. Remote Sensing of Environment, 96(1): 37-48.

Meroni, M. and Colombo, R., 2006. Leaf level detection of solar induced chlorophyll fluorescence by means of a subnanometer resolution spectroradiometer. Remote Sensing of Environment, 103(4): 438-448.

Meroni, M. et al., 2008a. Leaf level early assessment of ozone injuries by passive fluorescence and photochemical reflectance index. International Journal of Remote Sensing, 29(17-18): 5409-5422.

Meroni, M. et al., 2008b. Assessing steady-state fluorescence and PRI from hyperspectral proximal sensing as early indicators of plant stress: The case of ozone exposure. Sensors, 8(3): 1740-1754.

Monteith, J.L., 1972. Solar radiation and productivity in tropical ecosystems. Journal of Applied Ecology, 9: 747-766.

Monteith, J.L., 1977. Climate and efficiency of crop production in Britain. Philosophical Transactions of the Royal Society of London Series B-Biological Sciences, 281: 271-294.

Nakaji, T. et al., 2008. Utility of spectral vegetation indices for estimation of light conversion efficiency in coniferous forests in Japan. Agricultural and Forest Meteorology, 148(5): 776-787.

Nichol, C.J. et al., 2000. Remote sensing of photosynthetic-light-use efficiency of boreal forest. Agricultural and Forest Meteorology, 101(2-3): 131-142.

Nichol, C.J. et al., 2002. Remote sensing of photosynthetic-light-use efficiency of a Siberian boreal forest. Tellus Series B-Chemical and Physical Meteorology, 54(5): 677-687.

Nichol, C.J., Rascher, U., Matsubara, S. and Osmond, B., 2006. Assessing photosynthetic efficiency in an experimental mangrove canopy using remote sensing and chlorophyll fluorescence. Trees-Structure and Function, 20(1): 9-15.

Nouvellon, Y. et al., 2000. Time course of radiation use efficiency in a shortgrass ecosystem: Consequences for remotely sensed estimation of primary production. Remote Sensing of Environment, 71(1): 43-55.

Rascher, U. and Pieruschka, R., 2008. Spatio-temporal variations of photosynthesis: the potential of optical remote sensing to better understand and scale light use efficiency and stresses of plant ecosystems. Precision Agriculture, 9(6): 355-366.

Rossini, M. et al., 2010. High resolution field spectroscopy measurements for estimating gross ecosystem production in a rice field. Agricultural and Forest Meteorology, 150(9): 1283-1296.

Rouse, J.W., Haas, R.H., Schell, J.A., Deering, D.W. and Harlan, J.C., 1974. Monitoring the Vernal Advancements and Retro Gradation of Natural Vegetation, Greenbelt, MD, USA.

Suarez, L. et al., 2008. Assessing canopy PRI for water stress detection with diurnal airborne imagery. Remote Sensing of Environment, 112(2): 560-575.

van der Tol, C., Verhoef, W. and Rosema, A., 2009. A model for chlorophyll fluorescence and photosynthesis at leaf scale. Agricultural and Forest Meteorology, 149(1): 96-105.

Veroustraete, F., Sabbe, H. and Eerens, H., 2002. Estimation of carbon mass fluxes over Europe using the C-Fix model and Euroflux data. Remote Sensing of Environment, 83(3): 376-399.

# Chapter 7

# Conclusions

The aim of the present research was the development of automatic spectrometric systems capable of collecting unattended, continuous, long-term spectral measurements. The developed systems are intended to be operated in experimental sites equipped with *Eddy Covariance* flux towers to increase our understanding of the link between optical signals and *Gross Primary Productivity (GPP)*, because *Remote Sensing* observations can provide spatial (e.g. regional and global) and temporal variability of ecosystem parameters driving carbon fluxes, which can be integrated with local scale *Eddy Covariance* measurements to scale up carbon assessment.

In this research activity two different automatic spectrometric systems were developed: the *HyperSpectral Irradiometer* (HSI) and the *Multiplexer Radiometer Irradiometer* (MRI). Both instruments are able to routinely and autonomously measure: sun incoming irradiance (downwelling Irradiance, $E^{TOT}$) and the irradiance/radiance upwelling from the investigated Earth surface (HSI measures $E^S$, MRI measures $L^S$). The HSI is an entirely custom designed instrument developed in collaboration with the Italian National Research Council (IFAC-CNR, Florence, Italy). The instrument employs a rotating arm to observe alternately the sky and the target surface with the same cosine-response foreoptic allowing the computation of the BHR (*Bi-Hemispherical Reflectance factor*). The MRI, instead, is obtained assembling commercial opto-electronic components: the core of the instrument is a commercial *optical multiplexer* (MPM-2000, Ocean Optics, USA) that switches the input of the spectrometers between different optical channels (optical fibers) allowing to alternatively measure sun irradiance (downwelling) and radiance coming from the Earth surface (upwelling).

Using the optical layout described, MRI allows the measurement of the HCRF (*Hemispherical-Conical Reflectance Factor*).

These instruments are able to simultaneously collect “*fine*” and “*ultra-fine*” spectrums in the optical domain. The collected spectral data allow to estimate: i) vegetation biochemical and structural parameters using optical *Vegetation Indices* (e.g. NDVI)*; ii)* the *energy dissipation pathways* exploiting the *Photochemical Reflectance Index* (PRI) and the *sun-induced chlorophyll Fluorescence* at $O_2$-A band (F@760). Even if recent studies have shown some potential of PRI and F@760 for GPP estimation of, the relationship between optical signals and photosynthesis is not yet fully understood, in particular at canopy level, where radiometric signals are strongly affected by viewing and illumination angles, canopy architecture (e.g. leaf orientation and leaf area) and soil background.

The development of such systems involved the opto-mechanical design (*hardware*), and the definition of the spectral and radiometric calibration procedures. The opto-mechanical design consisted in the selection and assembly of different components employed in the instruments, in terms of spectrometers, foreoptics, mirrors, etc. Different procedures have been defined for spectral and radiometric calibration of these systems. Spectral calibration entailed two phases: a “*laboratory calibration*” carried out yearly before installing the instrument in the field and an “*in-situ calibration*” performed regularly during instrument field operations to check and keep upgraded the instrument calibration coefficients. Laboratory calibration was realized applying improved version of the standard methodology provided by spectrometer manufacture (Ocean Optics, US), while *in-situ* calibration was performed by means of the SpecCal algorithm. Radiometric calibration, instead, has not been realized in laboratory because it requires the use of special equipment (e.g. large Integrating Sphere traceable to International Standard) expensive and available only at a research centres of international importance. In this research, radiometric calibration was inferred by cross-calibration with a manually operated reference system calibrated in laboratory.

During the research activity, a specific acquisition software (*Auto3S*) was developed to manage the fully automatic collection of unattended, continuous and long-term spectral measurements with both instruments.

The processing of the large amount of spectral data collected was achieved using the specifically developed OO_IDL computer code that systematically provides: data calibration (spectral/radiometric), computation of radiometric indexes and data quality control and filtering.

The automatic spectrometric systems developed in the first part of the research were then tested in field campaigns supported by two international research projects. Both projects dealt with the simultaneous measurement of spectral and $CO_2$ flux data to better understand the relationships between optical signals and photosynthesis. The HSI was installed and operated during two consecutive years in an abandoned pasture of the subalpine belt in the framework of the Interreg project PhenoAlp, while the MRI was employed in 2009 in the context of the Sen3Exp field survey promoted by the European Space Agency as consolidation study to the future mission Sentinel-3.

Results show that the proposed automatic spectrometric systems (HSI and MRI) succeeded in collecting unattended and long-term hyperspectral data. Reliable time series of optical properties (incident irradiance, radiance upwelling from the earth surface, resulting reflectance factors and vegetation indices) were obtained with both instruments, in different experimental conditions (i.e. extreme environmental conditions) and on different vegetated canopies. Furthermore, the high resolution of the spectrometers hosted by the developed systems allowed for the first time the acquisition of long-term time series of *sun-induced chlorophyll Fluorescence* at 760 nm.

Only few published studies concerned the simultaneous monitoring of eddy fluxes and high resolution spectral data. The seasonal trends obtained in this research are consistent to previous works. NDVI is strongly related to the canopy greenness and thus to its potential photosynthetic capacity. PRI and F@760 are instead related to excess energy dissipation pathways (heat and fluorescence) and thus to the canopy actual photosynthesis. The analysis of the diurnal patterns is more complex because they are affected by the reflectance bidirectional effects (BRDF) caused by variations in the sun-target-sensor geometry. While NDVI is not expected to change during a day and thus its diurnal pattern can be supposed to be entirely determined by BRDF effects, the observed PRI and F@760 nm diurnal patterns are an integrated function of both changes in geometrically induced illumination conditions and physiologically induced changes in vegetation spectral properties. The analysis of the BRDF effects is beyond the aim of this dissertation and will be addressed in future studies.

As a demonstration of the potential of these instruments to estimate the *Gross Primary Production* (GPP), optical vegetation indices and F@760 derived from HSI and MRI were used as inputs of LUE models in the last part of the research. Several versions of the basic LUE model were used in order to verify the most effective formulation for the description of GPP. Results show that the use of the *apparent fluorescence yield* and the PRI to model ε instead of holding ε constant improves the estimation of GPP. The major improvement in midday GPP estimation occurs when F@760 is used to model the photosynthetically active radiation absorbed by the photosynthetic components of vegetation, accordingly to a previous study on rice.

Although only the most common VIs were presented in this dissertation, future studies will address the investigation of a number of spectral indexes that can be derived from the hyperspectral data collected by HSI and MRI.

Concluding, the instruments developed in this research allowed to acquire a unique dataset of $CO_2$ flux data coupled with high resolution canopy spectra at high temporal frequency, including for the first time F@760. The effective integration of optical and flux data remains a difficult yet essential challenge, and the data collected during this activity provides a valuable foundation for improving the understanding of the link between $CO_2$ gas-flux and the optical signal.

The instruments proposed in this study finds application within the framework of the established *SpecNet* (Spectral Network) and recent activities related to the 'Spectral Sampling Tools for Vegetation Biophysical Parameters and Flux Measurements in Europe' COST action that are aimed to collect spectral data continuously, regularly and from a worldwide network in connection to the well-established network of flux tower (FLUXNET). However, these instruments can be also used to monitor other environmental compartments like atmosphere, ocean, ice etc. and routinely collect ground-truth observations that can be used to calibrate remote sensing images and to validate retrieved products.